

Master's thesis

Odin Celius
Magnus Leirvik Knoph

Plated aluminium structures exposed to extreme pressure loads

Master's thesis in Mechanical Engineering
Supervisor: Vegard Aune and Magnus Langseth
June 2020

NTNU
Norwegian University of Science and Technology
Faculty of Engineering
Department of Structural Engineering

Odin Celius
Magnus Leirvik Knoph

Plated aluminium structures exposed to extreme pressure loads

Master's thesis in Mechanical Engineering
Supervisor: Vegard Aune and Magnus Langseth
June 2020

Norwegian University of Science and Technology
Faculty of Engineering
Department of Structural Engineering



MASTER THESIS 2020

SUBJECT AREA: Computational Mechanics	DATE: June 30 th 2020	NO. OF PAGES: 14 + 74 + 24
--	-------------------------------------	-------------------------------

TITLE:

Plated aluminium structures exposed to extreme pressure loads

Platestrukturer av aluminium utsatt for ekstreme trykkbelastninger

BY:

Odin Celius

Magnus Leirvik Knoph



SUMMARY:

The term extreme pressure loads denote pressure loads with high magnitude, short duration and non-uniform spatial and temporal distribution. Extreme pressure loads are critical in the design of plated structures in many applications, but no accurate and convenient modelling approach for industrial application currently exist. To rectify this an uncoupled modelling approach was established. Loads were generated through Eulerian simulations in EUROPLEXUS and described to the pressure exposed surface of Lagrangian models in ABAQUS/Explicit. The novelty of the approach is the description of the load as a surface mesh. To investigate the responses of plated structures to extreme pressure loading - and validate the modelling approach - a new test rig for the SIMLab Shock Tube Facility was designed and a test matrix constructed. The flexible design successfully enabled the testing of various structures to extreme pressure loading of varying complexity, in a controlled laboratory environment.

In addition to testing deformable plated structures, tests were conducted on a rigid plate with piezoelectric sensors to validate the Eulerian simulations. Two deformable structures were tested, a simple plate and a panel with three stiffeners and a welded section, both made of the aluminium alloy AA6082-T6. In the deformable specimens subjected to extreme pressure loading large inelastic deformations, asymmetric responses and fractures were observed. The two structures responded differently to the loading conditions, but both responses were seen to vary with the load magnitude and complexity.

The Lagrangian simulations largely predicted the deformed shapes of the deformable test specimens. The asymmetric responses, strain localisation and fractures observed in the tests were all replicated, although the magnitude of the deflections were underestimated. The Lagrangian simulations of the panel tests conducted at the lowest firing pressure have good correspondence, indicating that the modelling approach successfully predicts structural responses to extreme pressure loads.

RESPONSIBLE TEACHER: Vegard Aune

SUPERVISOR(S): Vegard Aune and Magnus Langseth

CARRIED OUT AT: Department of Structural Engineering, NTNU



MASTEROPPGAVE 2020

FAGOMRÅDE: Beregningsmekanikk	DATO: 30. juni 2020	ANTALL SIDER: 14 + 74 + 24
----------------------------------	------------------------	-------------------------------

TITTEL:

Platestrukturer av aluminium utsatt for ekstreme trykkbelastninger

Plated aluminium structures exposed to extreme pressure loads

UTFØRT AV:

Odin Celius

Magnus Leirvik Knoph



SAMMENDRAG:

Begrepet ekstreme trykkbelastninger beskriver trykkklaster av høy størrelsesorden, kort varighet og ikke-lineær fordeling i tid og rom. Ekstreme trykkbelastninger er kritiske for designet av platestrukturer i en rekke av deres bruksområder, men per dags dato eksisterer ingen modelleringsmetode som er lettvinnt, nøyaktig og allmenn tilgjengelig for industrien. På grunn av dette ble en ukoblet modelleringsmetode etablert. Trykkklaster ble generert av Euler-modeller i EUROPLEXUS og brukt som lastbeskrivelse på den trykkutsatte overflaten til Lagrange-modeller i ABAQUS/Explicit. Det nye med metoden er at lasten blir beskrevet som et overflatenett. For å undersøke responsen til platestrukturer utsatt for ekstreme trykkbelastninger, og for å validere modelleringsmetoden, ble en ny testtrigg til SIMLab Shock Tube Facility utviklet og en testmatrise ble konstruert. Den modulære testtriggen gjorde det mulig å utsette forskjellige platestrukturer for ekstreme trykkbelastninger av varierende kompleksitet i kontrollerte omgivelser.

I tillegg til å teste deformerbare platestrukturer ble forsøk utført på en rigid plate med piezoelektriske sensorer for å validere Euler-modellene. To deformerbare platestrukturer ble testet, en enkel plate og et panel med tre avstivere og en langsgående sveis, begge laget av aluminiumslegeringen AA6082-T6. Store plastiske deformasjoner, asymmetriske responser og brudd ble observert i forsøkene på de deformerbare platestrukturene utsatt for ekstreme trykkbelastninger. De to platestrukturene hadde forskjellige responser til lastsituasjonene, men begge varierte med størrelsesordenen og kompleksiteten til lasten.

Lagrange-modellene klarte i stor grad å forutsi deformasjonsmodene til testeksemplarene. De asymmetriske responsene, tøyingslokaliseringene og bruddene ble alle gjengitt numerisk, men deformasjonenes størrelsesorden ble undervurdert. Lagrange-simuleringene av panelforsøkene med lavest trykk hadde god overenstemmelse med forsøkene, noe som indikerer at modelleringsmetoden er egnet til å forutsi strukturelle responser på ekstreme trykkbelastninger.

FAGLÆRER: Vegard Aune

VEILEDER(E): Vegard Aune og Magnus Langseth

UTFØRT VED: Institutt for konstruksjonsteknikk, NTNU

MASTER'S THESIS 2020

for

Odin Celius and Magnus Leirvik Knoph

Plated aluminium structures exposed to extreme pressure loads

1. INTRODUCTION

Extreme pressure loads may be critical in the design of several engineering structures (e.g. blast-resistant structures, offshore installations, ship structures or aircraft structures). These types of engineering designs often consist of plated structures with a non-uniform distribution of the pressure loading. Important characteristics of such structures are high strength-to-weight and stiffness-to-weight ratios. This may be achieved by using aluminium plates and stiffened panels. It is therefore of interest to investigate the dynamic response of plated aluminium structures exposed to non-uniform pressure loads of short durations. Computational methods are now available to predict both the loading and structural response in these extreme loading situations, and experimental validation of such methods is necessary in the development of safe and cost-effective engineering structures. This study will generate extreme loading conditions in controlled laboratory environments and use these tests as a basis for validation and verification of some frequently used computational methods involving extreme pressure loading.

2. OBJECTIVES

The main objective of the research project is to determine how plated aluminium structures behave under extreme non-uniform pressure loading, and to validate to which extent this can be predicted using traditional computational methods. Special focus is placed on accurate predictions of both the loading and the structural response. The extreme loading will be generated using the shock tube technique and compressed air.

3. A SHORT DESCRIPTION OF THE RESEARCH PROJECT

The main topics in the research project will be as follows;

1. A comprehensive literature review should be conducted to understand the extreme load phenomenon generated in a shock tube, large deformations of plated structures and explicit finite element (FE) methods.
2. A new experimental setup will be designed for the SIMLab Shock Tube Facility (SSTF). This setup should expose plated aluminium structures to non-uniform, extreme pressure loading, and will be used to investigate both the loading and the dynamic responses.
3. Material tests will be carried out to obtain the mechanical properties of the aluminium material and used to calibrate relevant constitutive relations.
4. Optical techniques will be used to visualize the load and the response during testing in the shock tube experiments. Examples of such techniques are high-speed cameras, digital image correlation and schlieren photography. It will also be used a massive plate equipped with pressure sensors to measure the load acting on a non-deformable plate in the new experimental setup for the SSTF.
5. The experimental data will be used to evaluate the performance of FE simulations in Abaqus/Explicit.

Supervisors: Vegard Aune (NTNU), Magnus Langseth (NTNU)

The thesis must be written according to current requirements and submitted to the Department of Structural Engineering, NTNU, no later than June 10th, 2020.

NTNU, January 15th, 2020



Vegard Aune
Associate Professor

Preface

The following work is a master's thesis in computational mechanics as a part of the MSc in Mechanical Engineering at the Norwegian University of Science and Technology (NTNU). The master's thesis was written for the Structural Impact Laboratory (SIMLab), a research group at the Department of Structural Engineering. The timespan of the master's thesis was set to 20 weeks, beginning in January 2020.

In the middle of March, the Coronavirus Disease (COVID-19) was declared a pandemic, causing shutdowns worldwide. Our campus at NTNU Gløshaugen was closed for both students and staff, abruptly stopping all laboratory work and forcing everyone to work from home. This isolation made the cooperation more difficult. Experimental tests for this work were scheduled for the end of March, but they were not completed until the middle of May, when vital functions reopened. Performing the experimental work was both relieving and interesting. The considerable delay forced us to apply for a 19 day extension, to enable us to process the experimental data. The thesis was completed on the 30th of June. The campus did not reopen for students during this period.

Although this thesis focuses on structural mechanics, fluid mechanics is also required to understand the structural response to extreme pressure loads. Combining both disciplines has been both challenging and intriguing.

Abstract

The term extreme pressure loads denotes pressure loads with a high magnitude, short duration and non-uniform spatial and temporal distributions. Extreme pressure loads are critical for the design of plated structures in many applications, but currently, no accurate and computationally efficient modelling approach for industrial applications exists. To this end, an uncoupled modelling approach was established. Loads were generated through Eulerian simulations in the finite element (FE) software EUROPLEXUS and prescribed to the pressure exposed surface of Lagrangian models in the FE software ABAQUS/Explicit. The novelty of the approach is the description of the load as a surface mesh. To investigate the response of plated structures to extreme pressure loading - and validate the modelling approach - a new test rig for the SIMLab Shock Tube Facility was designed and a test matrix was constructed. The flexible design successfully enabled the testing of various structures subjected to extreme pressure loading of varying complexity in a controlled laboratory environment.

In addition to testing deformable plated structures, tests were conducted on a rigid plate with piezoelectric sensors to validate the Eulerian simulations. Two deformable structures were tested - a simple plate and a panel with three stiffeners and a welded section - both made of the aluminium alloy AA6082-T6. For the deformable specimens subjected to extreme pressure loading, large inelastic deformations, asymmetric responses and fractures were observed. The two structures responded differently to the loading conditions, but both responses varied with load magnitude and complexity.

Numerical models describing the material behaviour of the deformable structures were established, consisting of constitutive models and failure criteria. The material parameters of the simple plate were identified through tensile testing and subsequent reverse engineering of a representative test in ABAQUS/Standard. The panel parameters already identified in [1] were used.

Due to a spurious drift in the measurements from the rigid plate tests, only the first 4 ms were credible. Therefore, only this domain of the Eulerian simulations was validated. The experimental peak reflected overpressures were 40 to 50% larger than in the CFD, and the rise times were about 90% shorter, likely due to the mesh of the fluid subdomain being too coarse. Due to time limitations refined mesh simulations were not performed. Although the discrepancies increased with load magnitude and complexity, the correspondence was close to 99% in 1.5-3 ms for most positions, indicating the validity of the Eulerian simulations in the said domain.

Overall, the Lagrangian simulations predicted the deformed shapes of the deformable test specimens well. The asymmetric response, strain localisation and fractures observed in the tests were all replicated, although the magnitudes of the deflections were underestimated. The new equilibrium positions in the simulations were 40 to 50% smaller for the plate and 12.5 to 33 % smaller for the panel, relative to the experimental values. While the test structures were modelled as accurate as possible, severe computational times lead to the exclusion of the rig frame from the models, hence simplifying the boundary conditions. While the plate was clamped to the rig frame the panel was simply supported, making the simplified boundary conditions a better approximation. The boundary conditions are likely the main reason for the poor performance of the plate. Finally, the Lagrangian simulations of the panel tests conducted with a nominal firing pressure of 20 bar corresponded well to the test results, indicating that the modelling approach with the novel description of the loads successfully predicts the structural response to the extreme pressure loads in this study.

Acknowledgements

We want to thank Assoc. Prof. Vegard Aune and Prof. Magnus Langseth for their contribution to this master thesis. Through their input and feedback, they have further increased our knowledge of and interest in the subject. They have both been essential to the master thesis development.

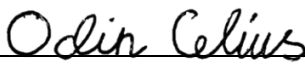
We would like to thank Senior Engineer Tore Andre Kristensen from SINTEF for helping us with the material tensile test.

Unfortunately, COVID-19 forced the closure of the university and its laboratories in March. This, of course, affected the experimental work as well as the thesis writing. In this period of home offices, Assoc. Prof. Vegard Aune was an invaluable support. He was quick to respond to our many doubts and questions through Microsoft Teams, he encouraged us to keep up the good work under the changed circumstances, and he truly took interest in the success of the said thesis. In the middle of May - weeks after the originally planned start date of the tests - we were allowed to commence the experimental work in the SIMLab Shock Tube Facility. We are forever grateful to Assoc. Prof. Vegard Aune and Senior Engineer Trond Auestad for enabling the execution of the tests. With their help, we achieved – at last – the experimental results that we feared COVID-19 would take away from us.


Additionally, we would like to thank our fellow master students, Anja Murud Gahre, Ragnhild Hembre Haug and Jon Hole-Drabløs, for great discussions and company during the semester.

And finally, we would like to thank all the special people in our lives for supporting and believing in us through this work.

Trondheim – June 30, 2020



Odin Celius



Magnus Leirvik Knoph

Contents

1	Introduction	1
1.1	Background and Motivation	1
1.2	Previous Work	1
1.3	Objectives	3
1.4	Scope	3
1.5	Thesis Outline	3
2	Preliminary Studies - Part I	4
2.1	Introduction	4
2.2	The SIMLab Shock Tube Facility	4
2.3	Test Structures	5
2.3.1	Plate	5
2.3.2	Stiffened Panel	5
2.4	Summary of Design History	6
2.4.1	Concept Analysis	6
2.4.2	Design Considerations	7
2.5	Summary of Final Setup	9
3	Material Modelling	10
3.1	Introduction	11
3.2	Uniaxial Tension Tests	11
3.2.1	Plate	11
3.2.2	Stiffened Panel	13
3.3	Constitutive Model	14
3.4	Failure Model	15
3.5	Material Parameter Identification	15
3.5.1	Plate	16
3.5.2	Stiffened Panel	18
4	Preliminary Studies - Part II	19
4.1	Introduction	19
4.2	Eulerian Simulations	20
4.2.1	Computational Fluid Dynamics	20
4.2.2	Numerical Model	21
4.3	Lagrangian Simulations	22
4.3.1	Numerical Model: Plate	23
4.3.2	Numerical Model: Stiffened Panel	24
4.4	Results from CFD	25
4.4.1	Nominal Firing Pressure	25
4.4.2	Resulting Pressure Distribution	27
4.4.3	Resulting Load	29
4.5	Results from CSD	30
4.5.1	Loading Regime	30
4.5.2	Plate	31
4.5.3	Stiffened Panel	32
4.6	Resulting Experimental Programme	34
4.7	Concluding Remarks	35
5	Shock Tube Experiments	36
5.1	Introduction	36

5.2	Measurement Techniques	36
5.2.1	Three-dimensional DIC	36
5.2.2	Background-oriented Schlieren	37
5.3	Rigid Plate	39
5.3.1	Experimental Setup	39
5.3.2	Measurement Inaccuracies	39
5.3.3	Experimental Results	43
5.3.4	Shock Wave Geometry	46
5.4	Plates	48
5.4.1	Experimental Setup	48
5.4.2	Experimental Results	49
5.5	Stiffened Panel	52
5.5.1	Experimental Setup	52
5.5.2	Experimental Results	52
5.6	Concluding Remarks	58
6	Numerical Analysis	58
6.1	Introduction	58
6.1.1	Naming Convention	59
6.2	Load	59
6.2.1	New CFD: Resulting Loading	60
6.2.2	The Griddata-algorithm	61
6.3	Blast Loaded Plate	63
6.3.1	Numerical FE Model	64
6.3.2	Load Evaluation	65
6.4	Blast Loaded Stiffened Panel	66
6.4.1	Numerical FE Model	66
6.4.2	Simulations	66
6.5	Concluding Remarks	70
7	Conclusions and Outlook	71
7.1	Summary and Discussion	71
7.2	Concluding Remarks	73
7.3	Further Work	74
A	Shock Tube Experiments	v
A.1	Rigid Plate	v
A.1.1	Dimensions and Pressure Sensor Location	v
A.1.2	Code for Numerical Filtration and Correction of Pressure Measurements	v
A.1.3	Pressure Measurements	xi
A.1.4	BOS Code	xv
A.2	Plate	xvi
A.2.1	Rigid Body Motions of Shock Tube and Rig Frame	xvi
A.3	Stiffened Panel	xviii
A.3.1	Rigid Body Motions of Shock Tube and Rig Frame	xviii
B	Numerical Analysis	xx
B.1	CFD Load	xx
B.2	Plate	xxi
B.3	Stiffened Panel	xxiii

1 Introduction

1.1 Background and Motivation

Pressure loads with high magnitude, short duration and non-uniform spatial and temporal distribution are commonly referred to as extreme pressure loads. There are numerous sources, both natural and man-made, that may cause extreme pressure loads. Structures have to withstand these loads to prevent for instance casualties, severe material damage and economical loss. Some structures commonly affected by extreme pressure loads are offshore installations as well as protective, ship and aircraft structures. An example of a natural extreme pressure load having fatal consequences due to inadequate structural design is the COSL Innovator drilling rig accident in 2015 [2]. In the incident a horizontal break wave caused one fatality, injuries to four people and extensive structural damage.

Engineering designs of lightweight plated structures are commonly affected by extreme pressure loads that may be potentially fatal. Aluminium alloys are often used in these designs due to their large strength-to-weight ratio, corrosion resistance and formability. To increase the stiffness-to-weight ratio, the plated structures are often multi-stiffened. Stiffened aluminium panels are used as a basic building block in offshore and ship structures, and have therefore been extensively studied since the turn of the decade. Stiffened panels are typically extruded, which creates anisotropy. To form engineering structures, the extruded parts are commonly welded together through metal inert gas welding or friction-stir welding. The heat involved in the welding process alters the material properties along the weld, introducing a heat-affected zone (HAZ). Due to the HAZ and the stiffeners, stiffened panels are complex structures and thus challenging to model accurately. However, accurate modelling is crucial to avoid accidents like the 2015 COSL Innovator accident in the future.

The response of plated aluminium structures have been researched extensively. However, the research on the response due to extreme pressure loads is lacking. To enable lightweight structural designs to withstand extreme pressure loads, a better understanding of the loading conditions and how to model them is required. The complexity of extreme pressure loads make them, and the structural response they cause, challenging to model. Applying a fully coupled analysis simplifies the process, but this is computationally expensive and generally not available to the industry. Sophisticated numerical methods are essential, as they provide engineers with the tools to design safe structures in a cost-efficient manner. However, no numerical method can be trusted without proper a validation, for which observations are required. To this end, extreme pressure loads must be generated and applied to deformable specimens. It is preferable to make the observations in a laboratory environment, as full control of the environmental parameters limits uncertainties.

The aforementioned aspects motivated studies on plated structures subjected to extreme pressure loads. This thesis therefore established a modular test setup with the objective to subject different plated structures to extreme pressure loads of varying complexity and magnitude. With minor alterations, the SIMLab Shock Tube Facility (SSTF) - traditionally used to simulate uniform shock wave events on structures - was able to generate extreme pressure loads in a controlled environment. Tests were conducted on a rigid plate with piezoelectric sensors, deformable aluminium plates and deformable stiffened aluminium panels. The tests were used to characterise the loading conditions and investigate the responses of the deformable specimens. In addition, the results was used to validate new and existing modelling approaches.

1.2 Previous Work

In order to investigate extreme pressure loads and the corresponding structural response of stiffened aluminium panels, it is important to get an overview of previous work of similar studies. There exist numerous papers that investigate structures subjected to dynamic loading for a variety of problems. Several research papers consider variations on structural geometries, structures, loading and boundary conditions. The common objective in the research of extreme pressure loaded structures is to develop an understanding and description of the structural response, the material responses and the loading itself.

It is essential to have an accurate description of the extreme pressure load when studying the response of structures subjected to them. The temporal distribution of an extreme pressure load of short duration is usually applied through simplified models such as square and/or triangle pulses. For instance, blast load events are well explored and the idealized load history can be described with the Friedlander equation [3]. In far-field blast events and in shock tubes, the spatial distribution of the pressure is usually simplified by using a uniform distribution. However, representing the spatial distribution of the extreme pressure load in this thesis is more complicated, because the load history is complex. The spatial distribution is non-uniform, so a uniform load is not valid. Therefore, sophisticated numerical models, preferably in combination with experimental results, need to be used to obtain the load representation. There does not exist any universal method to model the extreme pressure load, since the characteristics of the loading is highly dependent on the loading environment and engineering application.

The dynamic response of structures is evidently dependent on the load intensity. Menkes and Opat [4] conducted experiments on clamped aluminium beams with monolithically increasing high intensity short duration transverse pressure using sheet explosive to obtain uniform loading on the beams. Three different damage modes were identified with increased impulse: large inelastic deformations (Mode I), tensile tearing at the supports (Mode II) and transverse shear at supports (Mode III). Other studies observed that the damage modes were not limited to beams but also occurred in other structures; The same observations were discovered for circular clamped plates by Teeling-Smith and Nurick [5] and their findings supported that the damage modes are dependent on the impulse load intensity. Olsen et al. [6] found the same for square plates and observed an additional characteristic of Mode II, where tensile tearing at supports was first observed at the middle of the edged boundary before advancing along the boundary towards the corners with increasing load intensity. Nurick et al. [7], [8] contributed with further studies on this observation and gave Mode II additions to the amount of tearing at the boundary, reported as Mode II*. Furthermore, for Mode I, they included necking at the clamped supports. In the literature, the categorising of the deformation modes are commonly described and are deemed fundamental.

In quest for a deeper understanding of the dynamic response of beams and plates, studies were carried out by e.g. Jones [9] and further elaborated in [10]. In these studies estimations of permanent transverse deflection of beams and plates are made using approximate methods. This motivated further development of simple theoretical methods for stiffened panels [11]. Yu et al.[12] proposed methods for quick assessments of large inelastic deformations of stiffened panels.

Numerous studies on the response of stiffened panels have been conducted. Nurick et al. [13] performed experiments on stiffened panels where the stiffeners and plate was clamped together before it was exposed to a blast load. Nurick et al. [14] conducted later also more experimental and numerical work on stiffened panels. In this study, a thick plate of hot rolled steel was milled down to fully integrate a stiffener into the plate. The same deformation modes were observed as discovered in [4]. Mode I, permanent large deformations, was mainly detected, but also some examples of Mode II with tensile tearing similar to [6] with increasing impulse. It was also predicted that the critical impulse for Mode II, tensile tearing at the boundary, was found to be independent to stiffener size, which later was seen by Yuen and Nurick [13]. The stiffeners do not reduce the tearing, but restricting the plate to deform plastically, yielding an earlier initiation of tearing.

The structural response of plated structures are greatly influenced by the boundary conditions. Numerous investigations of the effects of loading conditions have been reported. Experimental results for stiffened panels were reported by Schubak et al. [15] , [16], Scheleyer et al. [17] and Pan and Louca [18], [19]. The boundary conditions were deemed important especially for the in-plate (membrane) restraints. Pan and Louca [18], [19] conducted an assessment of boundary conditions and discovered that the activation of membrane strains was important. Moreover, the provision of effective in-plane restraint is more important than bending resistant in order to resist blast loading for stiffened panels.

As the field progressed, more comprehensive experiments have been conducted to account for more realistic problems. The weld is unavoidable in engineering structures and the effect of the associated HAZ is of great interest with regard to the structural response. Paik [20] investigated the compressive strength of welded

aluminium stiffened panels due to imperfections and the softening of the HAZ. Bonorchis and Nurick [21] conducted experimental and numerical investigations on welded stiffeners, and they reported findings of tearing of stiffeners on the base plate. The tearing was mainly dependent on the stiffener height, and the studies showed that residual stresses could be neglected. Morin et al. [1] numerically modelled the HAZ on stiffened aluminium panels and compared it to impact experiments with good correlation.

1.3 Objectives

The objective of this thesis is to contribute to an increased understanding of the dynamic behaviour of plated aluminium structures subjected to extreme pressure loading. Additionally, an objective is to validate to what extent traditional computational methods can predict the behaviour of both fluid and structure subdomains. The extreme non-uniform pressure loading was generated using the SSTF. A new test setup for the SSTF was established in order to generate an extreme pressure load with spatial and temporal distribution. Special focus was provided to predictions of both the loading and the structural response. This will be achieved through relevant theory, experiments and numerical simulations.

1.4 Scope

The topic of behaviour and modelling of plated flexible structures subjected to extreme pressure loads is very broad and cannot be studied as a whole during this thesis work. Therefore, it is necessary to impose some limitations on the present work:

- The extreme pressure loads are limited to the load the SSTF are able to generate.
- Compressible fluid flow and shock physics modelling are not considered.
- Numerical simulations of the extreme pressure load are only performed in the finite element software EUROPLEXUS [22].
- Numerical simulations of the structural response are only carried out in the finite element software ABAQUS/Explicit [23].
- Fluid-structure interactions are not addressed and only an uncoupled approach is used, implying that the fluid and the structure are described separately.

Other restrictions are presented throughout the thesis where needed.

1.5 Thesis Outline

The outline of the thesis is as follows:

Chapter 2, Preliminary Studies - Part I: Introduces the experimental setup and the test specimens. It aims to give a short summary of the development, design and construction of the new experimental setup for the SSTF. A multipurpose setup that accommodates possible further work are established.

Chapter 3, Material modelling: The material model is introduced and the material parameters are identified based on experimental tests.

Chapter 4, Preliminary Studies - Part II: An experimental test programme are developed. Material model and the new setup is implemented in numerical models. Better understanding of the physics of the problem are obtained with the use of numerical tools. EUROPLEXUS is used for modelling the fluid inflow and ABAQUS/Explicit is used for modelling the structure.

Chapter 5, Shock Tube Experiments: Description of the shock tube experiments are given in this chapter. Results of the experiments from the laboratory work on a rigid plate, deformable plates and stiffened panels are presented. The shock tube experiments carried out are described.

Chapter 6, Numerical analysis: The experimental program will be performed numerical. This serves as a final numerical study of the problem. It utilises numerical results and work from previous chapters. An uncoupled approach is used for modelling the problem. The experimental results are compared to the numerical results.

2 Preliminary Studies - Part I

The SSTF will be used to generate the extreme non-uniform pressure load. However, since these kind of test had not been carried out before the work of this thesis, a new arrangement had to be constructed before deciding experimental programme. This chapter is therefore devoted to present the work done in order to design the experiment setup.

2.1 Introduction

Before experimental test on the stiffened plate were to be conducted, a new rig for the SSTF and test specimens had to be designed. The loading are usually assumed uniform and the temporal distribution of the load is usually characterised by the Friedlander equation [3] in the SSTF. From a structural engineering perspective the dynamic response of plates subjected to such loading are regarded as known. However, the loading is often of great uncertainty and involves several assumptions. The stiffened plate has not been investigated before in the extreme pressure events at SIMLab. Therefore, a simple plate structure will be introduced. The plate will be used to see if the complex load is interpretation correctly. The plate are believed to be more sensitive to the load.

Substantial amount of work was spent on the design of the test and major choices regarding the design will be discussed and summarised in this chapter. This included boundary conditions, dimensions on test specimens and the rig, but also practical considerations. In order to accomplish this, assumptions were made, and preliminary assessments were conducted. Several different designs were evaluated for the purpose to achieve the optimal solution. The final experimental setup will be presented lastly. First, a short description of the SSFT will be given before the test structures are presented.

2.2 The SIMLab Shock Tube Facility

All tests were conducted in the SIMLab Shock Tube Facility (SSTF), located at the Department of Structural Engineering, NTNU. A detailed description of the facility as well as performance evaluations can be found in [24]. In Figure 2.1 an overview of the SSTF and its components can be seen in a traditional setup. The tube consists of three main parts, all of which is made out of stainless steel. The first part of the SSTF is the driver section, a high-pressure chamber with modular length, located at the far left. In this study the length of the driver section was 1.27 m. The firing section, which is made up of a series of intermediate chambers divided by diaphragms, separates the driver section from the rest of the tube. Following the firing section is the driven section, a 16.20 m long low-pressure chamber. The driver section ends inside a dump tank. The experiment is carried out in two steps. First the driver and firing sections are filled with compressed air, during which the multiple chambers in the firing section induce a step-wise pressure gradient between the driver and driven sections. When the desired driver pressure is reached, controlled rapid venting of the chamber closest to the driver section causes the pressure to consecutively rupture the diaphragms and form the shock wave. A small ratio between the driver and driven lengths ensures the pressure profiles of the shock wave to resemble the ones from an far-field explosive detonation [24].

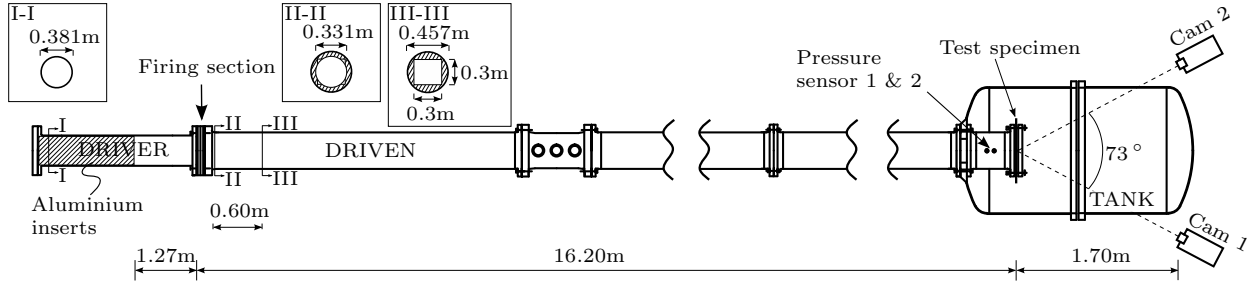


Figure 2.1: Overview of the SIMLab Shock Tube Facility with a traditional test setup [25].

As explained by Aune in [24] “A closed-end configuration of the SSTF is favourable to avoid leakage of pressure in the circumferential direction of the test specimens at the blast-structure interface and will therefore maintain a uniform and plane shock wave also around the perimeter of the tube. Placing the test specimen even the smallest distance from the end of the tube would lead to a non-uniform spatial and temporal distribution around the periphery of the tube, due to partial venting of the gas into the expanding tank volume (see [118,120]). Moreover, such a venting results in rarefaction waves travelling back upstream the tube causing increased complexity of the subsequent wave patterns.”. Therefore an open-end configuration is employed in this study to achieve the desired extreme pressure loads complexity. To further increase the complexity obstacles can be mounted at the the driven section outlet.

2.3 Test Structures

The aluminium alloy 6082(AA6082) is a widely used alloy in numerous industries, due to its advantageous properties. The alloy has high strength-to-weight-ratio, excellent corrosion resistance and sufficient plasticity for extrusion. In addition it is well suited for welding, machining and forming. Its grain structure is fine, which ensures good resistance to dynamic loading conditions. Its mechanical properties are comparable to regular offshore steels, which combined with its low density and corrosion resistance has made stiffened panels of AA6082 very attractive in offshore structures. The nominal chemical composition of the alloy is given in Table 2.1. Both the plate and the stiffened panel investigated in this thesis was made out of the aluminium alloy AA6082 with T6 tempering (AA6082-T6). The T6 tempering denotes that the alloy has been heat-treated and artificially aged to meet material property standards. As the manufacturers and production methods were different, the materials of the structures had to be characterised separately.

Table 2.1: Chemical composition of AA6082-T6 [wt.%]

	Si	Fe	Cu	Mn	Mg	Cr	Zn	Ti	Others
Min. [%]	0.70			0.40	0.60				0.05
Max. [%]	1.30	0.50	0.10	1.00	1.20	0.25	0.20	0.10	0.15

2.3.1 Plate

The 2-mm-thick aluminium plates were formed by cold-rolling by the Chinese manufacturer Alnan Aluminium Inc., and milled into 625 mm x 625 mm squares. The manufacturer listed the nominal yield strength in the order of 304 - 317 MPa and the nominal tensile strength in the order of 328 - 337 MPa.

2.3.2 Stiffened Panel

The stiffened aluminium panels are composed of extruded profiles, which were assembled by use of friction-stir welding. The welding process introduces a HAZ with lower material strength than the unaffected material.

The original panel consists of five extruded profiles, as shown in Figure 2.2a, but they were milled to the geometry in Figure 2.2b to get suitable dimensions for testing in the shock tube facility. The stiffeners has a thickness of 3 mm, while the base plate is 4 mm thick.

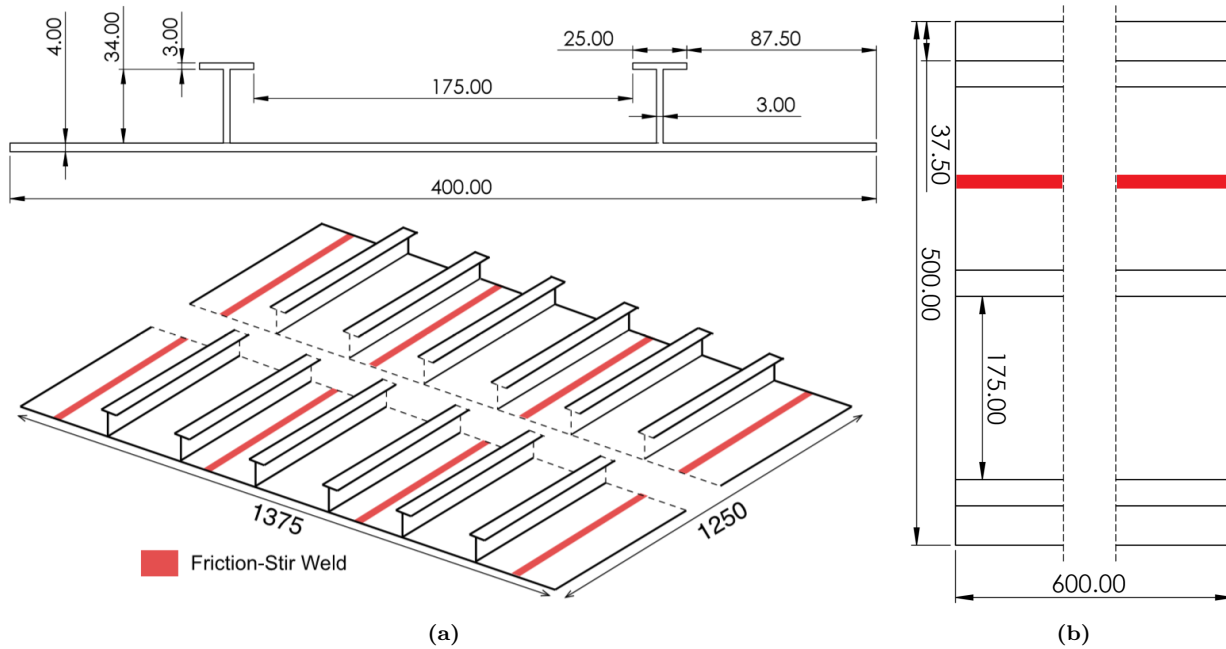


Figure 2.2: (a) Illustration of the extruded profile and the assembled panels. (b) Illustration of the milled panels tested in the shock tube facility.

2.4 Summary of Design History

The setup was constantly evolving, and several revisions and iterations of the rig setup were created due to various considerations that emerged during the design phase. Literature studies and parametric studies of simplified numerical models were used for the concept analysis. Several conditions arose through the work. A short summary of important factors in the design phase will be given in this section. In Section 2.5, the final setup is presented.

2.4.1 Concept Analysis

Introductory studies were conducted in order to acquire knowledge of the expected behaviour and response of both the plate and the stiffened panel, but also the rig itself during an extreme pressure event. Several considerations were investigated numerically and through literature in the design phase.

The same numerical shell models of the plate and panel - as described in Section 4.3 - were used in the design phase. An introductory load was applied. The loading was simplified and based on previous experiments in the SSTF. In previous experiments in the SSTF, a pressure-time history of a planar shock wave at the end of the tube has been registered and utilised in introductory studies. The pressure load was applied as an idealised pressure wave. Only the positive phase of the blast load was used. To represent the pressure-time history, the modified Friedlander equation [26] and [3] were employed. The pressure sensor data was idealised through curve-fitting of the modified Friedlander equation. To make the imposed load non-uniform, the exposed pressure area was partitioned into 25 subareas, with uniform pressure within each subarea. The magnitude was altered within the subareas to replicate different non-uniform loads. The largest magnitude of an open configuration of the driven tube was found in the subarea in the middle. For a wall configuration,

where half the tube is blocked, the centre of the pressure was altered and transferred away from the centre. The magnitude intensity of the remaining subareas was reduced by a third as the distance to the subarea with the greatest magnitude increased. For simplicity, the idealised pressure load was scaled with regard to peak pressure in the range 200 to 1200 kPa, and hence, altering the intensity of the load.

Using the introductory numerical models, details of the setup were investigated. Parametric studies of the structural response, using different load intensity and spatial distribution, were explored, as well as parametric studies of boundary conditions. Studies of setup oscillations were conducted. Lastly, the numerical model was used to iterate and dimension the final design.

Great efforts were made to design the fixtures and setup. It was important to have a simplified system in order to minimise the unknown and the complexity. Easy boundary conditions were emphasised so that the numerical modelling would be less complicated when conducting the numerical validations of the experimental results at a later stage. Taking this into account, previous work on panels were studied to discover fixtures that had been previously used to support panels. Wadley et al. [27] used clamping frames with through bolts for fully edge clamped sandwich panels. The bolts are there to restrain the in-plane movements. Nurick et al. [14] did not use a clamping frame but milled out stiffeners in a thick plate that was fixed with bolts. Others have welded the edge to fixed blocks. Another possible solution is to clamp the plate between two beams with a bolt attached to a rigid base, as done by Morin et al. [1] and master theses [28] and [29]. Teflon is introduced on the contact surface to reduce the friction, imposing no restrictions on the in-plane deformation of the panels.

All the above-mentioned fixtures have some form of restraints; bending restraints and/or membrane restraints. The development of membrane actions depends on the stiffness of the support frame. With large inelastic deformations, membrane forces are substantial, and the membrane restraint dominates the response. Increasing the restraint may result in considerable deflection of the supports if not properly designed. It is important to accurately define the boundary condition in order to achieve better agreement between experimental and numerical results. Louca et al. [19] conducted a numerical parametric study of the effect of different boundary conditions with different restraints on stiffened panels subjected to blast events. The response varied considerably depending on the edge restraint, and was emphasising the importance of a simple fixture.

2.4.2 Design Considerations

Based on considerations that appeared during the design phase, both in practice and through concept analysis, the dimensions and details of the final setup were determined. A summary of the major design considerations are given in this section.

Initially, when designing the experimental setup, test structure dimensions had to be decided. SIMLab had stiffened aluminium panels in their inventory from the project by Morin et al. [1], and the master theses [28] and [29]. Hence, determining whether these panels were suitable for our study was a natural starting point, as conducting the experiments on them would reduce both time and cost. Preliminary investigations of the response using loads that are assumed achievable by the SSTF gave large inelastic deformations with simply supported boundary conditions. The panel will be used.

Spatial distribution of the shock wave front was considered in the determination of distance between shock tube opening and test specimens. It was a compromise of intensity and spherical evolution. It was wanted a distance that was large enough for a non-uniform shock front to evolve and be able to cover the exposed area, but at the same time not lose too much intensity. Load intensity decreases greatly with distance. Computer fluid dynamics (CFD) simulations will later be used along with experimental measurements using pressure transducers and Background-oriented Schlieren techniques to verify the spatial distribution of the shock wave on a rigid plate.

Several considerations were effecting the decision when the size of the exposed pressure area of the panel was to be determined. It was desirable to have it greater than the free opening of the shock tube (300 x

300 mm) so the non-uniform pressure load can develop. The setup had to be adequately accommodated for with the existing limitations of the laboratory equipment with regard to the size and practical restrictions. Accordingly, the dimensions of the exposed area was set to be 500 x 500 mm based mainly on practical considerations.

It was desirable to have a setup that could accommodate for generic testing of several different plate structures. Making it modular and adaptable will emphasise a more efficient and economical execution of experiments. It was also desirable to measure the reacting forces of panel subjected to a shock wave. The setup was designed to accommodate for the load cells Kistler 9041A. The boundary condition for the test specimens was comprehensively investigated. As stated in Section 2.4.1 several boundary conditions was regarded and evaluated. Major design changes can be categorised into three revisions. The first was fully clamped and fixed with axial- and rotational restraints with a through bolt. This gave large forces on the supports. The second was rotation fixed supported without axial restraints, similar to the clamping fixture in [1]. This was a complex boundary condition which may be hard to model with sufficient accuracy. The third was simply supported without axial- and rotation constraint. All the above mentioned concepts only supported the panel on two sides - stiffeners resting on the support - to further simplify the boundary.

The simply supported design was determined to be best suited. Introducing restraints of the panel would dramatically increase the load needed to induce large inelastic deformation and expose the load cells to large shear stresses which is not desirable. The simply supported design added minimal modelling uncertainty to the problem. The setup will primarily deflect in the loading direction which will be accounted for in the experimental test. Due to gravity the panels had to be barley taped to the test rig, but the tape was assumed to have negligible impact on the test.

Shock waves without any disturbance have been subject to considerable research in the SSTF. To obtain more complex and realistic load case, obstacles were inserted in front of the structure to provoke the shock wave and to study the influence of this type of loading on the structural response. In real blast event the extreme pressure are not uniform with a known load history. Several obstacle can provoke the shock wave and alter its characteristics before it hit a engineering structure of interest. Initially, three different load obstacle configurations was assessed. One where half the opening are blocked, one where a column is blocking the middle tired and one which is open, respectively referred to as wall, column and open configuration. In Figure 2.3a and Figure 2.3b the wall and column configuration are illustrated. The column was not used further due to practical restrictions.

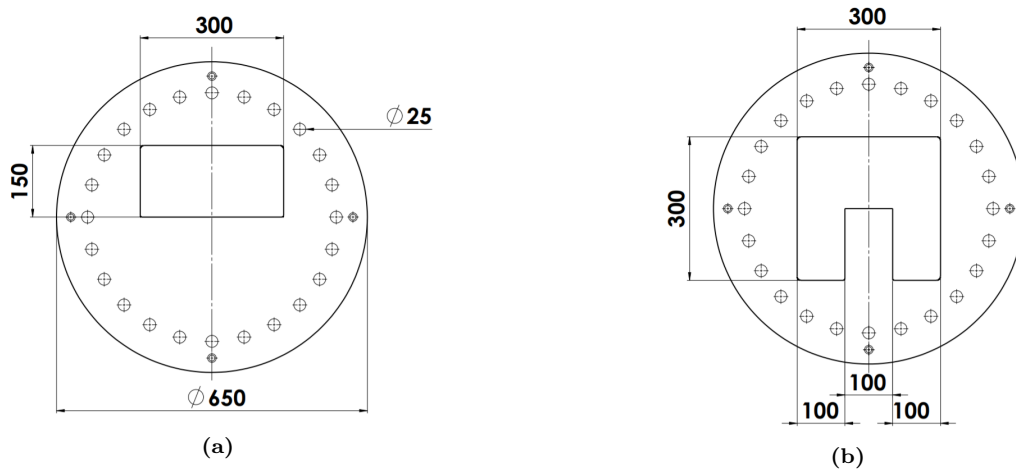


Figure 2.3: Illustration of the two driven outlet configuration (a) wall and (b) column.

As the nonuniform pressure wave expand into the tank, the pressure decays towards equilibrium pressure

which is the ambient pressure, but due to the momentum of the fluid it may get an over expansion and result in a pressure below the ambient pressure, resulting in a negative phase. Thus, a claw was designed to capture the panels for possible back bounce. Parametric studies was conducted to dimension the claws as close to the panel as possible without touching the panel through the entire loading event.

Due to the complexity of the load it was considered useful to perform a validation step of the interpretation of the load by comparing structural responses from numerical model to experimental results on a simpler structure, than the stiffened panel. As mentioned, a plate was introduced for this purpose and to be consistent with previous work in the SSTF. The experimental setup for the plate will be fixed with clamping frames and through bolts as previously done in the SSTF.

Summary of Concluded Major Guidelines

- Stiffened panel from in house storage.
- The stiffened panel should have no restrictions in bending and membrane actions
- Unstiffened plate should also be accommodated with boundary conditions consistent with previous work from SIMLab (clamped with bending and in-plane restraints).
- Exposed area is limited to 500 mm x 500 mm
- Distance from shock tube opening should be sufficient for non-uniform (spherical) shock front to develop.

2.5 Summary of Final Setup

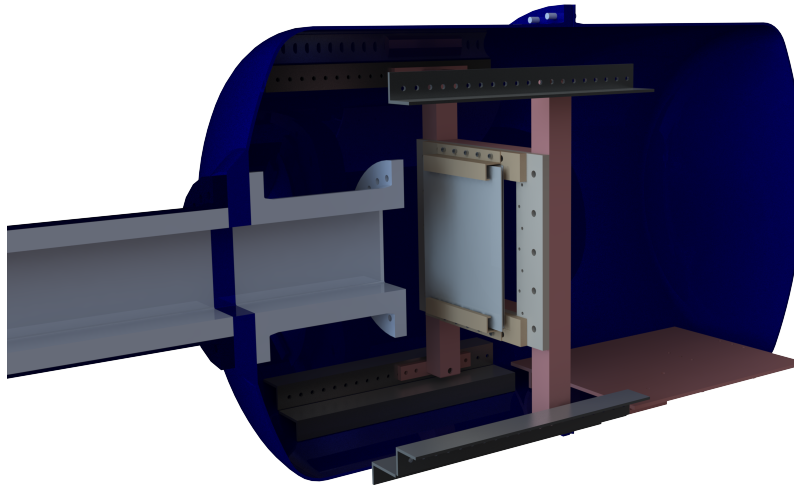


Figure 2.4: The new experimental set up inside the dump tank of the SSTF.

The experimental rig-setup will be produced by Heimdal Industriservice based on a computer-aided design (CAD) model created in SOLIDWORKS [30] and technical drawings created through the design phase.

As a summary of the final experimental rig set up, a rendered CAD model will be shown as an illustration. Figure 2.4 illustrate the stiffened panel in the dump tank with the open configuration. Figure 2.5 illustrates the three configurations: the rigid plate, the plate and stiffened plate, respectively.

Construction started with a base frame for all configurations, as shown in red in Figure 2.4. It was created based on practical restrictions in the dump tank. Base supporting frame consist of a two vertical and two horizontal square hollow steel sections (100 mm width, thickness 10 mm) welded together. Bolt holes was created to accommodate for the three different configurations in Figure 2.5. The base frame are bolted to the dump tank with four M24 bolts through different spacers that alter the distant from the shock tube opening to be 250 mm for all three configurations. In Figure 2.5a the dimensions of the base frame are illustrated.

The deformable plates has the same back plate. The back plate is a 30 mm AA6062 plate that is bolted with 20 M24 12.9 steel bolts to the base support rig frame. It has bolt holes for the clamping frame (plate) and the support blocks (panel) and a cut out of 500 mm x 500 mm for the exposed pressure area.

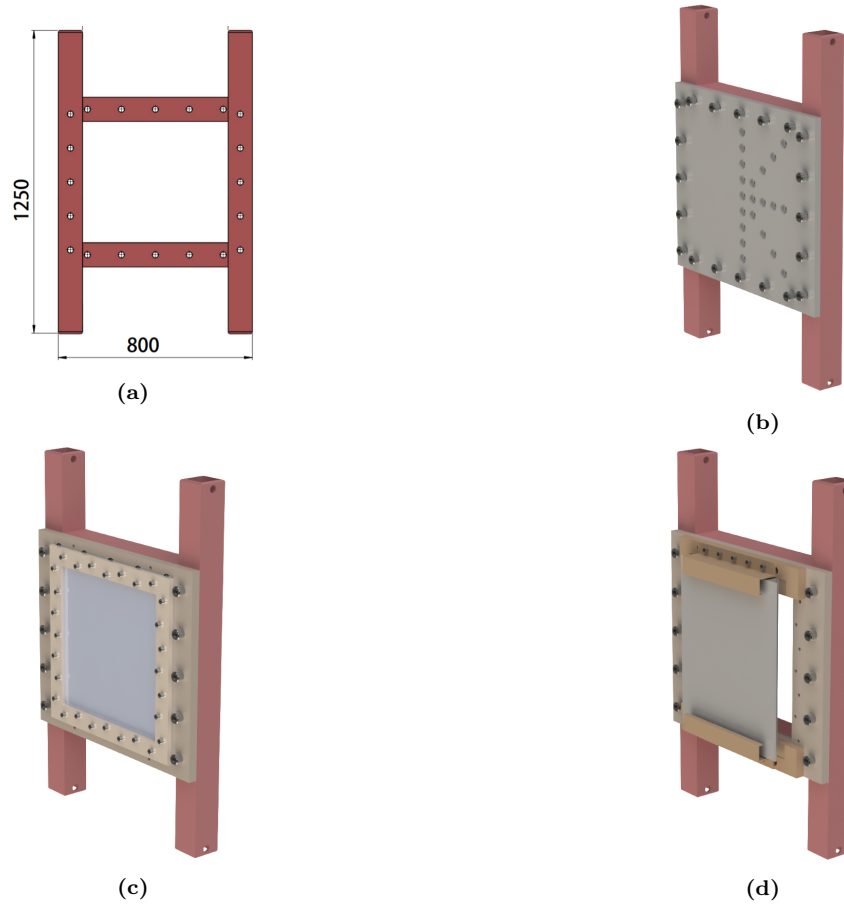


Figure 2.5: Dimensions of the base frame are shown in (a) and the three configurations of the setup: rigid plate, plate and stiffened plate are illustrated in (b), (c) and (d), respectively.

3 Material Modelling

This chapter covers the constitutive models and computational framework for modelling the test material. A description of the aluminium AA6082-T6, material tests, and a presentation of the calibrated material parameters used in this thesis will be given.

3.1 Introduction

The material model presented in this section is an isotropic and rate- and pressure-independent elastic-plastic model. These restrictions were added to limit the necessary experimental work, while remaining able to assemble a reliable material model for aluminium alloys. The same material model was used for both the plate and all parts of the stiffened panels, but the material parameters differed. The theory of plasticity has three main parts: a yield criteria, a flow rule and a work-hardening rule. These parts will all be defined for our model, in addition to a fracture criteria.

In addition the material parameters of the material model are identified through uniaxial tension testing and subsequent reverse engineering.

The constitutive model was implemented in ABAQUS [23] through a in-house user-defined material model for 3D and plane stress states. For temporal integration of the constitutive relations the cutting-plane algorithm [31] and a semi-implicit algorithm [32] was used in ABAQUS/Explicit and ABAQUS/Standard respectively. A sub-stepping scheme, was implemented to guarantee an accurate stress update. The sub-stepping scheme limits the maximum allowable incremental deviatoric strain tensor to a certain ratio of the strain to yielding. The ratio was set to 10% for the explicit scheme and 1% for the implicit scheme. The scheme reduces unacceptable strain increments to the maximum allowable value by sub-stepping.

In ABAQUS/Explicit failure and crack propagation was handled by removing elements. If the damage variable D reached unity in an integration point, the stress tensor was set to zero. If all the integration points of an element fail, the element was discarded. The method creates some noise in the calculated forces of simulations with failure, as the procedure of instantly setting the stress tensor to zero releases stress waves into the remaining mesh.

3.2 Uniaxial Tension Tests

3.2.1 Plate

In order to identify the material parameters for our numerical model, uniaxial tensile tests were carried out on dog-bone specimens milled from the aluminium plates. The tests were performed in a Zwick/Roell Z030 test machine with 2.1 mm/min loading velocity, which corresponds to a strain rate of $\dot{\epsilon} = 5 \cdot 10^{-4} s^{-1}$ for a specimen with 70 mm gauge length. The test machine measured both force and displacement, while a camera was set up to provide pictures for a displacement field through a DIC analysis. Only the displacement data from the DIC was used to characterise the material, as Aune validated its accuracy with the exact same test setup by utilising an extensometer in [24]. The test setup and the geometry of the dog-bone specimen can be seen in Figure 3.1a and 3.1c, respectively. A total of nine tests were carried out on specimens from three different directions (0°, 45° and 90°) in relation to the rolling direction. The cause for testing three different directions was to determine the degree of anisotropy.

The in house Digital Image Correlation (DIC) software, eCorr [33] was used to extract strain data from the tensile test. How the software works will be further explained in Section 5.2.1. Figure 3.1b shows how the strain data was extracted by using a virtual extensometer vector with an approximate gauge length of 60 mm (2389 pixels) on a meshed specimen. Three transverse vectors are also shown, which were used to measure the gauge width at different points in pixels. These measurements were compared to the physical measurements at the same points in order to obtain the mm/pix relation, which enabled the DIC to output measurements in mm.

As can be seen in Figure 3.2 the plate material acted highly isotropic. The engineering strain was calculated from Equation (3.1), where ϵ_e is the engineering strain, u is the displacement and L_0 is the initial gauge length. The strain at fracture differs slightly for the tests taken in the same direction, but this is expected as the fracture strain is dependent on stochastically distributed material defects like microvoid density and heterogeneties[34]. However, the behaviour until loss of stability for each direction is identical. In comparison to each other the maximum force of the tests taken from the 0° direction is 1.3% and 2.3% higher than the

maximum force of the tests taken from the 90° and 45° directions, respectively. The shapes are also very similar, as evident by the representative comparison between tests from the three directions in Figure 3.2d.

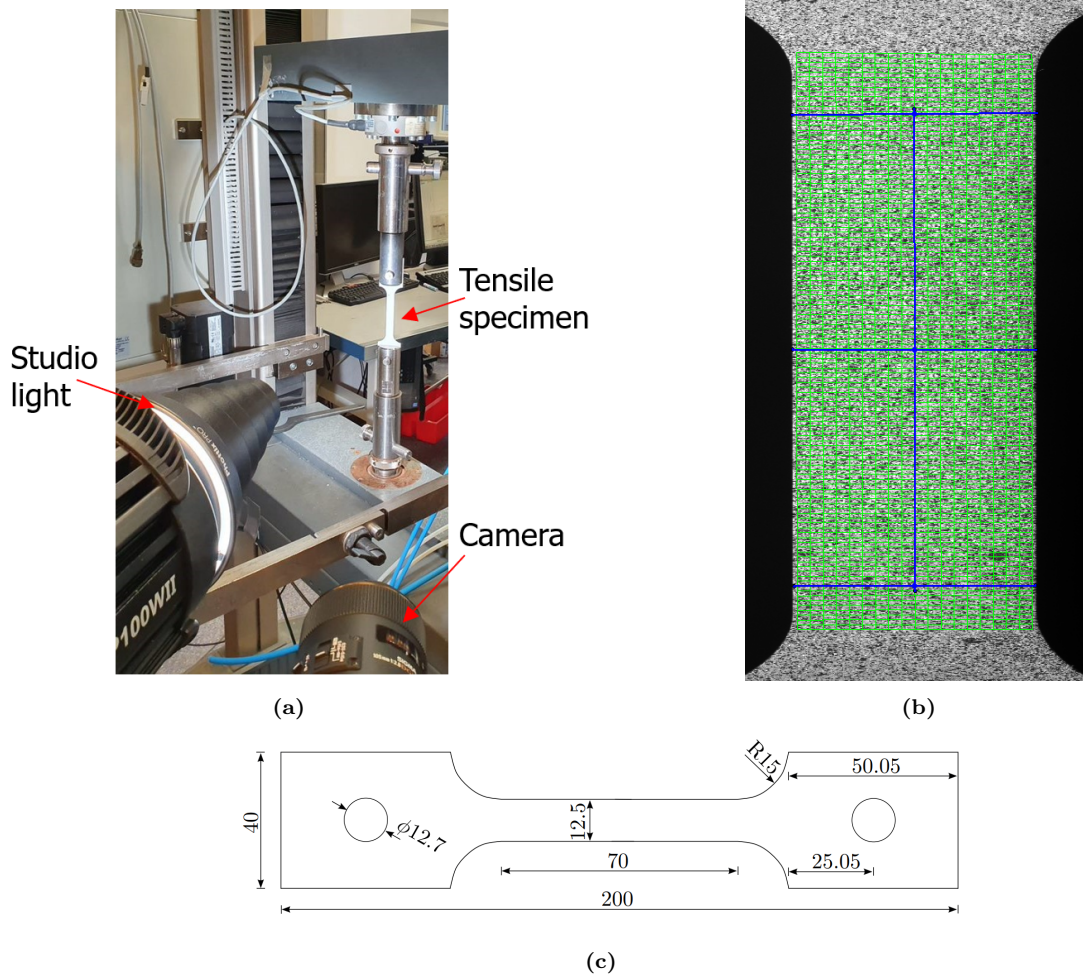


Figure 3.1: (a) Experimental setup for the material tests. (b) Resulting view from eCorr for a representative tensile test (test 1, 45 deg). Strain was extracted by the vector along the specimen (virtual extensometer) and correlating to loading history to obtain strain force history. Transversely vectors are for approximate the mm/pixel relation. (c) Geometry of the dog-bone specimen.

The equivalent strain for the three representative tests are shown until necking in Figure 3.2e and Figure 3.2f, plotted against total strain and plastic strain, respectively. These curves has been calculated by applying the equations (3.1) to (3.5). σ_e is the engineering stress, F is the force, A_0 is the initial minimum cross-section area of the gauge section and σ is the equivalent stress. ε is the true strain and E is Young's modulus, while ε^p is the true plastic strain. The equations concerning true values are only valid until necking.

$$\varepsilon_e = \frac{u}{L_0} \quad (3.1)$$

$$\sigma_e = \frac{F}{A_0} \quad (3.2)$$

$$\varepsilon = \ln(1 + \varepsilon_e) \quad (3.3)$$

$$\sigma = \sigma_e(1 + \varepsilon_e) \quad (3.4)$$

$$\varepsilon^P = \varepsilon - \frac{\sigma}{E} \quad (3.5)$$

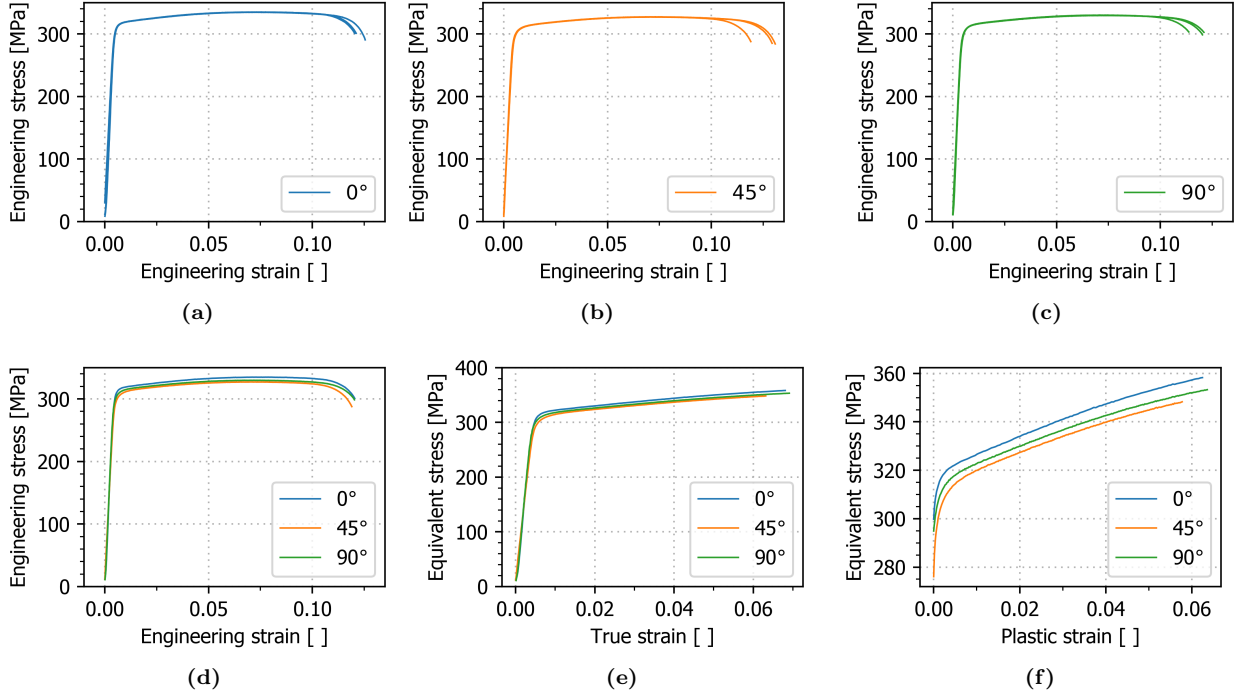


Figure 3.2: ((a)-(c)) Force - engineering strain curves for the three tensile tests executed for each of the tested directions. ((d)-(f)) Curves from a representative tensile test from each of the tested directions: (d) force - engineering strain, (e) equivalent stress - true strain, (f) equivalent stress - plastic strain.

3.2.2 Stiffened Panel

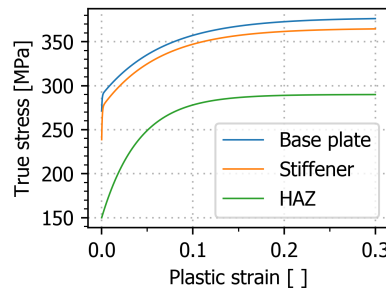


Figure 3.3: Illustration of the plastic hardening behaviour of the three material sections of the stiffened panel.

Morin et al. [1] investigated the material properties of the stiffened aluminium panels used in this study by performing tensile tests. The material behaviour in three different directions (0°, 45° and 90°) of the base plate regarding the extrusion direction of the panel was compared, and quite large anisotropy in the yield stress and some anisotropy in the plastic flow was found. The behaviour of the base plate material was

compared to the behaviour of cross-weld tensile specimen and stiffener material specimen, and it was found that the HAZ reduced the yield stress and increased the work-hardening, while the stiffener material showed a lower yield stress but a similar work-hardening. The plastic hardening behaviour of the different material sections are visualised in Figure 3.3. The effect of the HAZ was similar to the effect found in previous research on AA6082-T6 [35].

3.3 Constitutive Model

The yield limit is described mathematically as

$$f(\boldsymbol{\sigma}, p) = \varphi(\boldsymbol{\sigma}) - (\sigma_0 + R(p)) = 0 \quad (3.6)$$

where the yield function f is a continuous function of the stress tensor $\boldsymbol{\sigma}$ and the equivalent plastic strain p . $\varphi(\boldsymbol{\sigma})$ is the equivalent stress, σ_0 denotes the initial yield stress and R the isotropic hardening function. The yield function is restricted to

$$f(\boldsymbol{\sigma}, p) \leq 0 \quad (3.7)$$

where $f(\boldsymbol{\sigma}, p) < 0$ describes the elastic domain.

The three most common yield criteria in material modelling are the von Mises, Tresca and Hershey-Hosford criteria. The work done by Saai et. al. indicates that the Hershey-Hosford yield criterion closely replicates the yield surface of an aluminum alloy [36]. The Hershey-Hosford yield criterion, also called the high-exponent yield criterion, is a product of generalising the von Mises yield criterion. The Hershey-Hosford equivalent stress reads as

$$\varphi(\sigma_1, \sigma_2, \sigma_3) = \left(\frac{1}{2} (|\sigma_1 - \sigma_2|^m + |\sigma_2 - \sigma_3|^m + |\sigma_3 - \sigma_1|^m) \right)^{\frac{1}{m}}, \quad m \geq 1 \quad (3.8)$$

where σ_1 , σ_2 and σ_3 denote the principal stresses and m is a material parameter which for materials with face centered cubic crystal system like aluminium is equal to 8 [37]. The Hershey-Hosford yield criterion is equal to the von Mises criterion for $m = 2$ and converges to the Tresca criterion as m approaches the limits 1 and ∞ . All three yield surfaces are visualised in Figure 3.4 for a plane stress condition.

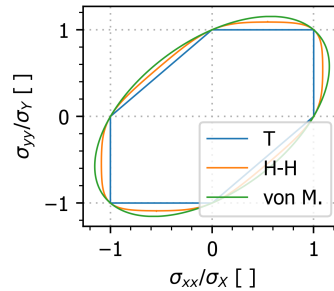


Figure 3.4: Illustration of the yield surfaces of Tresca, Hershey-Hosford (with $m = 8$) and von Mises in the plane stress space ($\sigma_{zz} = 0$).

In this study the von Mises criterion was implemented due to convenience and the modelling uncertainties being larger than the assumed difference between the von Mises and Hershey-Hosford criteria.

The plastic flow rule, which ensures non-negative dissipation, is described mathematically as

$$\mathcal{D}_p = \boldsymbol{\sigma} \dot{\boldsymbol{\epsilon}}^p \geq 0, \quad \dot{\boldsymbol{\epsilon}}^p = \dot{\lambda} \frac{\delta g}{\delta \boldsymbol{\sigma}} \quad (3.9)$$

where \mathcal{D}_p denote the plastic dissipation, $\dot{\boldsymbol{\epsilon}}^p$ denote the plastic strain rate tensor, $\dot{\lambda}$ the plastic multiplier and g the plastic potential function. Both the plastic multiplier and the plastic potential function are non-negative. The associated flow rule, where the plastic potential function is defined by the yield function, was applied in this material model. The following proves that non-negative dissipation is achieved for the associated flow rule as both the plastic multiplier and the equivalent stress is non-negative by definition.

$$\mathcal{D}_p = \boldsymbol{\sigma} \dot{\lambda} \frac{\delta f}{\delta \boldsymbol{\sigma}} = \dot{\lambda} \boldsymbol{\sigma} \frac{\delta \varphi}{\delta \boldsymbol{\sigma}} = \dot{\lambda} \varphi \geq 0 \quad (3.10)$$

To describe the work hardening of the material an extended Voce rule was utilized, which is described mathematically as

$$R(p) = \sum_{i=1}^{N_R} R_i(p) = \sum_{i=1}^{N_R} Q_i (1 - e^{-\frac{\theta_i}{Q_i} p}) \quad (3.11)$$

where Q_i and θ_i denotes the saturation stress and the initial work hardening modulus of the hardening term R_i , respectively. N_R denotes the number of hardening terms. Two terms were used for the both the plate and all parts of the stiffened panel, except for the HAZ, where one term was deemed sufficient.

3.4 Failure Model

In order to model failure an uncoupled damage evolution rule was applied. That is, the Cockcroft-Latham criterion [38] which is described mathematically as

$$\omega = \frac{1}{W_C} \int_0^p \langle \sigma_I \rangle dp \quad (3.12)$$

is a convenient criterion of this type of damage evolution rule, as only the fracture parameter W_C has to be calibrated. $\langle \sigma_I \rangle = \max(\sigma_I, 0)$ and σ_I denotes the major principle stress. Failure is assumed to occur when $\omega = 1$, thus the fracture parameter quantifies the tolerable measure of "plastic work" per unit volume. The unit volume in a FE analysis is the element volume, hence the fracture criterion is mesh dependent.

The Cockcroft-Latham criterion accounts for the primary aspects of ductile failure under plane stress conditions. However, the criterion is not suited to predict failure in uniaxial compression, lower stress triaxiality or pure shear. Thin-walled structures, as both the plates and stiffened panels are examples of, usually conform compression and shear loading by buckling leading to a locally tensile-dominated problem. Therefore the Cockcroft-Latham criterion is a sufficient failure model for the studies conducted in this thesis.

3.5 Material Parameter Identification

In order to apply the material model nine material parameters must be identified. For the plates σ_0 , $\theta_{i=1,2}$ and $Q_{i=1,2}$ was determined through reverse engineering of the tensile test using a FE model, while the remaining parameters were taken from literature [39] [40]. The work done by Morin et al. [1] was adopted for the stiffened panels.

3.5.1 Plate

The material parameters of the plate were determined by reverse engineering one of the tensile tests. The perpendicular tensile test in Figure 3.2d was chosen, and is henceforth referred to as the target curve. The target curve was deemed representative for the material on account of it being close to the median both in regard to the maximum force and the fracture strain. The FE model of the tensile test was established in the FE-software ABAQUS/Standard [23]. By assuming isotropy and the necking propagating perpendicular to the loading axis, modelling 1/8 of the specimen was sufficient due to symmetry. 8-node linear brick elements with a characteristic size of 0.6 mm were used globally in order to get 3 elements over the thickness, while biased meshing was applied along the gauge length with a minimal characteristic size of 0.3 mm. To decrease the computation time and improve accuracy reduced integration with hourglass control was utilised [41]. The specimen was loaded by a pinned connection modelled as a discrete rigid shell, and meshed with a characteristic size of 2 mm. The contact between the pin and the specimen was defined by utilising the surface-to-surface algorithm with "Hard" contact and penalty friction formulation with a conservative friction coefficient of 0.05. The model is displayed in Figure 3.5. The modelling procedure was inspired by Morin et al. [1].

The yield stress and extended Voce rule parameters were all found by utilising the non-linear least squares method *optimize.curve_fit* [42] from the Python-based open-source software collection *Scipy*. Figure 3.6a displays the work hardening curves resulting from curve fitting the parameters to the target curve data plus an additional point. The additional point was added to increase the hardening effect, as the FE analysis (FEA) conducted with the raw curve fit parameters underestimated the hardening of the material. Figure 3.6b displays the force - engineering strain from the FEAs with different hardening parameters compared to the target curve. Adding the point (0.25, 400) gave hardening behaviour close to the target curve, as can be seen from the red curve. Beyond the maxima of the target curve (necking) the behaviour of the red FEA diverges slightly, as its maxima is reached at a higher strain value. To obtain a better fit a three term Voce rule could have been implemented, but the constitutive model was deemed sufficient considering the assumption of isotropy. The red FEA curve from Figure 3.6b is displayed alongside all the conducted tensile tests in Figure 3.6c, and the material parameters can be seen in Table 3.1.

Fracture is a highly localised effect and therefore requires a sufficiently fine mesh to be represented accurately in a FEA. Describing the physics of the fracture accurately is impossible without a fine mesh, but fracture can still occur at the correct strain level with a coarser mesh. Hence modelling fracture is mesh dependent, and the same holds true for the Cockcroft-Latham criterion. As described by Gruben et al. [43], the mesh dependent parameters is conveniently handled with a computational-cell approach, i.e., keeping the element type and size constant in both calibration and application of the failure model. Therefore failure parameters are typically calibrated by utilising the same elements in tensile test FEA as component FEA. Uniaxial tensile tests on flat tensile specimen must be modelled with element length smaller than the specimen thickness to capture local necking and failure accurately. Modelling the tensile test with shell elements is possible, but would require the use of non-local regularisation to avoid unreasonable thinning [35]. However small shell elements combined with non-local regularisation is not better suited to model large plates than solid elements, which is highly impractical due to exorbitant computation times. Thus, an alternative method had to be applied.

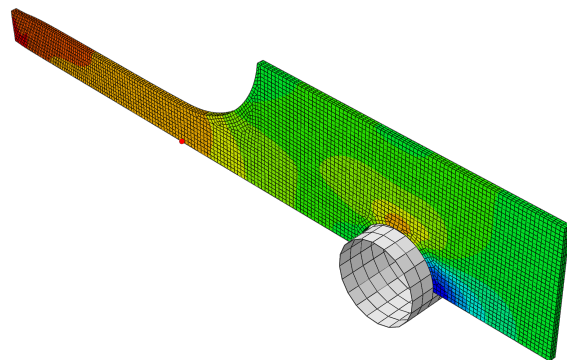


Figure 3.5: Picture of the ABAQUS/Standard model of the tensile test used for the reverse engineering. The red dot marks the node from which the strain was calculated.

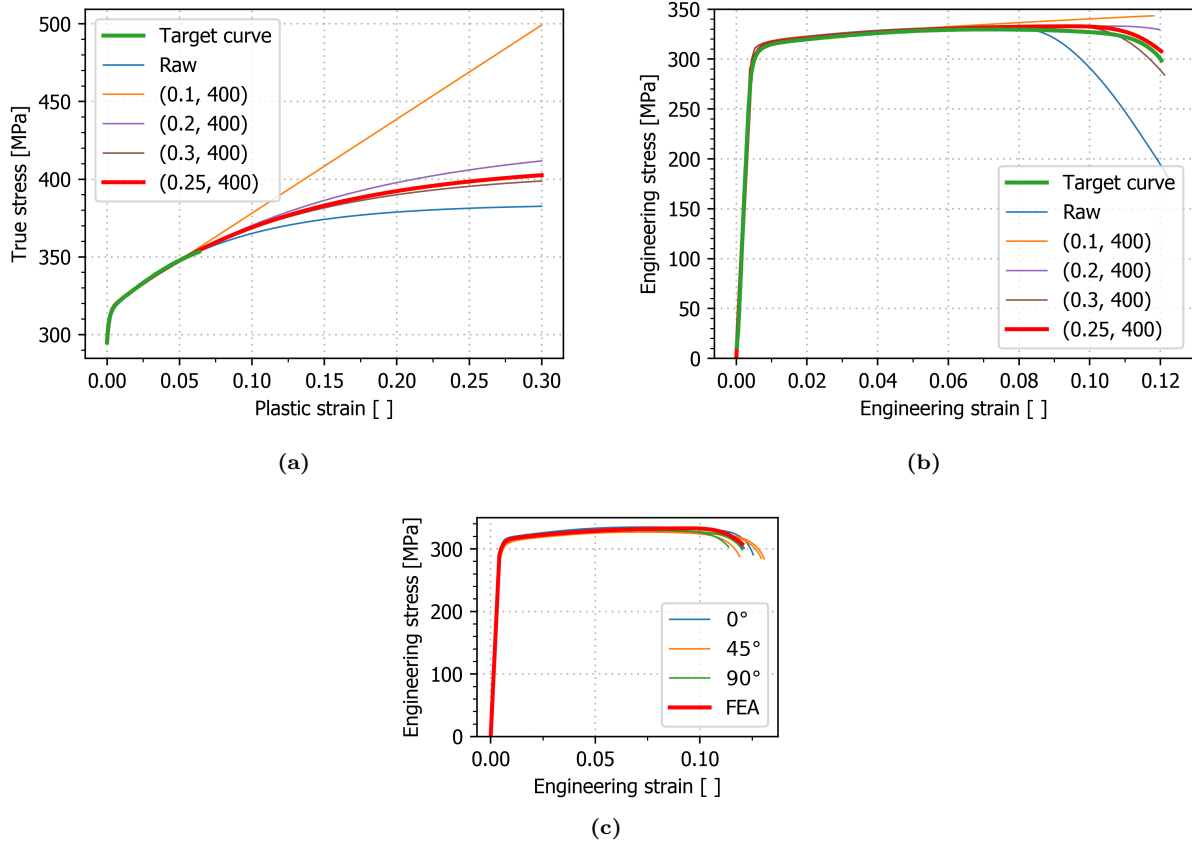


Figure 3.6: (a) True stress - plastic strain curves for the work hardening behaviour resulting from curve-fitting the two term Voce rule to the target curve and an additional point. (b) Force - engineering strain curves for FE analyses of the tensile test with the hardening behaviour from (a). (c) Force - engineering strain curves for all experiments and the final FE analysis(0.25, 400).

Morin et al. [1] proposed a convenient method for determining the mesh dependent fracture parameter, which builds on work by Hogström et al. [44]. The method consists of extracting strain measurements from a tensile test utilising DIC analyses with varying characteristic element size l_e , and use these to set the boundary conditions of a single shell element with the same l_e in FEAs. The fracture parameter corresponding to l_e can then be calculated as

$$W_C = \int_0^{p_f} \sigma_I dp \quad (3.13)$$

where p_f is the plastic strain at fracture. In this study the strain behaviour was extracted by utilising virtual extensometer vectors in eCorr, as explained in Section 2.3. The vector position was exactly the same for all the DIC analyses, while the vector lengths were set to the desired l_e . The shell element, which is displayed with BCs in Figure 3.7b, was modelled in ABAQUS/Standard. The model consisted of a single S4R element with a thickness of 2 mm and 5 Simpson integration points across the thickness. The material behaviour was described by our constitutive model, with the material parameters in Table 3.1, excluding the fracture parameter. The shell elements were stretched to the fracture strains found in the corresponding DIC analysis. The principal stress and plastic strain was extracted from the FEAs and used to calculate the damage evolutions and resulting fracture parameters, as can be seen in Figure 3.7c and Figure 3.7d.

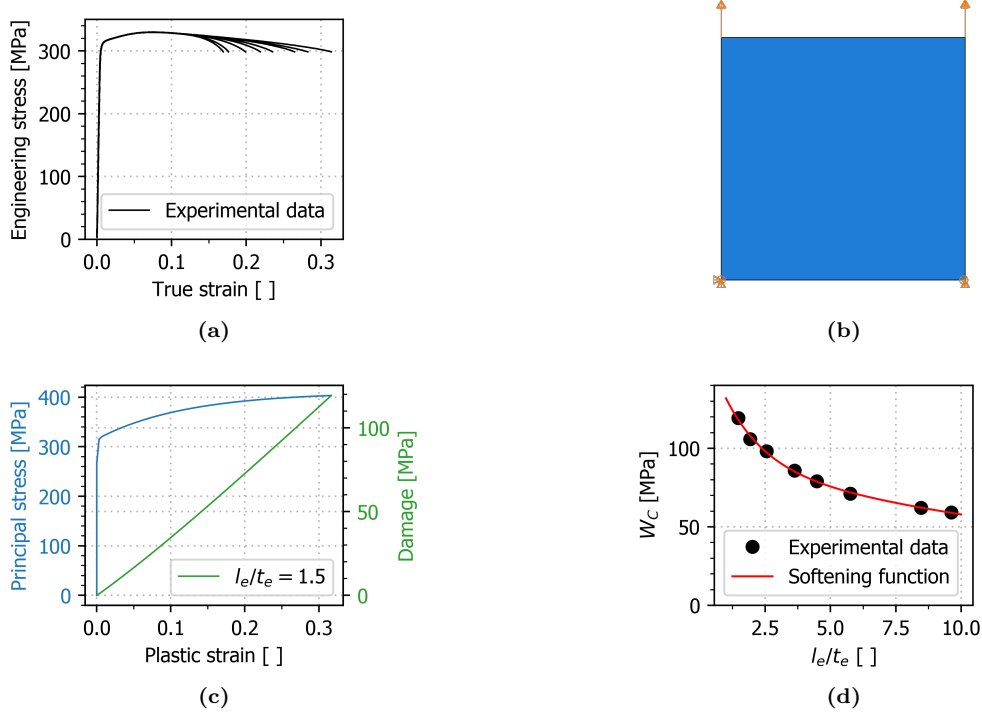


Figure 3.7: (a) True strain behaviour from DIC analyses with different characteristic element lengths, combined with force measurements from the Zwick/Roell Z030 test machine. (b) Snapshot of the single shell element used in the FEAs, with BCs. (c) The principal stress - plastic strain behaviour from the FEA with $l_e/t_e = 1.5$, as well as the damage evolution. (d) The exponential softening function describing the fracture parameter W_C for a range of l_e/t_e values.

Table 3.1: The material parameters for the plate, with $l_e/t_e = 1$.

	E [MPa]	ν []	σ_0 [MPa]	a []	θ_1 [MPa]	Q_1 [MPa]	θ_2 [MPa]	Q_2 [MPa]	W_C [MPa]
Plate	70000	0.3	291.8	8	794.0	95.0	16808.3	23.3	131.9

3.5.2 Stiffened Panel

Table 3.2: The material parameters corresponding to the material model suggested for the aluminium panel by Morin et al.[1].

	E [MPa]	ν []	σ_0 [MPa]	m []	θ_1 [MPa]	Q_1 [MPa]	θ_2 [MPa]	Q_2 [MPa]	W_C [MPa]
Base plate	66000	0.3	271.5	8	36591.2	17.8	1300.0	88.0	64.3
Stiffener	66000	0.3	238.7	8	63294.5	36.6	1440.0	90.0	64.2
HAZ	66000	0.3	150.0	8	3450.0	140.0			

Although anisotropy was evident, Morin et al. [1] adopted an isotropic elastic-plastic model, in order to enable industrial application. Their material model consisted of the Hershey-Hosford yield function, extended Voce

rule work-hardening and the Cockcroft-Latham failure criterion formulated as a damage evolution rule. The panel was divided into three material sections: the base plate, the stiffeners and the HAZ, each with separate hardening and fracture behaviour. The exact same modelling approach were used for the base plate and stiffener sections, while the modelling of the HAZ section differed slightly as it was modelled without a failure criterion and with a single term Voce rule. Except for the yield surface the same modelling approach will be applied in the numerical study of this thesis, of which the material parameters are shown in Table 3.2.

4 Preliminary Studies - Part II

This section will use the experimental setup presented in Section 2.5 to determine a test matrix. Numerical simulations will be used to study: (1) the effect of different driver lengths and nominal firing pressures and analyse the resulting loading, and (2) the structural responses based on the loading obtained in (1). This section starts with a description of the numerical simulations. Then, the dynamic response is evaluated, and, lastly, the experimental programme is presented.

4.1 Introduction

The complexity of the problem in this thesis, with regard to both the loading and the structural response for the stiffened plate, requires numerical methods for sufficient insight into the problem. To validate the performance of relevant computational methods, experimental validation is necessary. Experimental trials in a small-scale, controlled environment - such as in the SSFT - is necessary, because it represents the actual physics of the complex problem. Before the experimental work, an insight into the extreme non-uniform loading and the resulting structural responses will be investigated numerically as a preliminary study, with the objective of developing an experimental programme for the setup. Here, the intensity of the applied extreme pressure load will be determined, that gives distinctive structural responses for easy calibration and validation of the later numerical model.

There are several approaches readily available in the literature, although different load, that can be utilised to determine both the loading parameters and the description of the structural response. In [45], a brief overview of available approaches is presented. Within numerical methods, the Eulerian-Lagrangian method is commonly used, implying the fluid and the structure to be described separately. The Lagrangian description focuses only on the structure. The mesh node follows the associated material particle during motion ([46]). For larger distortions - like in fluid dynamics - Eulerian algorithms are used ([46]). The mesh is fixed, and the continuum moves relevant to the mesh. The Eulerian description predicts the fluid inflow around the structure. From here, the problem can be approached in two ways: A coupled Eulerian-Lagrangian approach, or an uncoupled Eulerian-Lagrangian approach. Regarding the latter, the pure Eulerian simulation with the obtained spatial and temporal distribution of the pressure on the rigid body is imposed into a pure Lagrangian simulation. In the coupled approach, the two domains (fluid and structural) are allowed to interact, whereas the uncoupled approach assumes the structure motion will not alter the pressure, and vice versa. Fluid structure interactions (FSI) is an active field of research. The influence the dynamic response have on the pressure distribution and vice versa has been illustrated by comparing the uncoupled and coupled approaches. Børvik et al. [47] and Casadei et al. [48] demonstrated that FSI effects could substantially influence both structural response and pressure distribution. They compared uncoupled with fully coupled FSI simulations when dealing with a container exposed to blast load as well as other industrial objects and cases.

The uncoupled approach will be used in the preliminary studies due to the increased complexity and computational cost of a fully coupled FSI simulation. First, a presentation of the Eulerian simulations with the new setup within the SSFT is executed, using the latest models developed by Aune et al. [49]. By doing so, the spatial pressure distribution and the temporal pressure distribution are obtained. Second, the pure Lagrangian simulation will be presented. Third, the results and the experimental programme will be determined.

4.2 Eulerian Simulations

The extreme pressure load for the uncoupled approach was obtained from numerical simulations in the finite element code EUROPLEXUS (EPX) [22]. EPX is a jointly developed code made by the French Commissariat l'Energie Atomique et aux Energies Alternatives (CEA) and the Joint Research Centre of the European Commission (JRC). Post-processing of the numerical simulations was carried out in Paraview [50] and EPX.

The numerical modelling of the shock wave loading for the uncoupled approach is divided into two steps. These steps can be seen in Figure 4.1. The first step is a preliminary mapping simulation, including a detailed representation of the diaphragm failure process. The importance of including the failure of the diaphragm was emphasised by Andreotti et al. [51]. It was shown that the failure process may affect the reflected overpressure on the test specimen downstream the firing section, due to the development of a multi-dimensional flow field. From a discrete 3D mesh in proximity to the driver section and the firing section, the fluid shock wave propagates downstream into a 1D mesh discretisation. The first step generates a mapping file of the developed shock wave close to the shock tube opening. The second step is a restart of the mapping file only including the fluid and excluding the diaphragm. By doing this, computational time is saved by excluding the rupture process of the diaphragm later. The second part focuses on modelling the fluid physics from the shock tube opening and into the dump tank resulting in a spatial and temporal distribution of the loading. The pressure-time history is then extracted on the rigid wall, in Figure 4.1b, and exported into purely Lagrangian (structural) simulations in ABAQUS/Explicit.

4.2.1 Computational Fluid Dynamics

The CFD method makes use of mathematical equations that describe the basic laws of physics. The governing equations in the fluid sub-domain express the conservation of mass, momentum and energy. It is preferred to express the conservation laws of the fluid sub-domain in a spatial (Eulerian) framework, due to the assumption that the fluid experiences inviscid compressible flow which will occupy the entire control volume. This section was based on description from [45].

The conservation laws in Equations (4.1), (4.2), (4.3), are the Euler Equations [52] which is a reduced form of the Navier-Stokes equations where heat conduction, shear stresses and turbulence are neglected. Euler Equations are expressed on differential form:

$$\frac{\partial \rho}{\partial t} + \nabla \cdot (\rho \vec{v}) = 0 \quad (4.1)$$

$$\frac{\partial \rho \vec{v}}{\partial t} + \nabla \cdot (\rho \vec{v} \otimes \vec{v}) + \nabla p = 0 \quad (4.2)$$

$$\frac{\partial E}{\partial t} + \nabla \cdot (\vec{v}(E + p)) = 0 \quad (4.3)$$

where Equation (4.1) represents the conservation of mass, Equation (4.2) is the conservation of momentum, and Equation (4.3) represents the conservation of energy. ρ is the density, and $v = v_i \mathbf{e}_i = [v_1 v_2 v_3]^T$ is the velocity vector with components v_1 , v_2 and v_3 along each of the basis vectors in a Cartesian coordinate system \mathbf{e}_i . The total energy per unit volume is given as $E = \rho(e + \frac{1}{2} \mathbf{v}^t \mathbf{v})$, where e is the specific internal energy per unit mass, $\frac{1}{2} \mathbf{v}^t \mathbf{v}$ is the kinetic energy per unit mass, p is the pressure, ∇ is the spatial gradient, and \otimes is the tensor product.

The conservation law generally contains more unknowns than equations. In order to obtain a unique solution to the conservation laws, a thermodynamic equation of state (EOS) - i.e. a constitutive equation that relates the pressure to the conserved variables - is introduced as the ideal gas law for air. It is given on the form applied for this thesis as

$$p = \rho(\gamma - 1)e \quad (4.4)$$

where the ratio of specific heat, $\gamma = C_p/C_v$, is given by C_p and C_v , which is the specific heat for constant pressure and constant volume, respectively. e is the specific internal energy per unit mass. The specific internal energy is further given as $e = RT/(\gamma - 1)$ for an ideal gas behaviour, where T is the temperature and R is the specific gas constant which is unique for each gas. The ideal gas law is not valid under certain conditions, such as high pressures and low temperatures. The presented EOS is regarded as sufficient for problems under consideration in this thesis.

4.2.2 Numerical Model

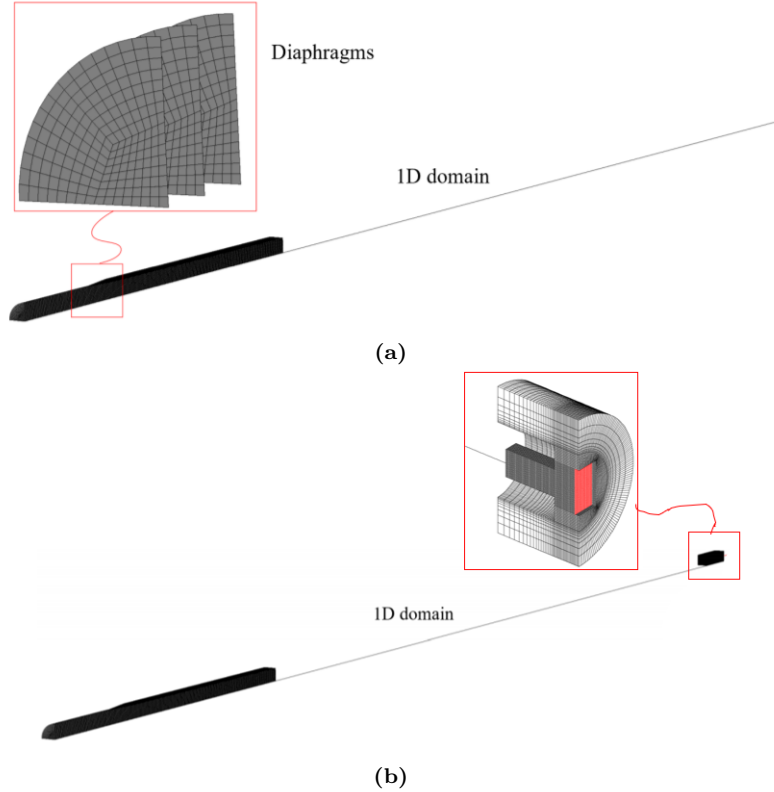


Figure 4.1: Numerical model of (a) the preliminary mapping simulation and (b) the fluid sub-domain close to the rigid plate.

The set up for the numerical model developed in EXP can be seen in Figure 4.1. Here, the fluid sub-domain was discretised using the finite volumes - i.e. 1D finite volumes (TUVF) - and by 3D finite volumes (CUVF). Cell-centred finite volumes (CCFV) was used with approximate Harten-Lax-Leer-Contact Riemann solver for calculations of the numerical fluxes between neighbouring CCFVs. The Courant-Friedrichs-Lewy (CFL) coefficient was set to 0.4 to ensure stability by ensuring that flux only occurred between neighbouring cells. For both the 1D and 3D mesh, an initial mesh size of 10 mm was set based on mesh sensitivity studies carried out in [24], [53]. The cell size in the dump tank was prescribed with a biased size of 80 mm towards the internal walls. By modelling the driven section with TUVFs, EPX can handle the heat exchange and friction with the walls by specifying average roughness (0.4 micrometers) in the PARO directive in EPX [22]. Furthermore, the computational time will be reduced. In Figure 4.1, one can first see the circular 3D

mesh in the driver section and the firing section, before it follows the geometry of the shock tube into a square cross section in the driven section, followed by the 1D discretisation until 625 mm in front of the rigid pressure wall. The symmetry of the problem is utilised, and one quarter is modelled in the preliminary mapping simulation (Figure 4.1a). However, due to the shock wave disturbance mounted at the end of the shock tube, only one symmetry plane exists for the second simulation (Figure 4.1b). Because of this, half symmetry is used at the right end of the model.

Only the diaphragms were modelled with Lagrangian discretisation in EPX. The diaphragms have a base mesh of 10 mm with Reissner-Mindlin shell elements (Q4GS), modelling exclusively the exposed area. The nodes located around the perimeter were fixed against translations in all directions as a simplified boundary condition. Fracture was modelled through the use of element erosion when all integration points within an element have obtained maximum principle strain. Element erosion is used together with adaptive mesh refinement (AMR). AMR is a modelling technique that correlates any monitored parameter with a refinement of the mesh, splitting a base mesh element into smaller elements (Figure 4.2) as a threshold condition is obtained [54]. In this numerical model, the AMR was driven by user-defined values of plastic strain. The first mesh refinement was performed with a plastic strain of 0.01, and the last refinement with a plastic strain greater than 0.4, resulting in a minimum element size of 2.5 mm. This ensured fracture without excessive loss of mass.

The failure process of the diaphragms is mainly a FSI problem. In order to model the failure of a structure with an extreme loading case, the embedded FSI algorithm (FLSW) [22] is chosen. This, along with a FSI-driven AMR, was used for the coupling of the fluid and the diaphragm interface. For sufficiently refinement of the mesh on the fluid diaphragm interface, the FSI-driven AMR was used in the fluid sub-domain.

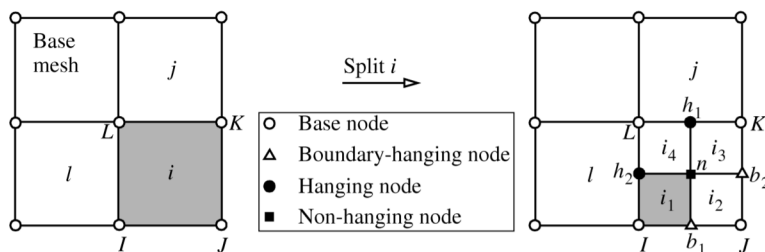


Figure 4.2: The figure is taken from [54]. Illustrating one level of adaptive mesh refinement. The hanging nodes are constrained by neighbouring nodes and link conditions [54], and the boundary hanging nodes are determined by the boundary conditions they are placed on.

The CFD code computes the spatial and temporal fluid pressure along the rigid fluid boundary (the red wall in Figure 4.1b). The pressure-time history is then obtained from a number of points on the surface of the wall, as illustrated in Figure 4.3b. The exposed area of the wall in the numerical model (250 mm x 500 mm due to symmetry) is partitioned into 50 squared subareas of 50 mm x 50 mm, where the pressure-time is averaged within the subareas. The mapped data is then used as input of the Computer Structural Dynamic (CSD) code, ABAQUS/Explicit, with a pure Lagrangian simulation to determine the structural response of the deforming structure.

4.3 Lagrangian Simulations

The second half of the numerical modelling of the uncoupled approach is the Lagrangian model. This section will describe the numerical models of the deformable plate and panel, used to determine the experimental programme. They are performed in the explicit FE software, ABAQUS/Explicit [23].

The obtained mapped pressure-history inflow around the rigid fluid boundary in the CFD simulations is exported as 50 smaller subareas over the exposed pressure area - where symmetry is utilised - as seen in

Figure 4.3b. Pressure and time for the 50 subareas are then post-processed through a python script. The script controls that the time monotonically increases, and it writes the pressure-time data to a text file with readable syntax for ABAQUS/Explicit.

In ABAQUS/Explicit, the exposed pressure area is partitioned into 100 surfaces (50 x 50 mm), to accommodate the CFD data. To manually create 50 amplitudes and pressure loads before manually assigning the zones into the correct subareas in the numerical models is cumbersome. Therefore, a python script that creates pressure loads with amplitude histories and assigns them to the appropriate surface sets was created.

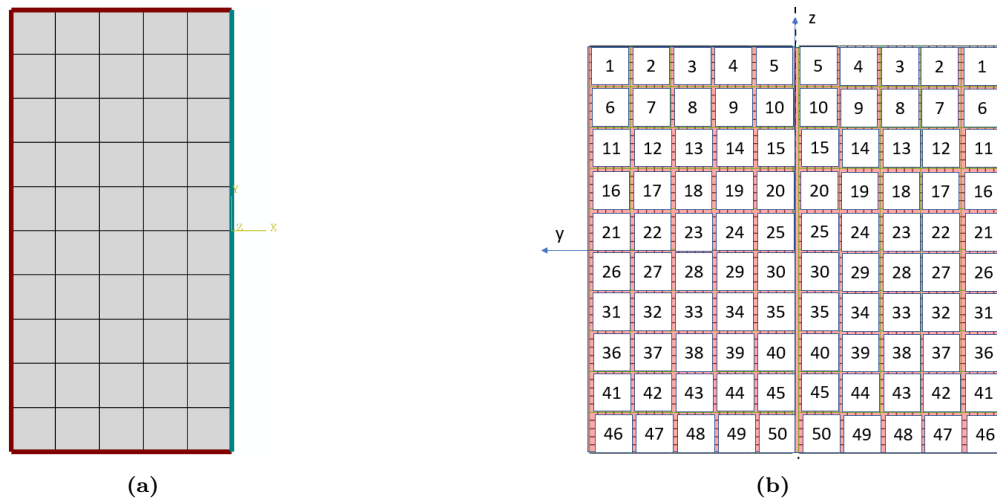


Figure 4.3: (a) Illustrate the simplified numerical plate model and shows the 50 partitioned subareas where the loads are assigned. The red edge is the clamped boundary and the blue edge is the symmetry line. (b) Illustrating the 50 subareas (50 x 50 mm), where average pressure-time history from EPX was extracted. The subareas correlates with the exposed pressure area (500 x 500 mm) for the test specimen. The z-axis is a symmetry axis.

4.3.1 Numerical Model: Plate

A simplified numerical model of the plate was established in ABAQUS/Explicit. Only the exposed pressure area of the plate was modelled. The plate would be bolted and clamped in the experiments, thus, the simplified model had all edges locked for all translations and rotations expect for the symmetry edge. The symmetry of both the loading and the structure permitted the use of symmetry in the model. Hence, half the plate was modelled. A representation of the plate model with the partitioned subareas for assigning loads is displayed in Figure 4.3a.

Furthermore, the plate is represented using Lagrangian discretisation. 4-noded Mindlin-Reissner shell elements with reduced integration (S4R) and hourglass control, 6 degrees of freedom per node and 5 Gauss integration points through the thickness (20 Gauss integration points in total) were used to discretise the plate. A mesh sensitivity study was conducted, and it was discovered that the global deformation converged at an element size of 10 mm. An element size of 5 mm was deemed adequate to capture tearing and failure, with regard to limiting mass loss and computational time at this initial stage. Material fracture is modelled through element erosion. Fracture is initiated when the damage criteria described in Section 3.4 is satisfied at an integration point within an element. The stress tensor is then set to zero. Element erosion occurs when all integration points reach the critical value. The fracture parameter, W_C , has been presented and calibrated for a number of element sizes in Section 3.4. Standard material modelling techniques were applied with von Mises yield surface criterion, with its material and physical constants found in Table 3.1. The material behaviour of the plate was governed by the constitutive model described in Section 3.3.

4.3.2 Numerical Model: Stiffened Panel

The panel is discretised with S4R shell elements - just like the plate. As previously discussed in Section 3.5.1, modelling shell elements with characteristic element length close to or below the shell thickness leads to excessive thinning and potential numerical problems. Hence, the characteristic element lengths used in shell models are typically equal to or greater than the thickest part of the given section ($l_e/t_e \geq 1$). As the stiffeners and base plate share nodes, the panel is meshed with a global element size. Therefore, the critical element length is 4 mm (Figure 2.2a). Mesh size studies were conducted, and as the global deformation did not converge - even with an element length of 8 mm ($l_e/t_e = 2$) - using the critical element length was deemed a necessity. The most significant thickness scaling factor with the critical element length is 0.79. As it was ensured in the preliminary studies that the claws had no physical interaction with the test specimen for the simulated duration, the supports were modelled as simple aluminium cuboids. The bottoms of the cuboids are fixed in all translations and rotations, to represent the bolted nature of the actual aluminium supports. The supports are discretised using eight-node solid brick elements, with reduced integration (C3D8R), of aluminium with linear-elastic behaviour. The supports are meshed with a characteristic element length of 10 mm, and the same material parameters as the panel are used to model the linear aluminium.

In order to prevent the geometries from exhibiting non-physical penetrations, constraint equations are imposed. A tracking algorithm is also needed, and it handles the geometries that are interacting. This gives a contact formulation. ABAQUS/Explicit only provides two algorithms to model contact: general contact or contact pairs. For constraint criteria in explicit analysis, both the Penalty method and the Lagrangian method can be used, however only the Penalty method is used in ABAQUS/Explicit. In addition a constitutive model governing the relationships between the various surfaces in the numerical model - such as frictional behaviour - is introduced. Friction was introduced in the mechanical surface interaction model through the Simple Coulomb friction model [23]. For the stiffened panel model general contact was utilised.

The panel rests freely on the supports - merely held in place by friction. The frictional coefficient sensitivity was investigated, and a great variation was discovered. Due to limited experimental data the frictional coefficient had to be found from literature. For conditions similar to the component tests conducted in this study (dry, static, rough surfaces), scientific literature lists the friction coefficients for aluminium-aluminium between 0.1-0.7 [55]. Therefore, a friction coefficient of 0.15 was used as a conservative estimate.

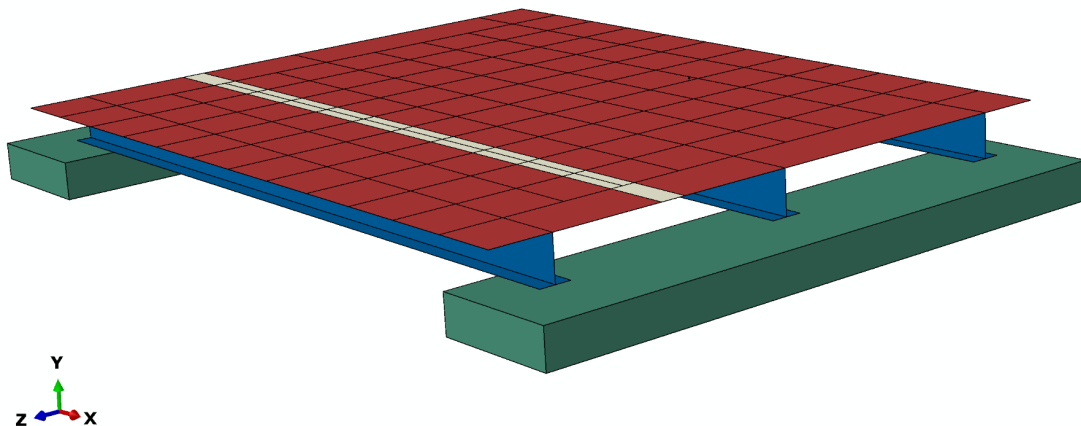


Figure 4.4: Numerical model of the stiffened panel with supports (green). The stiffened panel consists of the base plate (red), three stiffeners (blue) and a HAZ (white). Furthermore, the figure shows the 100 partitioned subareas where the loads are assigned. The centerline of the HAZ coincides with the borderline between the third and fourth columns of subareas.

The panel is modelled with three different material sections. The material modelling is described in Section 3.5.2. The three sections are the base plate, the stiffeners and the HAZ. Previous work by Morin et al. [1] was considered when modelling the HAZ as a 20 mm wide homogenised section along the weld. The hardening behaviour of the HAZ differs significantly from the behaviour of the stiffener and base plate sections, as can be seen in Figure 3.3, making the HAZ a weaker zone. In Figure 4.4, the complete model is illustrated.

4.4 Results from CFD

In this section, some of the results from the Eulerian simulations will be presented and explored. Furthermore, the effects different driver lengths and nominal firing pressures have on the resulting pressure load will be presented.

4.4.1 Nominal Firing Pressure

In Figure 4.5, the driver pressure with the corresponding peak pressure is shown. It is observed that with an increased nominal firing pressure, the peak overpressure reaches a saturation pressure. This was also observed for the rigid plate in the closed shock tube configuration by Aune [24].

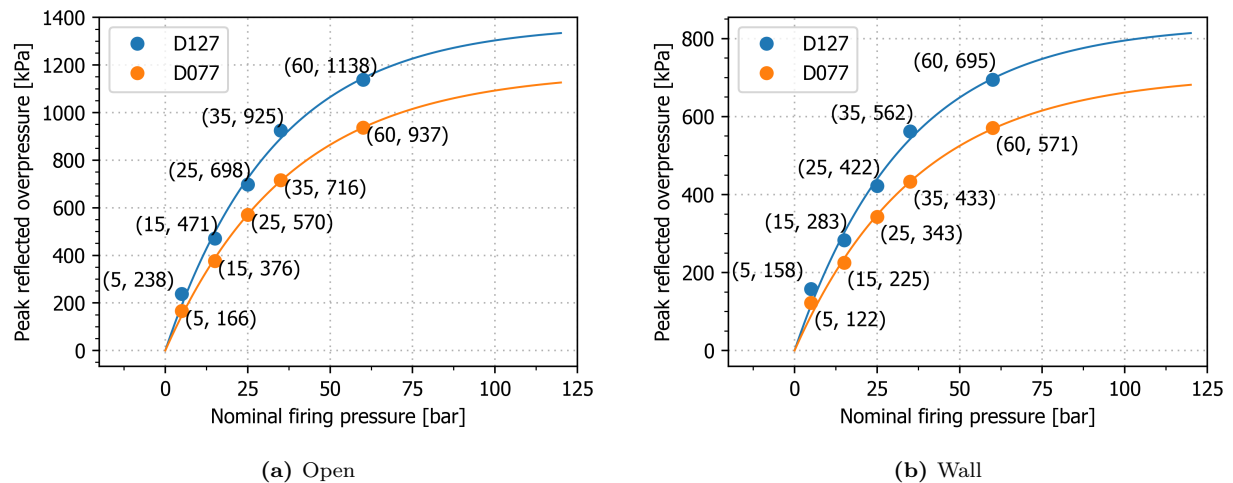


Figure 4.5: Firing pressures in the driver section, related to peak overpressure on the rigid plate, and fitted with an exponential function.

It should be noted that Aune [24] showed that the numerical simulations and the experimental results corresponded for lower nominal firing pressures. It was discovered that as the nominal firing pressure increases, the peak reflected overpressure of the CFD simulations tends to deviate more than the experimental results. The reason for this was explained to be the increased obstruction of flow during the diaphragm opening process, due to increased diaphragm thickness to comprehend the increased pressure. This will slow down the opening process and prevent satisfactory folding-back of the diaphragm. The result is a loss of directional energy downstream the shock tube. Although the physics of the open and the closed configuration of the shock tube are different, it still provides a certain correspondence that could give some indications. As an intent to address this problem, the diaphragm rupture process was included in the 3D numerical model of the firing process, as mentioned in Section 4.2.2.

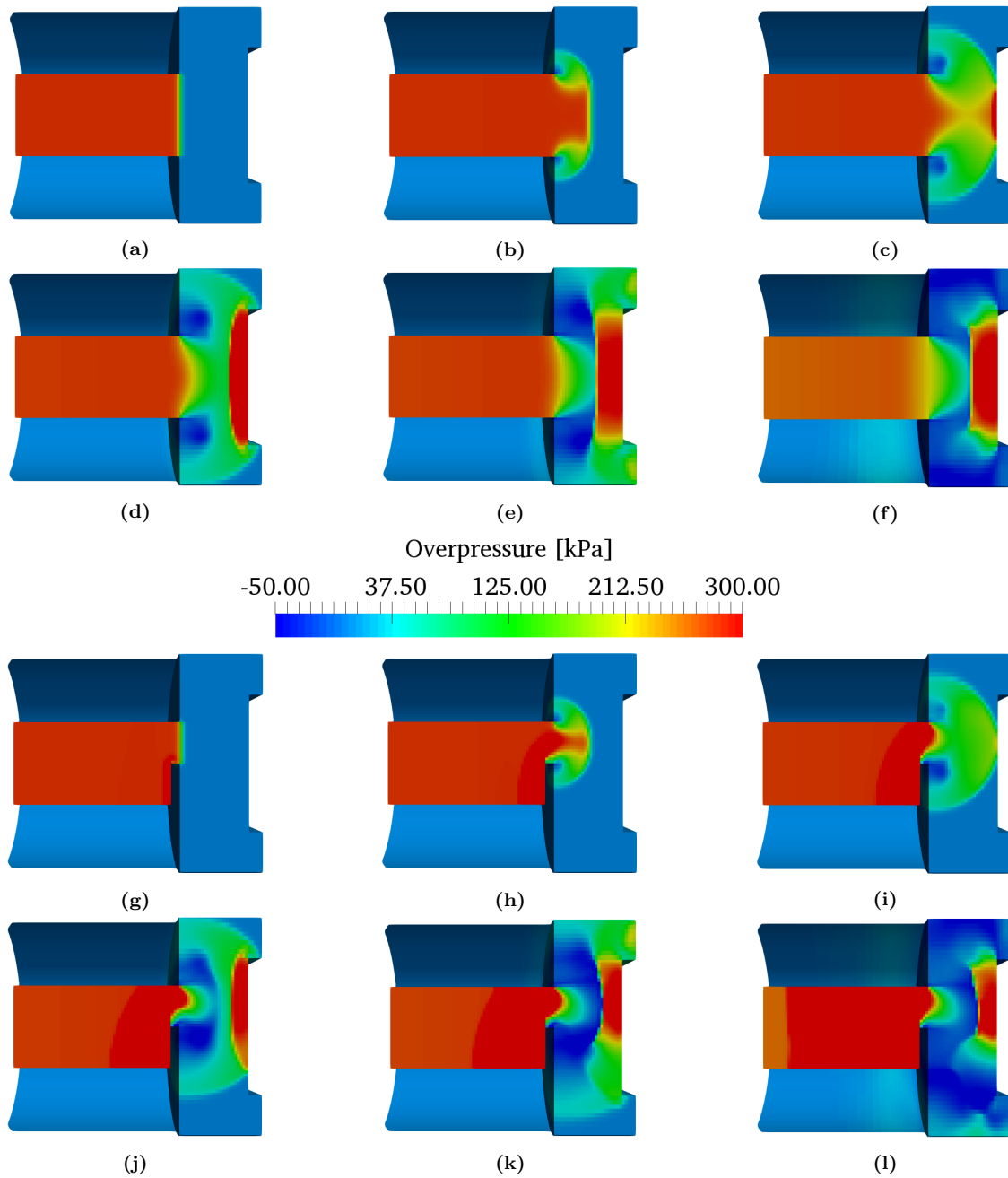
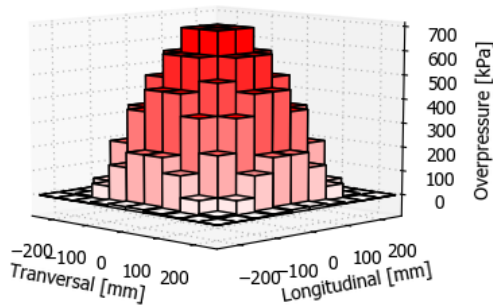


Figure 4.6: Pressure distributions from the CFD simulations with 25 bar nominal firing pressure are displayed for the open ((a)-(f)) and wall ((g)-(l)) configurations. The images capture the last 375 mm of the driven section as well as the first 250 mm of the dump tank, complete with the rigid pressure wall. The pressure distributions are more or less representative for all firing pressures.

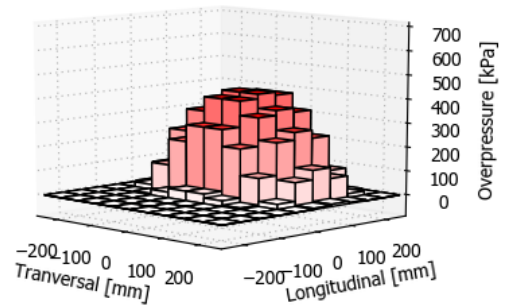
Figure 4.5 provides vital information about peak pressure for the experiments of the new setup. Moreover, it indicates the maximum load levels achievable in the SSTF. Due to the saturation of the peak pressure within one driver length, an increase of the driver firing pressure past 60 bars gives a marginal increase in the peak pressure. However, increasing the driver length results in larger peak pressures with the same firing

pressure. As the deformable test structures have different loading capacities, and it is highly inefficient to alter the driver length between tests, a driver length that yielded a satisfactory wide loading spectre was chosen. A driver length of 127 cm was determined to yield a sufficient loading spectre. Longer drivers could have been used, but increasing the driver length increases the time needed to build up the pressure. Hence it is inefficient to use a longer driver than necessary. Limiting the nominal firing pressure also gives better results for the CFD simulations, as the loss in the directional flow energy is kept to a minimum.

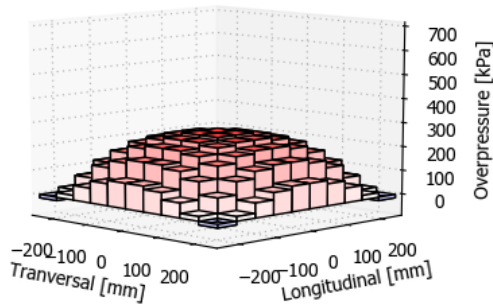
4.4.2 Resulting Pressure Distribution



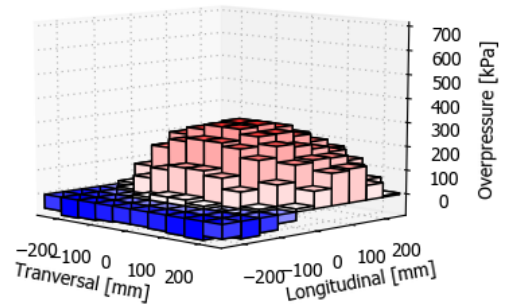
(a) CFD_O.25 - Maximum



(b) CFD_W.25 - Maximum



(c) CFD_O.25 - Minimum



(d) CFD_W.25 - Minimum

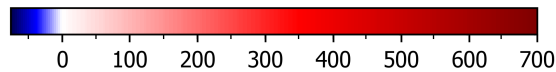


Figure 4.7: A visualisation of the maxima and the minima of the simulations, conducted with a driver pressure of 25 bar for the two driven outlet configurations. The shapes of the distributions are representative for all simulations.

Pressure distributions from the CFD simulations with 25 bar nominal firing pressure are displayed in Figure 4.6 for both outlet configurations. The images capture the last 375 mm of the driven section as well as the first 250 mm of the dump tank, complete with the rigid pressure wall. The shock front forms the sphere shape

characteristic of air blasts as it exits the driven section for both configurations. For the open configuration, the shock front first contacts the centre of the massive plate. Then, it gradually covers the whole plate with an almost uniform pressure. It is almost uniform in the sense that the pressure magnitude stays slightly elevated at the centre and that lower pressure values are seen along the edges due to complex fluid flow effects. For the wall configuration a pressure wave is observed travelling back upstream the driven section, in large part accounting for the loss in peak pressure. The sphere travelling towards the rigid wall first makes contact with the rigid pressure wall about 120 mm above the centre. The subsequent pressure distributions around the wall are very complex, resulting in an underpressure establishing on the bottom fifth of the rigid pressure wall(Figure 4.6l). The wall configuration was added to increase the complexity of the pressure load on the test specimens, and the simulations certainly indicate that the addition of the wall greatly alters the pressure load.

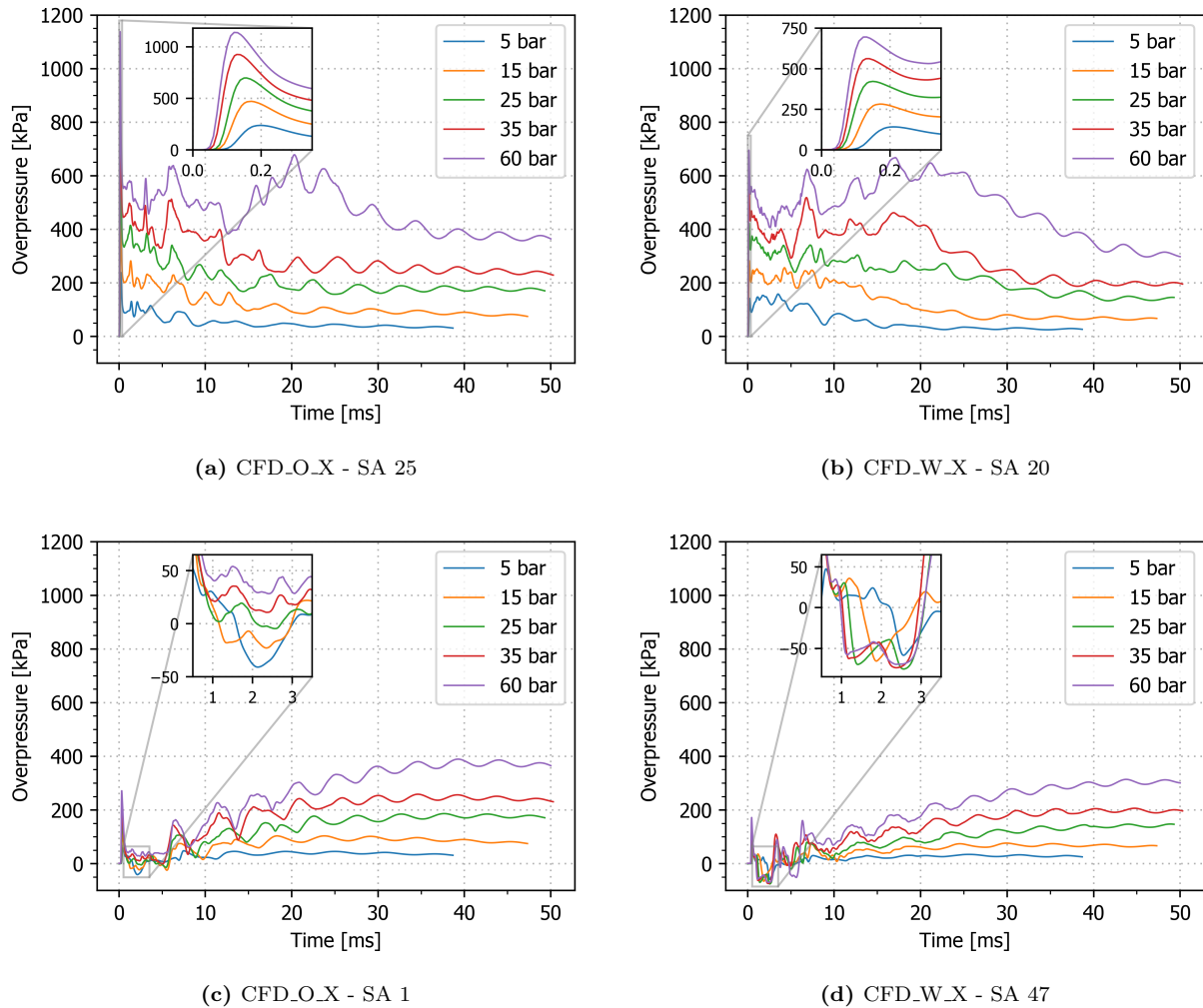


Figure 4.8: Overpressure-time histories of the subareas containing maxima ((a)-(b)) and minima ((c)-(d)) for all nominal firing pressures and both the open and wall configurations.

4.4.3 Resulting Load

The non-uniform spatial distribution of the overpressure loads at the time of maxima and minima is displayed in Figure 4.7. The figure emphasises the subarea partitioning by showing the pressure level measured at the middle of each subarea. The subareas were used both in the CFD simulations for data extraction, and for assigning the load in ABAQUS/Explicit. Therefore, this visualisation was deemed more appropriate than a smooth integrated surface. The plots are symmetric about the longitudinal line through the 0 mm transversal point. The driven outlet configuration greatly affects the overpressure distribution.

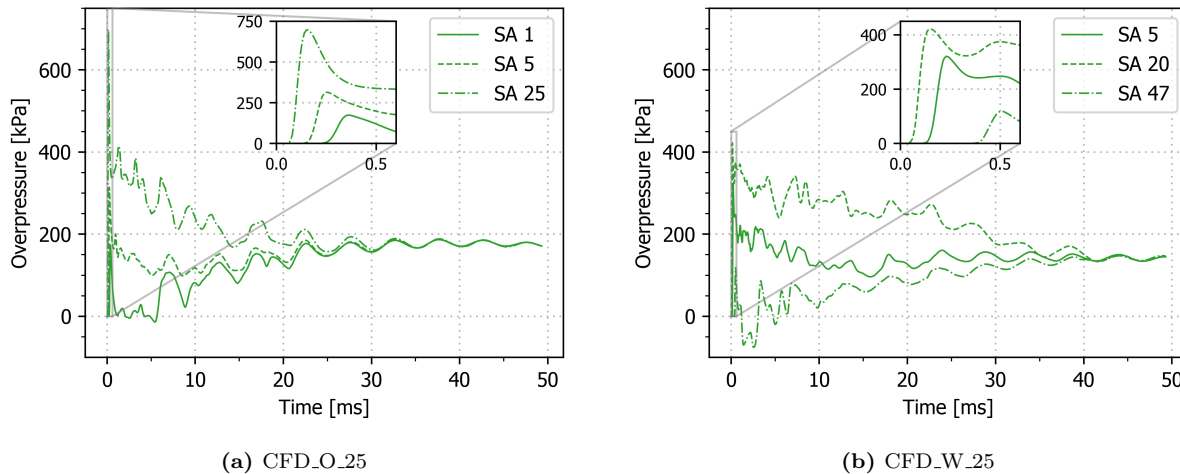


Figure 4.9: Overpressure-time histories of the subareas containing the maxima and minima, in addition to a subarea with median pressure levels from the two simulations conducted with a nominal firing pressure of 25 bar. The shape of the curves are more or less representative for all firing pressures, as can be seen from the maxima and minima curves in Figure 4.8.

The overpressure-time histories of the subareas subjected to the maximum and minimum pressures are shown for all nominal firing pressures and both driven outlet configurations in Figure 4.8, showing some interesting trends. As can be seen, the behaviour of the maxima curves (a, b) of both driven outlet configurations are similar. As is discussed above, the peak pressure on the rigid pressure wall increase with increasing firing pressure. The peak pressure saturates however, leading to a decreasing percentage of the total energy being contained in the shock front. After the pressure drops from the peak value, the excess energy at elevated firing pressures translates to sustained periods of medium pressure, before the pressure decreases to equilibrium. There is a pressure drop of about 50% and 25% for the simulations conducted with the open and wall configurations, respectively. The delayed transfer of energy is especially apparent when looking at the simulations with a nominal firing pressure of 60 bar, as the second highest pressure values are measured at around 20 ms. The equilibrium level- which is easily detected from the convergence of the subarea pressure levels in Figure 4.9 - increases with firing pressure. This is because the excess air is trapped inside the tank in the simulations, while it leaks out in reality. However - as only the first 250 mm of the dump tank was included in the simulations - the equilibrium level is likely exaggerated considerably. The minima of the simulations with open configuration increase with firing pressure. This is not typically found in literature [56], which indicates that the negative values are due to complex flow effects and not over-expansion. The magnitudes of the minima of the simulations with the wall configuration are all quite similar, although the negative impulse of the simulations with firing pressures of 5 and 15 bar are smaller than the rest. Apart from these variances, the shape of the overpressure-time curves for each subarea are representative for all firing pressures with the same configuration, and the maxima and minima curves neatly enclose the curves of the

remaining subareas. Figure 4.9, a and b, are therefore good representations of the general overpressure-time behaviours.

4.5 Results from CSD

In this section, some of the results from the Lagrangian simulations will be presented and explored. The results will be presented in three blocks. The first block characterises the loading regime, focusing on both structures. The second and third block deal with the plate and the panel, respectively, focusing on the exploration of the structural responses.

4.5.1 Loading Regime

Modal analyses of both the plate and the stiffened panel were conducted in ABAQUS/Explicit, in order to obtain the response time. It is common within structural dynamics to relate the natural period of a structure to the loading duration. In the book by Bakers et al. [57], three loading regimes based on an impulsive blast load duration on a structure were defined: impulsive, quasi-static and dynamic. The latter is a transition region between the two former.

The quasi-static regime is defined as, $t_d/T_n > 6.4$, while the impulsive regime is defined as, $t_d/T_n < 0.064$. t_d and T_n is the duration of the pressure pulse and the period of the fundamental natural frequency of the structure, respectively. During the impulsive regime, the duration of the applied load pulse is small relative to the response time of the structure. Furthermore, the deformation is strictly dependent on the impulse of the load. In the quasi-static regime, the response strictly depends on the peak load and the stiffness of the structure, not the load history. In the dynamic regime on the other hand, both the loading profile and history significantly influence the response, making it far more complex.

Modal analyses using the Lanczos eigensolver [23] in ABAQUS/Explicit was performed on the structural models described in Section 4.3. While the plate model could be analysed unaltered, minor changes had to be made to the stiffened panel model. The support blocks were removed and the panel was fixed for all translations where the support blocks were previously located. The fundamental natural frequencies were found to be $\omega_n = 68.55$ Hz for the plate and $\omega_n = 274$ Hz for the panel. To validate the frequencies, formulas from [58] were applied. The formulas gave fundamental natural frequencies of $\omega_n = 69.6$ Hz for the plate. Thus, the plate has a natural period of vibration of 14.6 ms, and the stiffened panel has a natural period of vibration of 3.6 ms.

Table 4.1: Ratio t_d/T_n is listed for all nominal firing pressures and both driven outlet configurations.

Nominal firing pressure [bar]	t_d [ms]		t_d/T_n []			
	Open	Wall	Plate		Panel	
			Open	Wall	Open	Wall
15	20	30	1.4	2.1	5.5	8.2
25	30	42	2.1	2.9	8.2	11.5
35	35	45	2.4	3.1	9.6	12.3
60	40	50	2.7	3.4	11.1	13.7

Defining the duration of the loading (t_d) of blast events is usually done by setting it equal to the duration of the positive phase of the pressure pulse. However, the spatial and temporal distributions of extreme pressure loads are different. Therefore the duration of the load was set to the time required to reach the equilibrium pressure for the subarea with the peak pressure. For the open and wall configurations in Figure 4.9, the time was set to 30 ms and 42 ms, respectively. The duration for all nominal firing pressures is presented in Table 4.1.

In Table 4.1, the ratio t_d/T_n is listed for both the plate and the stiffened panel for different nominal firing pressures and both driven outlet configurations. As the plate is between the two regimes (impulsive and quasi-static), the loading can be classified as dynamic. This indicates that the load profile significantly influences the response. The stiffened panel can be characterised to be within the quasi-static loading regime based on the ratios of Table 4.1. This implies that the load profile has a minimal effect on the structural response.

4.5.2 Plate

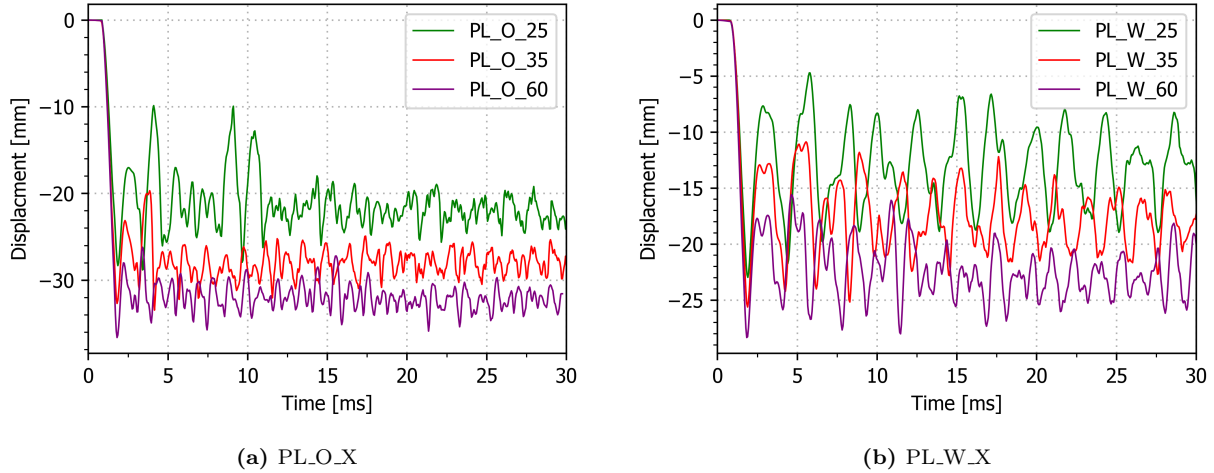


Figure 4.10: Midpoint deflection for a driver length of 127 cm. (a) is the open configuration and (b) the wall configuration.

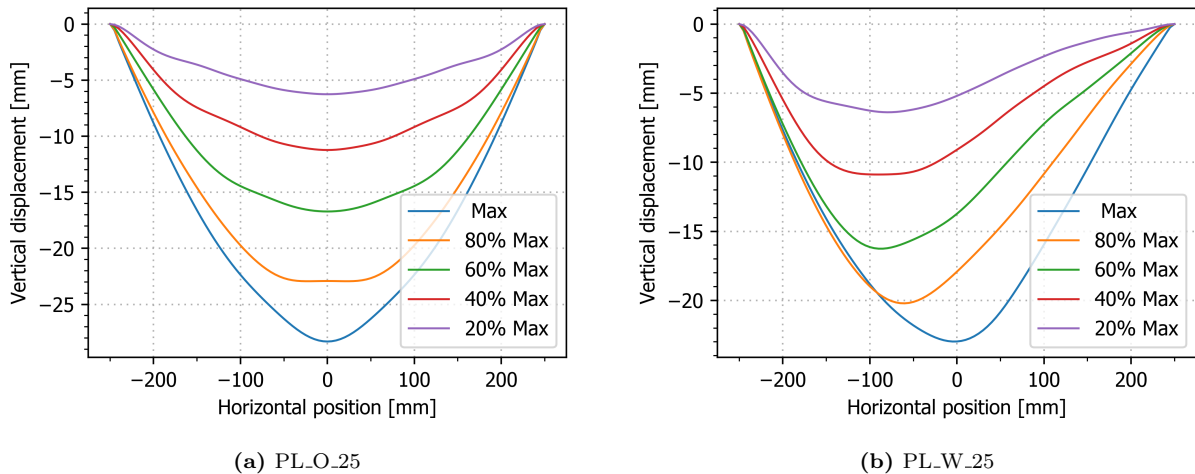


Figure 4.11: Deformation profiles for the (a) open and (b) wall configurations, with a nominal firing pressure of 25 bar. Due to poor sampling frequency, the given maximum deformation friction is not precise.

The midpoint deflection history of the plate is presented in Figure 4.10. Results are presented for nominal firing pressures of 25, 35 and 60 bar, with a 127 cm driver. It is evident that the increasing nominal firing pressure results in a increased inelastic deformation. After the rapid increase in deflection, the plate oscillates at its new equilibrium position. Only Mode I failure will be obtained with the available load magnitude. It was not possible to obtain fracture along the supports, thus, only inelastic deformation will be evaluated.

In Figure 4.11, representative deformation profiles of the plate are presented for the wall and open configurations. The wall configuration of the driven outlet is observed to induce an asymmetrical structural response. Travelling plastic hinge is observed travel towards the midpoint as the deflection progresses.

4.5.3 Stiffened Panel

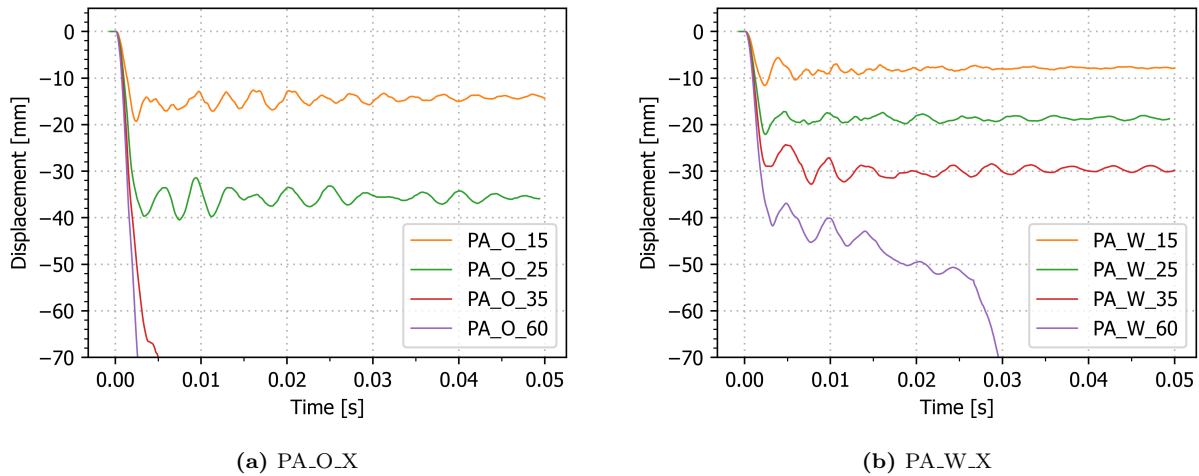


Figure 4.12: Deflection of the flange midpoint of the middle stiffener for the (a) open and (b) wall driven outlet configurations for different nominal firing pressures (127 cm driver).

The panel model was subjected to the pressure loads generated in EPX, and the resulting deflection history of the middle flange midpoint is presented in Figure 4.12. The presented results are for nominal firing pressures of 15, 25, 35 and 60 bar, with a 127 cm driver. Just like the plate, an increased nominal firing pressure results in an increased inelastic deformation for the panel. However, there is a major difference in that some of the deflection histories tends to infinity. This is due to the unfastened boundary conditions of the panel, which enable the panel to be pushed through the gap between the supports. The structural failure is initiated by the fracture of one of the stiffeners, which drastically reduces the panel's load-bearing capacity. This further increases the deformation of the base plate, which leads to the subsequent failure of the two remaining stiffeners. Without the added stiffening, the base plate folds, and the panel slips through the gap. The fracture sequences are shown in Figure 4.15. Whether the middle stiffener or the stiffener furthest from the weld (the right stiffener) fractures first depends on the shape and magnitude of the load. However, the stiffener closest to the weld (the left stiffener) always fractured after the right stiffener in the simulations. This highlights one of the effects of the HAZ. The weaker zone leads to larger deflections on the side of the HAZ, clearly visualised by the deformed panels with contour plots in Figure 4.14. This in turn forces more of the load to be absorbed by the opposite side. Because of that, the right stiffener always fractures before the left stiffener. After the panel reaches maximal deflection, elastic oscillations around its new equilibrium position commence, though with lower frequency and amplitude than the plate. The delayed transfer of energy discussed in Section 4.4.3 is made apparent by the deflection history in the PA_W_60 simulation in Figure 4.12b. When ignoring the oscillations, its maximal deflection increases almost linearly from the

initial maximum, resulting in a structural failure at 30 ms. This response is atypical when working with blast loading. PA_O_25 and PA_W_35 also reach maximal deflection after the initial maximum, but the effect is more subtle for these simulations.

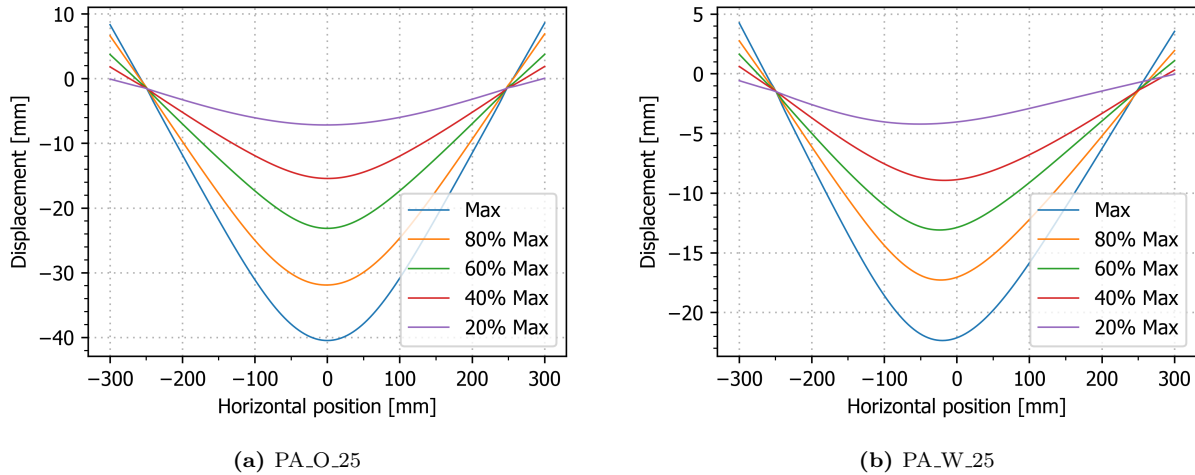


Figure 4.13: Deformation profiles of the centreline of the middle flange for the (a) open and (b) wall configuration for a nominal firing pressure of 25 bar.

In Figure 4.13, the deformation profiles of the centre-line of the middle flange are shown in increments of 20% of maximum deflection. The behaviour is quite similar to the behaviour of the plate, which is displayed in Figure 4.11. The maximal deflection point stays centred in the open configuration simulation, while the maximum point drifts in the wall configuration simulation - though to a lesser extent than for the plate. The reduced drift of the maximum and the added smoothness of the deformation profiles are due to the stiffeners restricting the movement of the base plate.

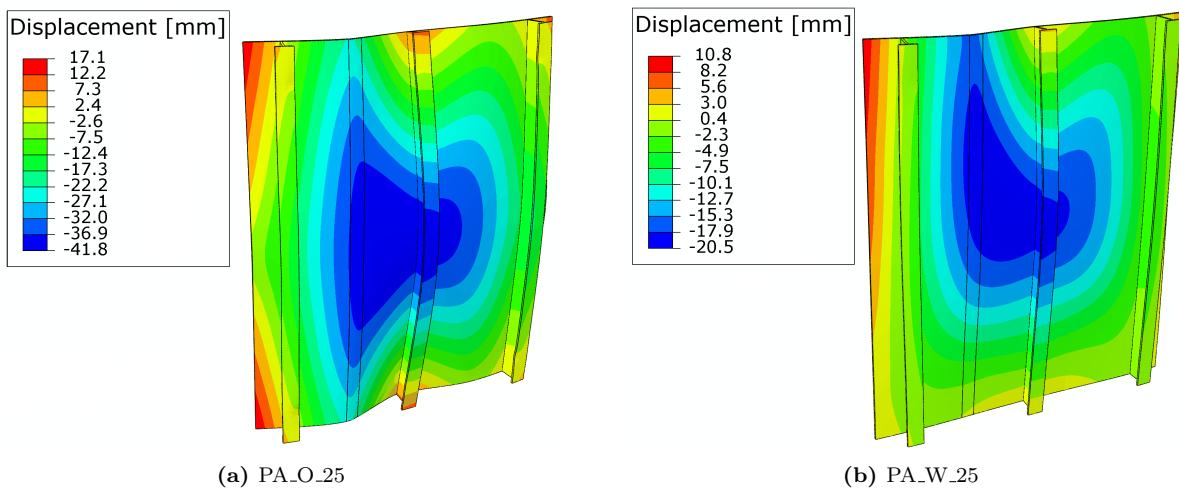


Figure 4.14: Deformed panel models at maximal deflection, with contour plots displaying the relative displacements. The panels were subjected to the CFD load corresponding to their respective outlet configuration with a nominal firing pressure of 25 bar.

Due to laboratory time restrictions, only essential responses were chosen. Therefore, fracture was not prioritised. However, the predicted structural response of the panel was quite consistent for each configuration - except for magnitude - in the load range below fracture. Thus, it was determined to look at one load resulting in a response close to - but safely below - fracture, and one load resulting in minor plastic deformations. Correctly predicting the structural responses in the entire plastic range up to fracture would validate both the CFD and CSD models, hence providing a framework for modelling plated structures subjected to extreme pressure loads. Additional simulations to the ones in Figure 4.12 were conducted - even though the chosen friction coefficient in the panel model was conservative - to ensure the chosen nominal firing pressures would not induce fracture.

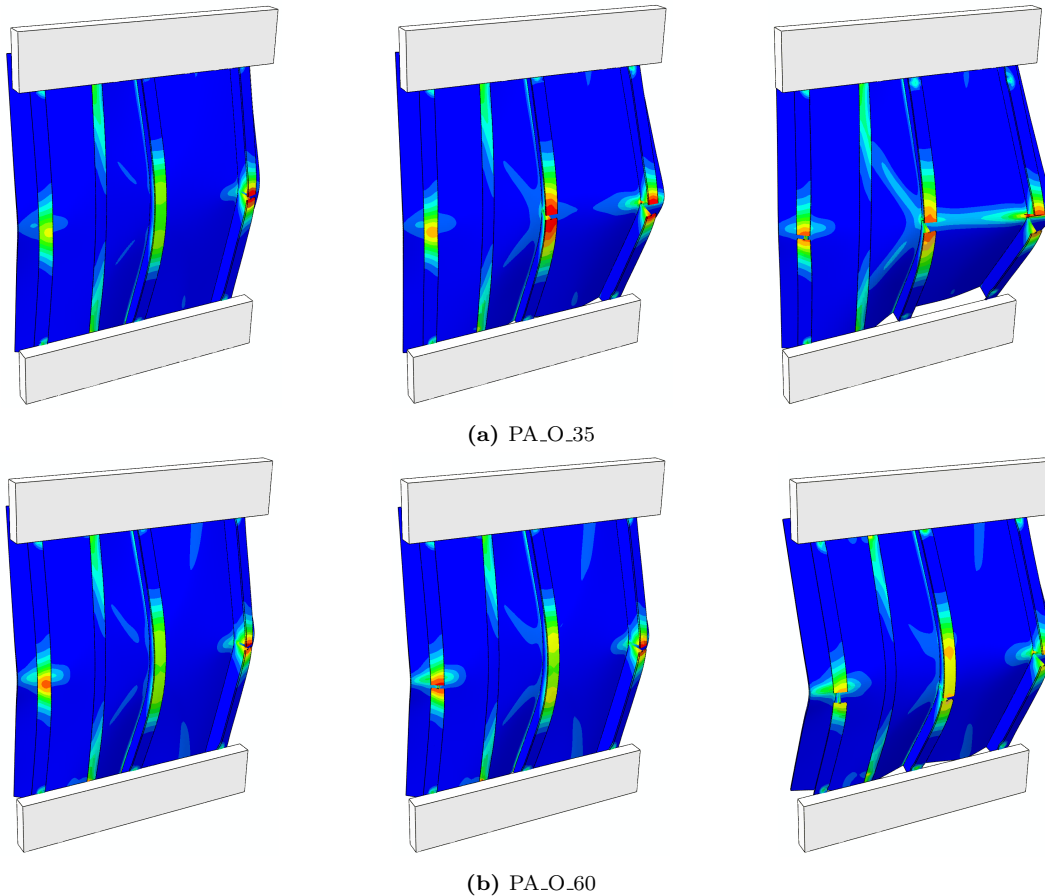


Figure 4.15: Failure modes of the panel, subjected to the CFD loads generated with the open configuration and nominal firing pressures of 35 and 60 bar.

4.6 Resulting Experimental Programme

Based on the knowledge from the simulations presented in this chapter, an experimental test matrix was developed. In Table 4.2, the complete resulting test matrix is displayed. Each test is numbered MN-X-Y. MN denotes rigid plate (RP), aluminium 2 mm plate (PL), or stiffened panel (PA). X indicates the open (O) or wall (W) driven outlet configuration. Lastly, Y indicates the firing overpressure (in bar) of the driver section.

The test matrix includes a rigid plate with pressure sensors to better understand the pressure load. The Schlieren technique - explained in Section 5.2.2 - as well as the rigid plate, will be used to capture the shock

waves' spatial geometry.

Table 4.2: The experimental programme is based on the knowledge obtained in the preliminary studies. The obstacle Wall refers to Figure 2.3a, and the obstacle Open indicates no interference at the outlet of the shock tube. All nominal firing pressures refer to a driver length of 127 cm.

Test nr	Name	Firing Pressure [bar]	Obstacle	Test Specimen
1	RP_O_20	20	Open	Rigid plate
2	RP_O_30	30	Open	Rigid plate
3	RP_O_60	60	Open	Rigid plate
4	RP_W_20	20	Wall	Rigid plate
5	RP_W_40	40	Wall	Rigid plate
6	RP_W_60	60	Wall	Rigid plate
7	PL_O_20	20	Open	Plate 2 mm
8	PL_O_60	60	Open	Plate 2 mm
9	PL_W_20	20	Wall	Plate 2 mm
10	PL_W_60	60	Wall	Plate 2 mm
11	PA_O_20	20	Open	Panel
12	PA_O_30	30	Open	Panel
13	PA_W_20	20	Wall	Panel
14	PA_W_40	40	Wall	Panel

4.7 Concluding Remarks

Concluding remarks of this chapter are listed in this section.

- It should be noted that the objective of the preliminary study was to explore the load magnitudes and the resulting structural responses, in order to develop an experimental programme. The goal was not to obtain accurate results, but to obtain trends. The extreme pressure load is a great uncertainty. The physics of the problem is complicated. Non-uniform pressure loading and experiments on stiffened plates have not previously been conducted in the SSTF. There are no benchmark test results. The numerical models are therefore considered sufficient for qualitative initial studies of the dynamic response.
- The Eulerian simulations generate loads with high magnitude, short duration and non-uniform spatial and temporal distributions. The addition of the wall is predicted to increase the complexity of the load. Complex fluid effects are seen to cause negative overpressures.
- The load magnitudes in the test matrix in Table 4.2 will induce large inelastic deformation (Mode I) for both the plate and the panel.
- Asymmetrical and symmetrical structural responses for both plate and panel are obtained from the spatial and temporal distribution of the non-uniform loading.
- The conducted uncoupled simulations predict that fracture will occur for panel tests at elevated firing pressures.
- All Lagrangian models were modelled as isothermal and rate-insensitive, in compliance with previous work at NTNU [53] [59].
- Parametric studies of the friction coefficient, mesh sensitivity, boundary conditions, and effects of different load magnitudes were conducted. The aim was to discover the sensitivity to and possible effects of different parameters, in order to obtain an impression of plausible uncertainties.

5 Shock Tube Experiments

5.1 Introduction

The SSTF, where the tests in this chapter have been conducted, is briefly explained in Section 2.2. All tests in this study were conducted with a driver length of 1.27 m and with the test specimen placed 0.25 m from the outlet of the driven section. During all tests, sensors in the driver and driven sections provided essential data, like ambient pressure ($p_{ambient}$) and temperature ($T_{ambient}$), firing pressure (p_{driver}), Mach number (M_s), and maximal incident pressure ($p_{so,max}$), as displayed in table 5.1. The sensors in the driven section, which are included in Figure 2.1, were denoted Sensor 1 and Sensor 2. Sensor 1 and Sensor 2 were placed 39.5 cm and 29.5 cm upstream the outlet of the driven section, respectively. For all tests, the timescale was relative to when the shock wave reached Sensor 2. The pressure sensors were operated with a sampling frequency of 500 kHz. Detailed information about the sensors and the data acquisition is provided by Aune in [24]. Only two Phantom v2511 high-speed cameras were available for the tests. The Background-oriented schlieren technique was used on the photo series from one of the cameras in the rigid plate tests, while both cameras were used in a stereo-vision setup to enable three-dimensional digital image correlation for the deformable specimen tests. Each camera recorded the blast event at 37 000 fps with an image size of 768×800 pixels. The images were synchronised with the pressure-time measurements from Sensor 1 and Sensor 2 for all tests.

5.2 Measurement Techniques

The various blast events were documented through the use of high-speed cameras and high-frequency pressure measurements. This section will present the three-dimensional digital image correlation (3D-DIC) and Background-oriented schlieren (BOS) - both of which are techniques that utilise the high-speed cameras.

5.2.1 Three-dimensional DIC

DIC is an optical measuring technique that detects changes between images in image series. In order to obtain a strain and deformation field, a black- and white-speckled pattern is applied to the test specimen, to track displacement and strains. For the shock tube experiments, out-of-plane displacement had to be measured, and thus, 3D-DIC was used. Two Phantom v2511 high-speed cameras were positioned in a stereo vision setup. A total of six pictures - with a varying position of a pre-calibrated cylinder inside the rig-frame - was used for the stereo vision calibration. The cylinder had a diameter of 80 mm and a chequerboard pattern on the surface. The cameras recorded the shock wave event on the flexible structures with 37 000 fps and an image size of 768×800 pixels. The camera calibration and post-processing image analyses were carried out in eCorr [33], following the software documentation [60].

A finite element (FE) formulation of DIC - with a mesh of Q4-elements - was used for the plate. Coarse mesh with element size of 25×25 pixels was used due to speckle pattern was uniform. Obtaining connectivity between the tracking points proved to be difficult for the stiffened plate. Only minor areas could be meshed with both cameras, such as the area between the two right stiffeners. Spatial coordinates of the mesh are accounted for through the calibration process. After a coarse extension of the mesh from the first camera to the second, DIC is performed to optimise the mesh by minimising the difference between the grayvalues of the two cameras. Then, low-pass filtering of the images through the frequency domain with a Fast Fourier Transformation (FFT) was used. A mask out of high frequencies was done before again returning to the spatial image domain. This increases the nodal movement during DIC optimising, and the global minima is obtained with the Newton-Raphson search approach, after some iterations.

Another approach is Subset DIC formulation. By using Subset DIC, the continuity constraint among adjacent elements is lost. Therefore, multiple subsets were used to obtain a sufficiently smooth plot of the deformation profiles. Subsets DIC is useful for point tracking, i.e. midpoints.

The shock tube is free to move in axial direction, and the new rig setup inside the dump tank moves and

oscillates during the loading event. Thus, the rigid body motions of the flexural test structure have to be corrected and accounted for. Rigid body movements of the shock tube and the new rig setup inside the dump tank were accounted for through the use of chequerboard stickers on the rig frame. This enabled the measurement of the movement with Subset DIC. Rigid body movements were relatively small compared to the deformation of the test specimens. Resulting motions for all tests can be seen in Appendix A.2.1.

5.2.2 Background-oriented Schlieren

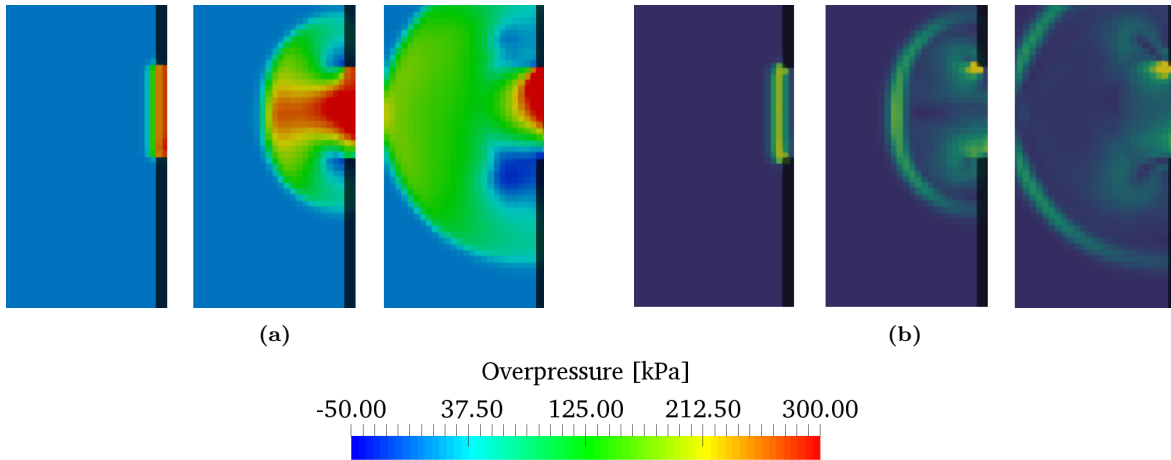


Figure 5.1: Pressure distributions (a) and density gradients (b) at different time steps for the volume between the driven outlet and rigid pressure wall from EPX for the simulation with 25 bar nominal firing pressure and the wall configuration.

Schlieren techniques utilise white light based optics to visualise density gradients in transparent media. Refractive disturbances - which are captured through a system of lenses, mirrors and cameras - are used to determine the density gradients. These optical techniques have been employed to visualise fluid flows, such as shock waves, since the mid-19th century. However, they have been greatly improved through the implementation of digital high-speed video cameras and image-processing software. The BOS is a new synthetic schlieren technique, which distinguishes through a particularly simple setup. BOS requires a well-lit environment, a patterned background and a camera, as shown in Figure 5.2. A speckle patterned background is typical, as abrupt spatial changes are necessary for high contrast images. Through comparing experiment images to a tare image taken with the medium at rest, subtle shifts of the pattern due to refractive disturbances can be registered. Image processing software can relate the displacements of the background pattern to the gas density through the Gladstone-Dale equation. Pseudo-schlieren images can then be constructed based on the density distribution. The method and images are labelled as synthetic and pseudo-schlieren, respectively, as the digital nature of BOS stands in contrast to classical schlieren. [61] [62]

In this study, BOS was used to visualise the shock wave between the outlet of the driven section and the rigid plate, not to provide any quantitative information. To exemplify the difference between a density gradient and a pressure distribution Figure 5.1 provides a comparison between a shock wave and the density gradient resulting from its motion. The visualisations are taken from the CFD simulation conducted with wall configuration and 25 bar nominal firing pressure in Section 4.4. As can be seen in the figure the trajectory and spatial distribution of the shock front is well represented by the gradient, but variances within the shock wave is lost.

The setup and results are elaborated on in Section 5.3.1 and 5.3.4. The in-house BOS code [63] at SIMLab was utilised to create the pseudo-schlieren images.

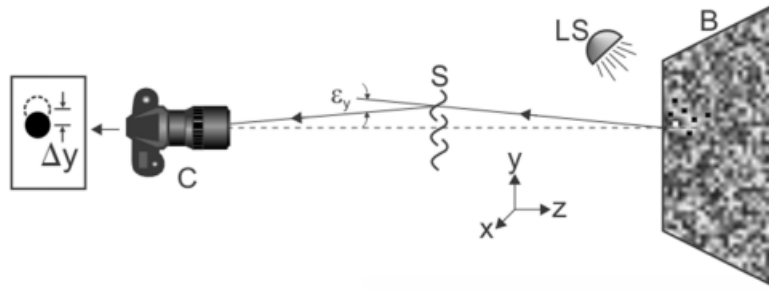
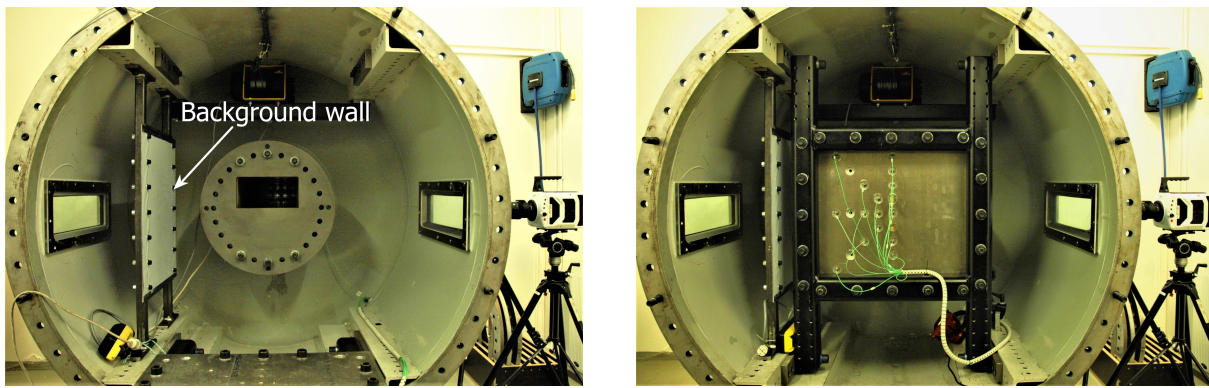
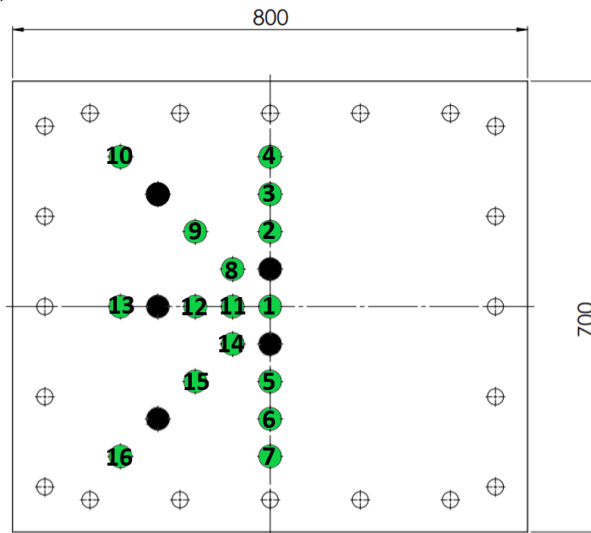


Figure 5.2: Diagram of the optical system required for the background-oriented schlieren technique. S denotes the refractive disturbances in the medium. The figure is an edited version of a figure from Settles and Hargather [61].



(a)

(b)



(c)

Figure 5.3: (a) The experimental setup with the wall configuration and the massive plate laid down, emphasising the BOS part of the setup. The light source is in the part of the tank behind the camera. (b) The experimental setup with the rigid plate and sensors in place. (c) The position of the pressure sensors and their numbering. Only green numbered holes are equipped with sensors. All dimensions of the rigid plate with sensor locations are in the Appendix.

5.3 Rigid Plate

The rigid plate tests were performed on a massive aluminium plate equipped with pressure sensors. These tests were conducted in order to determine the approximate spatial and temporal pressure distribution on the deformable test specimen, and to visualise the shock wave propagating from the driven outlet to the test specimen. The pressure data was imperative in this study, as it enabled quantitative evaluation of the Eulerian simulations from Section 4.4. Two additional tests were performed at a nominal firing pressure of 20 bar with the wall configuration in addition to the tests presented in Table 4.2. The reason for one of the additional tests was an error with the light source, which made it impossible to produce BOS images. The second additional test was performed without the background plate needed for the BOS images, to assess whether or not the plate affected the pressure measurements. The three RP_W_20 tests are denoted X_1, X_2 and X_3, where RP_W_20.2 is the test producing clear BOS images and RP_W_20.3 the test without a background plate.

5.3.1 Experimental Setup

The rigid plate configuration of the rig is explained and shown in Section 2.5. The rigid plate is a 25 mm thick 800 mm x 700 mm aluminium plate, with holes as shown in Figure 5.3c. The holes along the boundaries are for bolting purposes, while the remaining 21 holes are intended for the mounting of pressure sensors. Due to equipment limitations, 16 sensors were mounted on the plate in this study. The naming convention of the sensors were PC_XX, where XX corresponds to the number in the figure. Identical sensors to the ones used in the driver and driven sections were used on the rigid plate, and the same same sampling frequency of 500 kHz was employed. The rigid plate was placed 0.25 m from the outlet of the driven section, to be consistent with the tests on the deformable specimen.

To visualise the geometry of the shock wave, BOS was utilised. For this purpose, one of the Phantom v2511 high-speed cameras was set to capture the area between the driven outlet and the rigid plate, and a speckle patterned wall - hereby denoted the BOS-wall - was mounted to provide a background with abrupt spatial changes. The experimental setup is shown with and without the massive plate for the wall configuration in Figure 5.3.

5.3.2 Measurement Inaccuracies

The pressure measurements from the shock tube tests are typically filtered numerically to remove measurement noise from various sources. This section outlines the measurement noise observed in this study, it identifies most of the sources and presents the filtration procedure.

There were three frequency-related noise sources in the pressure measurements: One source was the high-frequency oscillations in the sensors. A second source was the spikes and high-frequency oscillations due to membrane pieces interacting with the sensors. A third source was the distinct lower frequency (relative to 500 kHz) for the PC_08, PC_11 and PC_12. This created oscillations with large amplitudes, not replicated by the other sensors.

Regarding the first source, high-frequency oscillations occur when the sampling frequency is close to the eigen frequency of the pressure sensors [24] - which was close to 500 kHz for both in this study.

Regarding the second source, the piezoelectric sensors made for measuring gaseous pressure are very sensitive, and they are not intended to interact with solid matter. Hence, the measurements resulting from membrane interactions are very apparent. Spikes with magnitudes of several times the initial peak pressure and high-frequency oscillations with mid-range amplitudes can not be created from gaseous behaviour in a shock tube environment. There were not any disturbances detected around the peak pressure for any tests, which was as expected since the shock front travels faster than the membrane pieces. No membrane interactions were detected before the 10 ms mark. The interactions were more prominent for the elevated firing pressures and the tests with the open configuration. The reason for the first trend was twofold. First, more / thicker membranes were needed for increased pressures, which increases the total volume of membrane pieces.

Second, increased pressures cause messier tears in the membranes, which leads to more free-flying pieces. The second trend was very logical; With an obstacle at the end of the driven section, less of the membrane pieces make it out of the driven section - directly due to the physical barrier and indirectly due to the complex flow effects it leads to.

The third reason for the oscillations in the three aforementioned sensors is unknown. However, there are at least two logical explanations: a) hardware / user faults like mounting errors, damaged sensors and dirty connectors [64] and b) vibrations in the rigid plate that can interfere with the measurements. One typical mounting error where the threads do not align is shown in Figure 5.5b. The fact that the three sensors were grouped together indicates explanation b), but the fact that there were no traces of the oscillations in the measurements from the surrounding sensors contradicts this notion. Due to symmetry, the measurements from PC_14 and PC_08 were expected to closely resemble each other for the tests with the open configuration. However, as can be seen in Figure 5.4c, this was not the case.

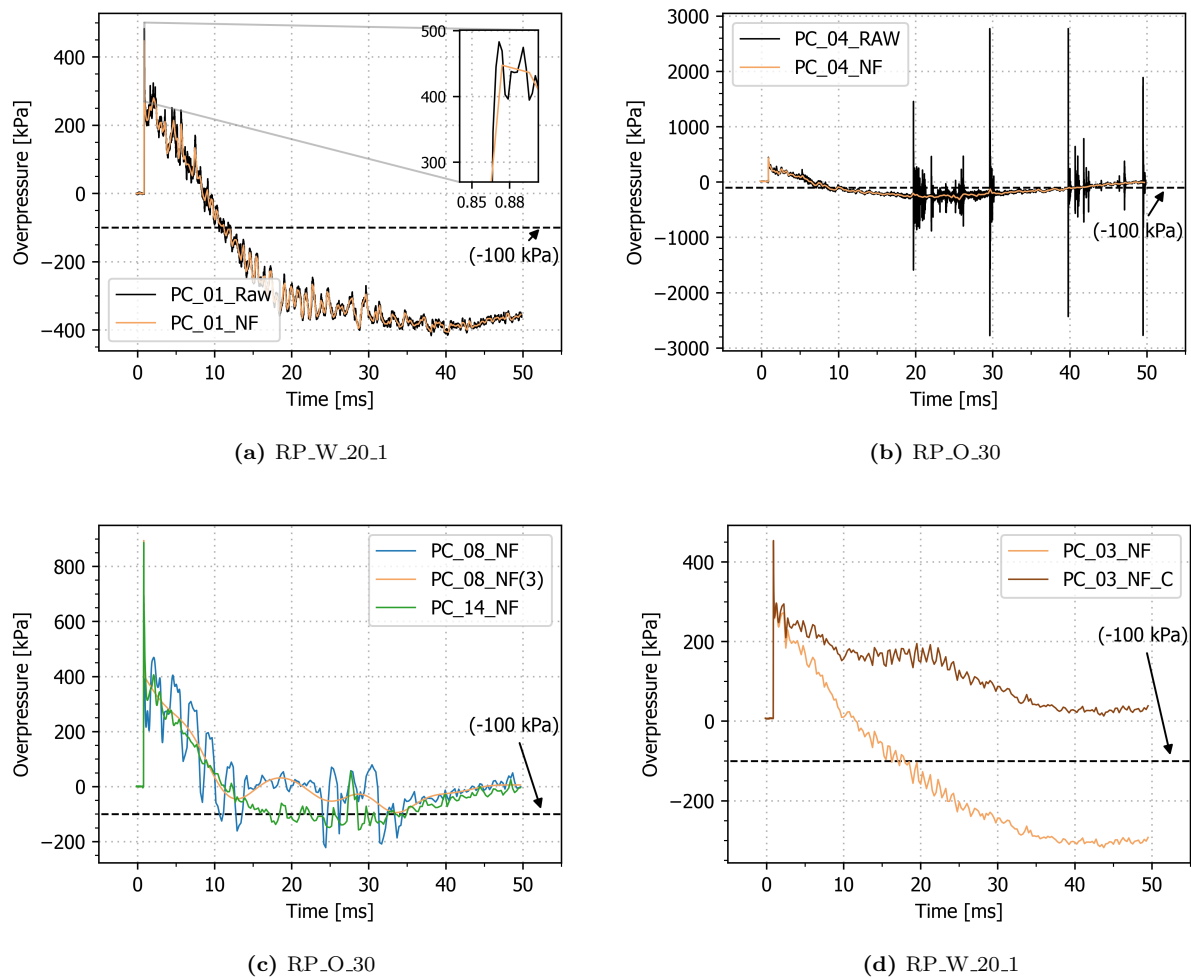


Figure 5.4: Noisy raw pressure measurements and filtered/corrected data: (a) High-frequent sampling noise, (b) Membrane interaction noise, (c) Large amplitude oscillations, (d) Spurious drift.

In order to negate the noise, the data collected from the pressure sensors was processed with numerical filtering. In order to remove source 1), a five-point running average was applied to all the pressure data.

Figure 5.4a displays the effect of the averaging by highlighting the peak pressure. As a monotonic increase in the peak pressure is expected, the filtered data better represents the physical behaviour. All peak pressures in Table 5.1 were extracted with the running average centred on the measured maximum. The effects of second source (membrane debris) was - as previously stated - very apparent, which made it easy to assess the proficiency of the filtering scheme. An effective scheme consisting of a spike removing algorithm, a lowpass-filter and two additional five-point averaging runs was designed, of which results are shown in Figure 5.4b. This scheme was applied after the peak pressure for each data set. The lowpass filter was a digital Butterworth lowpassfilter with the critical frequency set to 1% of the Nyquist frequency. The filter was applied both forwards and backwards in order to avoid a phase shift.

For RP_O_60, the membrane interaction dominated the pressure measurements past 25 ms. Therefore, the data past that point was not considered. The noise was less prominent for the remaining tests, and could be removed without compromising the real pressure measurements. To rectify noise the third source (lower frequency oscillations with large amplitude), the critical frequency of the lowpass-filter was set to 0.05% of the Nyquist frequency rather than 1%. As can be seen in Figure 5.4c, the filtered PC_08 data closely resembles the PC_14 data. The complete filtering script is included in the appendixes.

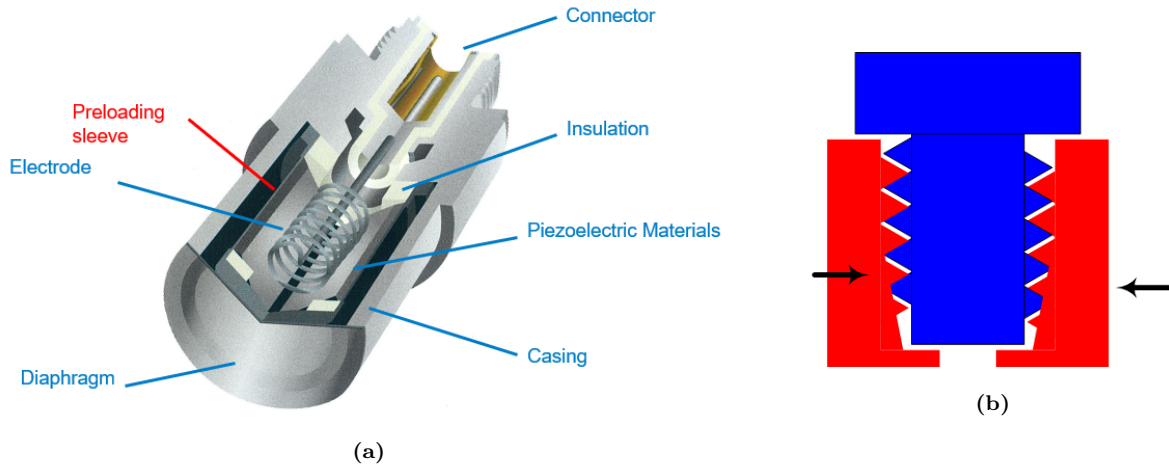


Figure 5.5: (a) Assembly drawing of a piezoelectric pressure sensor. (b) Typical mounting error for piezoelectric sensors, where the threads do not quite fit. The figures were provided by Kistler Nordic DK [64]

From the pressure measurements in Figure 5.4, it is evident that there is a negative spurious drift in the pressure measurements. The drift seems to gradually increase in magnitude, with some exceptions. An overpressure of -100 kPa corresponds to perfect vacuum, which is impossible on earth [65]. However - as can be seen in Figure 5.4 - far lower pressure levels were measured in this study. The spurious drift seems to be linked to the complexity of the flow, as the drift is more severe for the tests with the wall configuration than the open configuration. The drift is also observed to be more significant for the sensors on the upper half of the rigid plate than the sensors on the lower half for the wall configuration tests, while they are similar for the open configuration tests. More importantly, though, is the fact that the only place where non-physical negative pressure values have been observed in the traditional SSTF setup is shortly downstream the firing section. The way the membranes fracture and open causes a complex flow. The spurious drift is also seen to increase with increasing firing pressure, likely due to increasing velocities which further increase the complexity of the flow. The spurious drift is observed for all sensors on the rigid plate as well as for Sensor 1 and Sensor 2 in the driven section.

Even though the spurious drift is linked to the complexity of the airflow, the actual cause of the noise is uncertain. In the data sheet for the sensors used in this study - which are designed for shock tubes - the

following is written: "The sensor Type 603B is especially suited for measuring pressure fluctuations of high frequency resp. short rise time in heavily vibrating measuring objects." [66]. This indicates that they should be perfect for the conditions in this study. Due to the sensor drift being inherently negative, thermal shock was investigated as a possible reason for the drift. Thermal shock is a common problem in metrology, as all piezoelectric sensors are sensitive to it, and it accompanies pressure pulses in many applications such as for free-field blasts. When the stress level of the quartz crystals changes, they release a charge. In a piezoelectric sensor, these charges are converted to readable measurements. To be able to measure pressure levels lower than the calibration pressure, the crystals are preloaded. When the outer casing of the piezoelectric sensor heats up, the casing expands, which leads to a reduction of the preload force. The crystals then experience less tension, which causes negative signal outputs. The assembly of a piezoelectric sensor can be seen in Figure 5.5a. The thermal shock effects are difficult to isolate and quantify and must therefore be anticipated and minimised. In shock tube application it is recommended to insulate the sensors. Therefore, the sensors in this study were protected by a thin layer of insulating silicone. The heating in this experimental setup is no larger than for the traditional setup, however. Hence, it is unlikely that the thermal shock has a considerable effect on the measurements.

As the filtered pressure measurements are non-physical, an attempt to rectify the data was performed. Due to the spurious drift being near impossible to isolate, it was decided to attempt to use the expected negative phase as a correcting factor based on best available literature. In traditional blast mechanics, the momentum of air during a blast event results in an overexpansion, which leads to pressures below ambient level behind the blast wave. This period of negative overpressure - which is called the negative phase - causes particles to flow back towards the blast centre. The influence of the negative phase of the blast event is usually neglected in blast-resistant designs, and little research exists. However, it is a topic that has gained some attention recently.

Rigby et al. [56] used the data in [67] to determine empirical relations between the negative reflected pressure and the positive reflected pressure - among others - for hemispherical surface bursts. They found the negative reflected pressure to increase in magnitude with the positive reflected pressure. They also found that positive reflected pressures of 20000 kPa and above corresponded to negative reflected pressures close to -100 kPa. The largest positive reflected pressure of this study was 1717.1 kPa which corresponds to a negative reflected pressure of -50 kPa. They investigated a traditional undisturbed shockwave loading on infinitely large plates, which is quite different than what was looked at in this study. In fact, the CFD simulations in Section 4.4 indicate the opposite trend for the open configuration, as no negative overpressures were measured on the rigid pressure wall with a nominal firing pressures of 25 bar and above. Figure 4.6f and Figure 4.7c suggest that the negative values in the low nominal firing pressure range is caused by complex flow effects - and not overexpansion - as negative values only are measured in the corners. Complex flow effects seem to be the cause of the negative phase in the simulations conducted with the wall configuration as well, as Figure 4.6l and Figure 4.7d show that only parts of the wall are subjected to underpressure. These results suggest that the pressure load on the rigid plate is greatly influenced by flow effects, and that traditional blast mechanics have limited applications for the extreme pressure loading explored in this study. However, the loading environment is similar - at least for the open configuration. Furthermore, as the pressure measurements were intended to validate the CFD, the CFD could not be used to rectify the measurements. Therefore, the parameters found by Rigby et al. [56] were used.

As the measurement drift was seen to gradually increase, the measurements were corrected accordingly. The minimal measured value for each test was found and compared to the expected minimal value based on the work by Rigby et al. [56] and Equation (5.1). p^C denotes the corrected pressure, while p^{NF} denotes the numerically filtered pressure measurements. The difference was then added to all pressure measurements from the time of the measured minima to the end of the measurements. Between the peak reflected overpressure and the measured minima, the value added to the measurements increased linearly. This is shown in Equation (5.2). The result of the correction algorithm is displayed in Figure 5.4d. The complete correction script can be seen in the appendixes.

$$\Delta p = p_{ro,min}^{Rigby} - p_{ro,min}^{NF} \quad (5.1)$$

$$p^C = p^{NF}, \quad t \leq t(p_{ro,max}^{NF})$$

$$p^C = p^{NF} + \Delta p * \frac{t - t(p_{ro,max}^{NF})}{t(p_{ro,min}^{NF}) - t(p_{ro,max}^{NF})}, \quad t(p_{ro,max}^{NF}) < t \leq t(p_{ro,min}^{NF}) \quad (5.2)$$

$$p^C = p^{NF} + \Delta p, \quad t(p_{ro,min}^{NF}) < t$$

5.3.3 Experimental Results

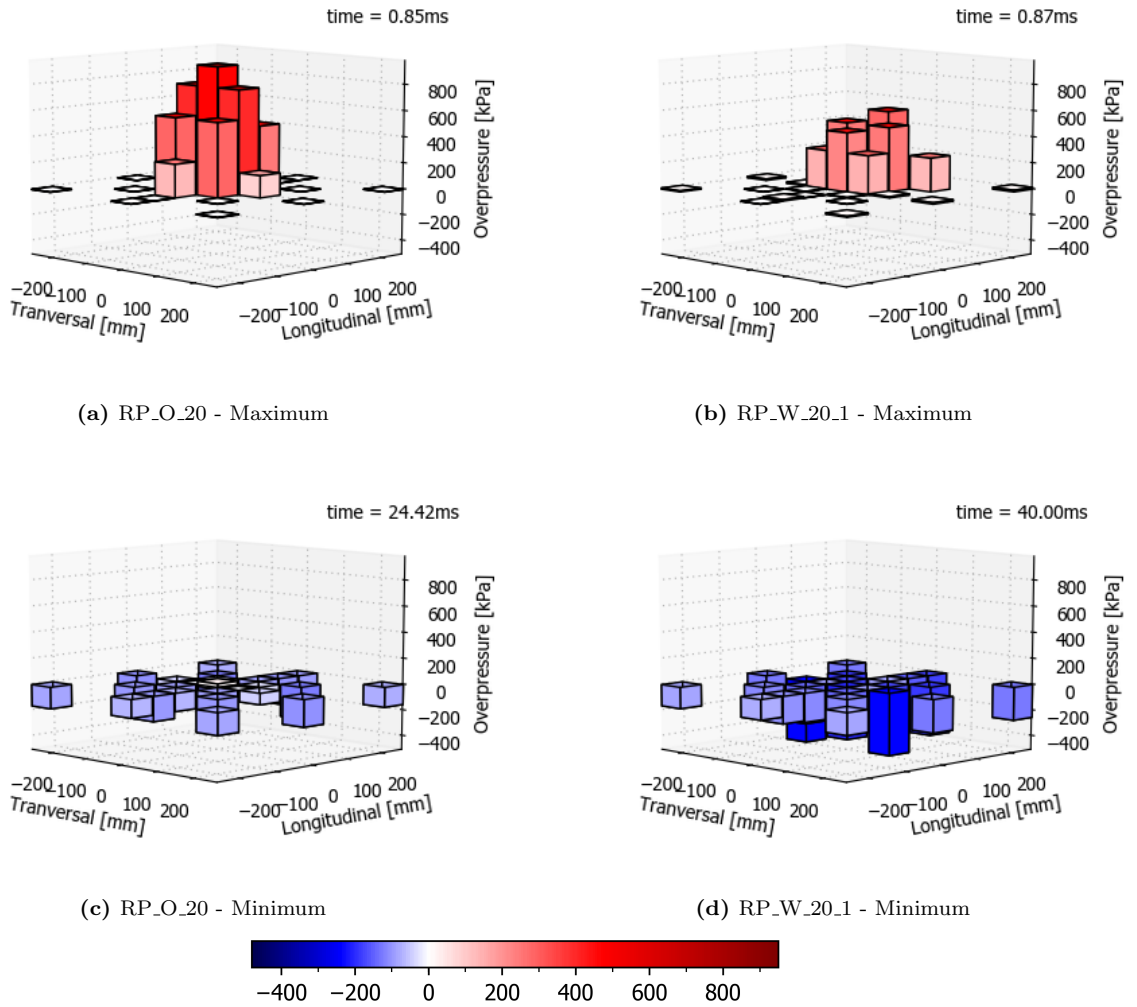


Figure 5.6: Visualisation of the pressure level measured at each sensor at the time of maxima and minima of the numerically filtered pressure measurements from RP_O_20 and RP_W_20.1. The plots are mostly representative for all simulations.

Assessing the effectiveness of the correction of the spurious drift is impossible by simply looking at the resulting pressure measurements. Hence, the measurements presented in the following subsection are numerically filtered to negate the frequency-related noise sources, but they are not corrected for the spurious drift. Both the corrected and uncorrected pressure measurements are assessed in Section 6.3.2.

Table 5.1: Measured firing parameters, blast parameters and peak reflected overpressures from the tests on the rigid plate.

Test	Firing conditions			Parameters driven Sensor 2		Parameters rigid plate	
	p_{driver} [kPa]	$p_{ambient}$ [kPa]	$T_{ambient}$ [°C]	M_s []	$p_{so,max}$ [kPa]	$p_{r,max}$ [kPa]	$p_{r,max}$ [kPa]
RP_O_20	2161.0	101.3	21.4	1.76	274.9	951.0	643.8
RP_O_30	3117.8	101.4	22.7	1.87	372.8	1180.5	808.5
RP_O_60	6208.7	101.4	23.3	2.05	469.7	1732.1	1224.1
RP_W_20_1	2166.2	101.3	22.2	1.78	302.2	448.0	581.2
RP_W_20_2	2165.9	101.0	22.7	1.74	265.4	408.3	521.9
RP_W_20_3	2164.4	100.9	22.8	1.76	289.5	434.9	565.1
RP_W_40	4066.3	101.3	23.4	1.94	401.2	637.7	844.8
RP_W_60	6210.8	100.9	23.9	2.02	466.4	725.9	1015.5

The relation between the firing conditions and the driven parameters in Table 5.1 is consistent with what has been previously measured in the SSTF, as presented by Aune in [24]. Small variations are found between tests conducted with the same nominal firing pressure, largely due to slight variances in the tearing of the membranes. All shock waves are in the supersonic regime. As expected, the maximal peak reflected overpressure was registered at different sensors for the two configurations. The maximal values were measured at PC_01 for the tests with the open configuration, while they were measured at PC_02 for the tests with the wall configuration. The location of the true maximal pressure for the wall configuration tests was most likely somewhere in between the positions of PC.01 and PC.02. However, due to limited sensors, the measurements were taken at face value. $p_{r,max}(PC_{02})/p_{r,max}(PC_{01}) \approx 70\%$ for the open tests, and the percentage seems to increase with increasing nominal firing pressure. For the tests with the wall configuration, $p_{r,max}(PC_{01})/p_{r,max}(PC_{02}) \approx 75\%$, and the percentage seems to decrease with increasing nominal firing pressure.

The spatial pressure distribution across the rigid plate sensors is visualised at maximum and minimum for the open and wall configurations in Figure 5.6. For consistency, the same visualisation style used in Figure 4.7 is implemented here. Therefore, each sensor is represented by a column with 50 mm x 50 mm base. Transversal symmetry was applied to better visualise the distribution. The spurious drift is very apparent in the minimum figures, as most sensors indicate pressure levels of -200 kPa or below. The maximum figures indicate that the peak reflected overpressure occurs before the shock wave has covered most of the rigid plate. This, as well as the sharp decline in pressure levels from the peak sensor, highlight the non-uniformity in the spatial distribution achieved by placing the test specimen at a distance from the driven outlet.

The overpressure-time histories of the sensors subjected to the maximal pressure and the sensor expected to be subjected to the minimal pressures are shown for all tests in Figure 5.7. It is interesting to note that the spurious drift is more prevalent for the tests with the wall configuration, and that the spurious drift seems minimal at PC_01 for the open tests. Some of the trends found for the CFD simulations in Section 4.4.3 can also be found for the experimental data - such as the delayed transfer of energy for the tests executed at elevated firing pressures. However, they are difficult to compare due to the noise. The CFD data and experimental data will be compared in Section 6.3.2.

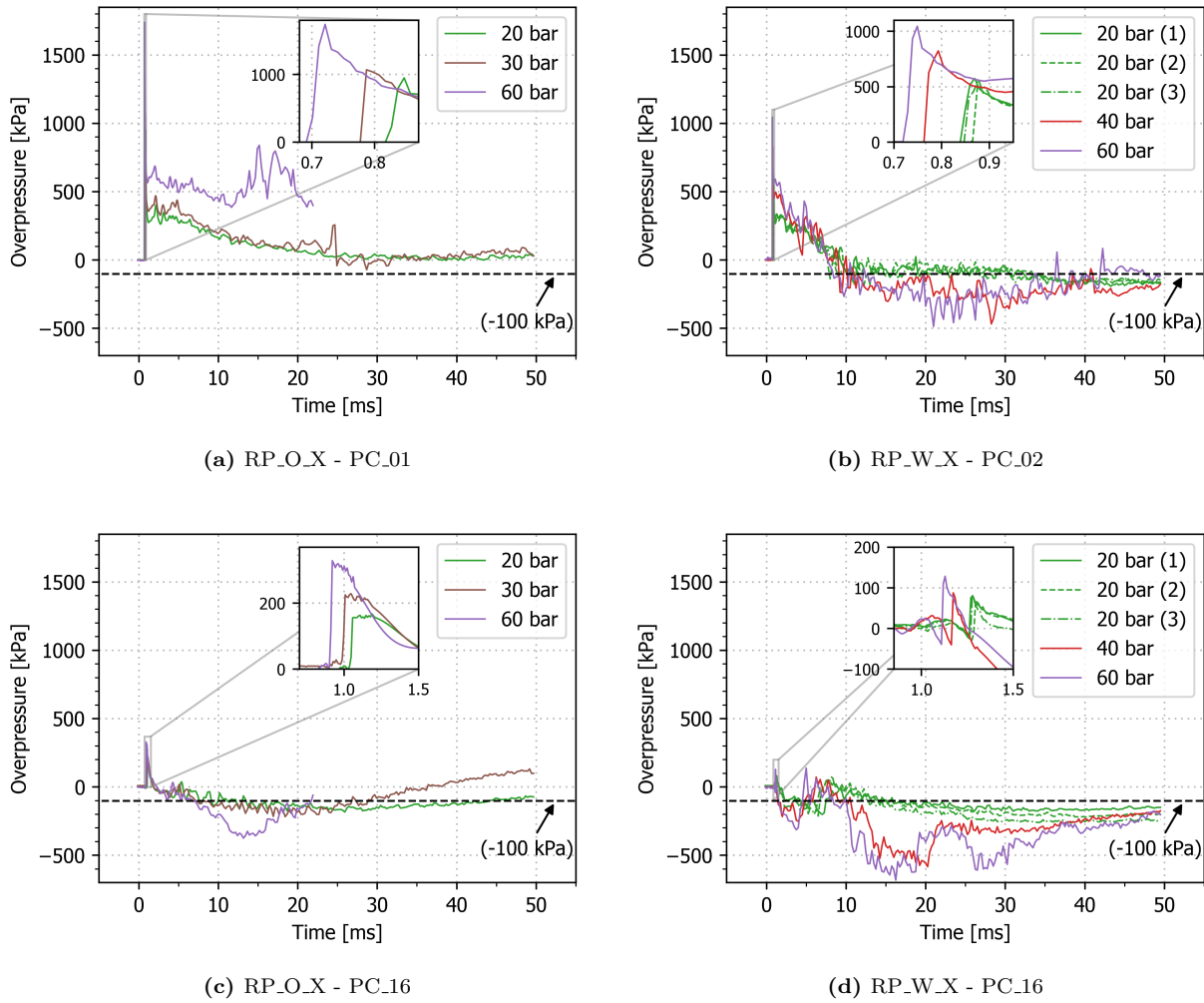


Figure 5.7: Overpressure-time histories of the sensors containing maxima and the sensor expected to contain the physical minima for all nominal firing pressures and both driven outlet configurations.

As previously stated, three tests with the wall configuration and a nominal firing pressure of 20 bar were conducted to assess the effect of the BOS-wall on the pressure measurements. At sensor PC_02, there is no noticeable difference between the three tests. Nonetheless, the measurement data from the three tests diverge from about 15 ms for PC_16. PC_16 is one of the sensors closest to the BOS-wall, while PC_02 is one of the sensors furthest away. From these data sets, it is possible to suspect that the BOS-wall slightly affects the closest sensors. In spite of that, PC_10 and PC_13 (not displayed) did not show any signs of diverging. Hence, the BOS-wall is assumed to have a negligible effect on the measurements.

In Figure 5.8, the overpressure-time histories from the sensor subjected to the maximal pressure, the sensor expected to be subjected to the minimal pressure and an additional sensor history is presented. The maximal and minimal pressure curves' tendency to enclose the remaining pressure curves - as seen in Figure 4.9 - is mostly found in the open tests. This tendency does not present itself in the tests with the wall configuration. The said trend indicates that the sensors are affected quite similarly by the spurious drift for the open configuration, and that the effect is less uniform for the wall configuration.

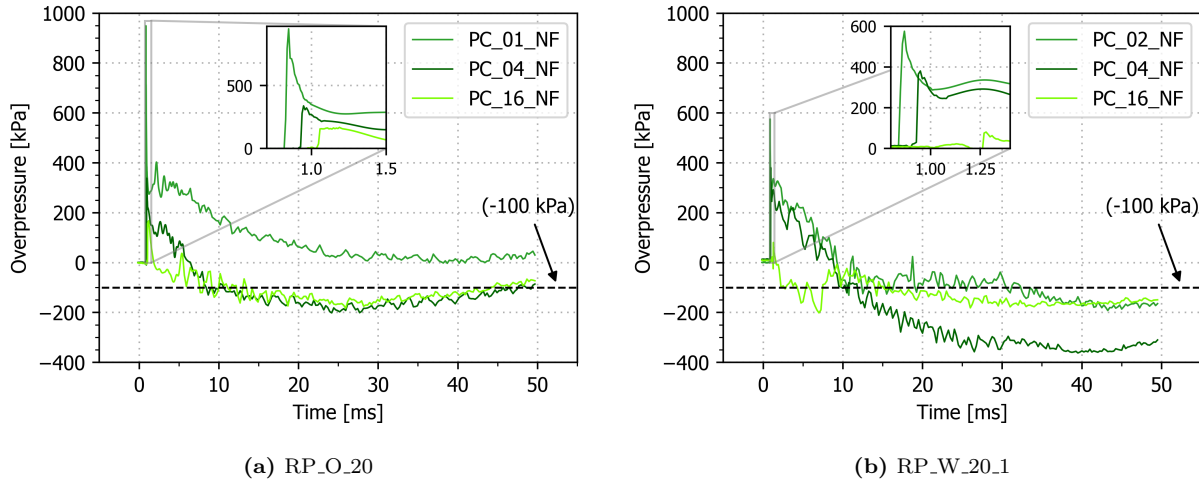


Figure 5.8: Overpressure-time histories from sensors capturing the overall shape from two of the tests conducted with a nominal firing pressure of 20 bar.

5.3.4 Shock Wave Geometry

Images capturing the pressure gradient in the volume between the driven outlet and the rigid plate are shown for both RP_O_20 and RP_W_20.2 in Figure 5.9. The air flow of the tests with each configuration closely resemble each other, hence, the images are representative for all tests. The images are a result of applying the BOS technique explained in Section 5.2.2. The gradients for each configuration both take a spherical shape as they exit the driven outlet, although the gradient from the open configuration remains relatively close to uniform. As is natural for spheres, the shock waves initially make contact with the rigid plate at a single point, before gradually enveloping the plate. As the shock wave of the open configuration is semi-uniform - and makes initial contact at the centre - it quickly covers the plate and establishes a stable wall of particles on the plate surface. The gradient of the wall configuration takes substantially longer to cover the plate, as it is significantly more spherical and makes initial contact above the plate centre. The figure indicates that the wave mainly travels down- and upstream for the open configuration, with limited complex flow effects. Thus, the increased complexity introduced to the flow by the wall is evident in the stark contrast between the flow effects following the initial reflection of the shock wave off the rigid plate. The flow in the wall images is clearly messier. The images roughly correspond to the images of the pressure distributions from the CFD simulations in Figure 4.6 with respect to time. Furthermore, the spatial distributions are very similar. The similarity in the images - and the fact that Figure 5.9f and Figure 5.9l show clear signs of buildups of gas - further indicate the validity of the CFD simulations and the measurement errors of the pressure sensors. As previously stated, these images and the use of BOS in this study is merely intended for visualisation purposes.

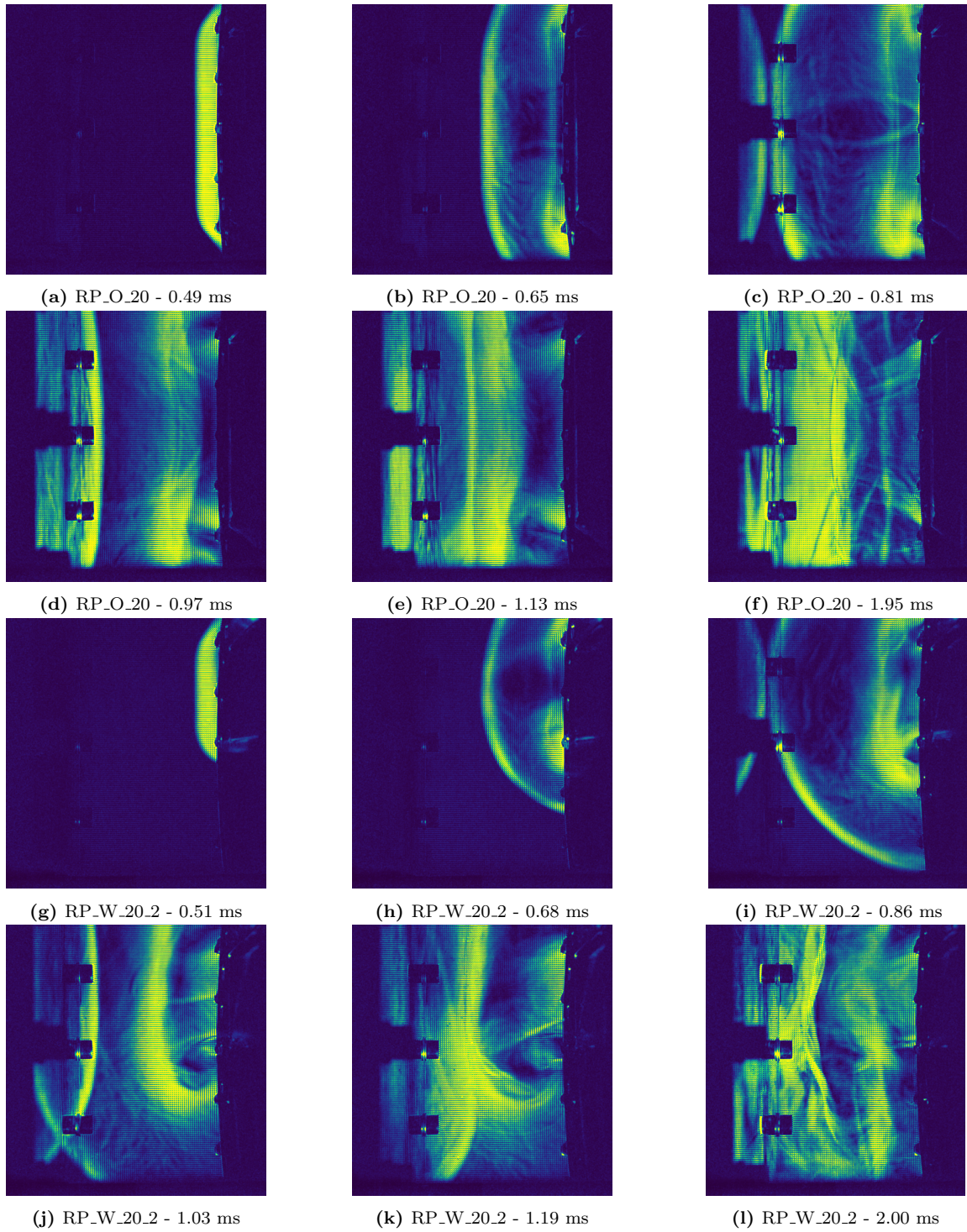


Figure 5.9: The shock wave as it flows from the driven outlet to the rigid plate, as well as the subsequent flow effects for RP_O_20 ((a)-(f)) and RP_W_20.2 ((g)-(l)). The images are representative for all tests with the same configuration.

5.4 Plates

The obtained dynamic response of the flexible aluminium plates will be presented in this section. First, a brief introduction of the experimental setup not previously covered will be given.

5.4.1 Experimental Setup

The 2 mm aluminium 6082 T6 alloyed plate, Figure 5.10a, is clamped in the clamping frame configuration illustrated in Figure 2.5b and Figure 5.10b, with 28 M12 12.9 grade steel bolts in an attempt to achieve fixed boundary conditions. The bolts were tightened to an estimated torque of $50Nm$. The rolling direction of the plate is oriented vertically. As mentioned in Section 5.2.1, to track deformation with high-speed cameras for 3D-DIC, the plates were manually spray painted with a perforated template to obtain the speckle pattern. The entire back side of the plate was covered in paint. This may result in a different friction between back frame and plate for each test. The experimental setup is further described in Section 2.5.

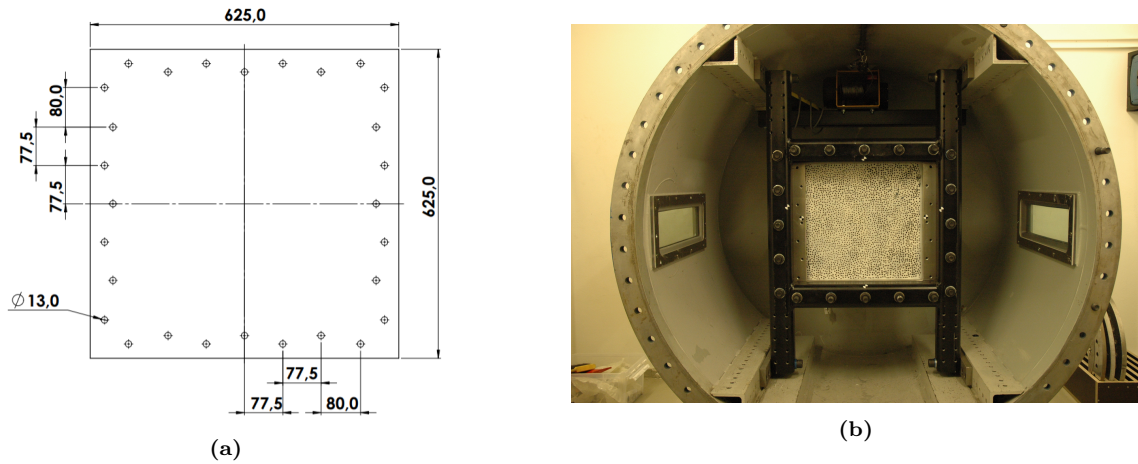


Figure 5.10: Illustration of (a) the plate dimensions (626 mm x 625 mm x 2mm) and (b) the mounting of the plate in the shock tube. The BOS wall was removed prior to the flexible structure test.

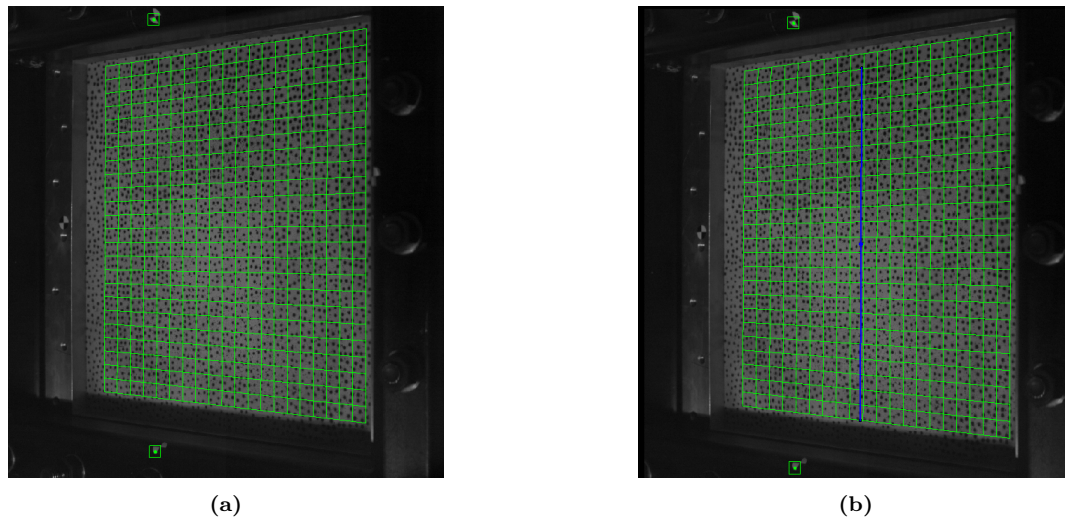


Figure 5.11: Representative illustration from eCorr [60] of (a) the mesh of the plate used for FE based DIC and (b) cross section vector over the mesh for obtaining profile deformation of the plate.

5.4.2 Experimental Results

The following section will present the experimental results of the plate. As mentioned in Section 5.2.1, FE-based DIC was used on the plate. The mesh of a representative test is shown in Figure 5.11a.

Figure 5.12 presents the experimentally obtained midpoint deflection history, measured with the FE-based 3D-DIC. All curves are corrected for the rigid body movement of the setup and facility. Positive direction is defined as upstream the shock tube. Time is shifted to equal zero when shock wave arrives at Sensor 2. Sudden drops in midpoint deflection after initial deflection are associated with diaphragms debris hitting the plate, and the cross indicates when diaphragms debris perforate the plate for the PL_O_60 test.

It is observed that all the tests first exhibit a rapid increase in the inelastic displacement before undergoing a phase of oscillations in the negative direction and Mode I [6] classified failure. When comparing the wall configuration to the open configuration at the same nominal firing pressure, it is evident that the wall configuration decreases the deflection of the plate. No visible signs of tearing along the boundaries or local necking were observed. Deformation of the bolt holes on the plate was observed after the tests. The holes close to the middle of edge to the plate deformed the most. The severe straining around the bolt holes was visually observed to increase with increasing inelastic deformation of the plate.

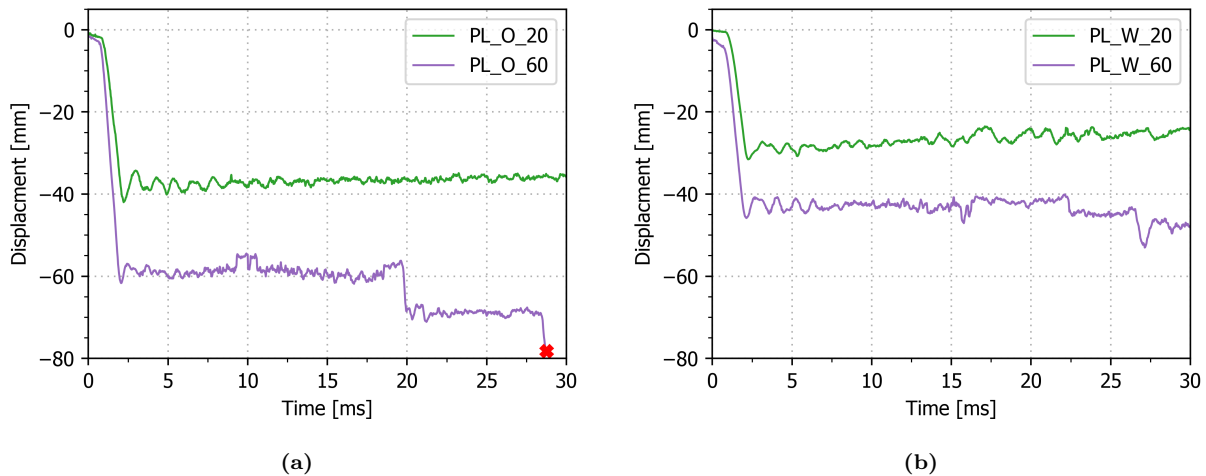


Figure 5.12: Midpoint deflection history, measured with 3D-DIC for plates. Curves are corrected for rigid body (RB) movements. Data is synchronised with time zero as shock wave passes Sensor 2. (a) is for open configuration and (b) is for wall configuration. The Red X indicates when the Melinex diaphragms debris perforating plate PL_O_60.

In Figure 5.13, the deformation profiles corresponding to maximum deflection - 80% of max, 60% of max, 40% of max and 20% of max - are presented. The max deflection is measured during the first 10 ms; After that, diaphragm debris hit the plate, giving invalid results. The cross section deformation is extracted by defining a vector manually in eCorr over the supposed centre line of the plate, as illustrated in Figure 5.11b. The plate midpoint (in Figure 5.12) is the centre of the vector, and its vertical coordinate in eCorr was defined as zero along the position axis in Figure 5.13. Doing the exercises of defining the vector manually - only using visual inspection - introduces uncertainties. It is observed that the deformation profile are not what one may expect from a impulsive response, but rather a quasi-static or dynamic response profile, confirming that the load are in the dynamic loading regime.

It is evident that the configuration with the fluid obstacle wall, influenced the symmetry of the dynamic response. The point of maximum deflection as the deformation profile progresses is marked with a red dot in

Figure 5.15. A constant time of 0.027 ms is between the red points in the figure. Maximum deflection point moves to the left as the deflection progresses until a turning point at around -75 mm for the PL_W_60 test. An interesting observation is that after the turning point, the point of maximum deflection moves towards the centre as the velocity of the midpoint of the plate becomes zero. The maximum deflection of the plate are located in the centre. A plausible explanation is that the non-uniform spatial pressure distribution initiate a non-uniform velocity field where the left side has the greatest velocity. As the inelastic deformation increases the membrane force increases and the effect of the boundary condition starts to dominate the response rather than the load.

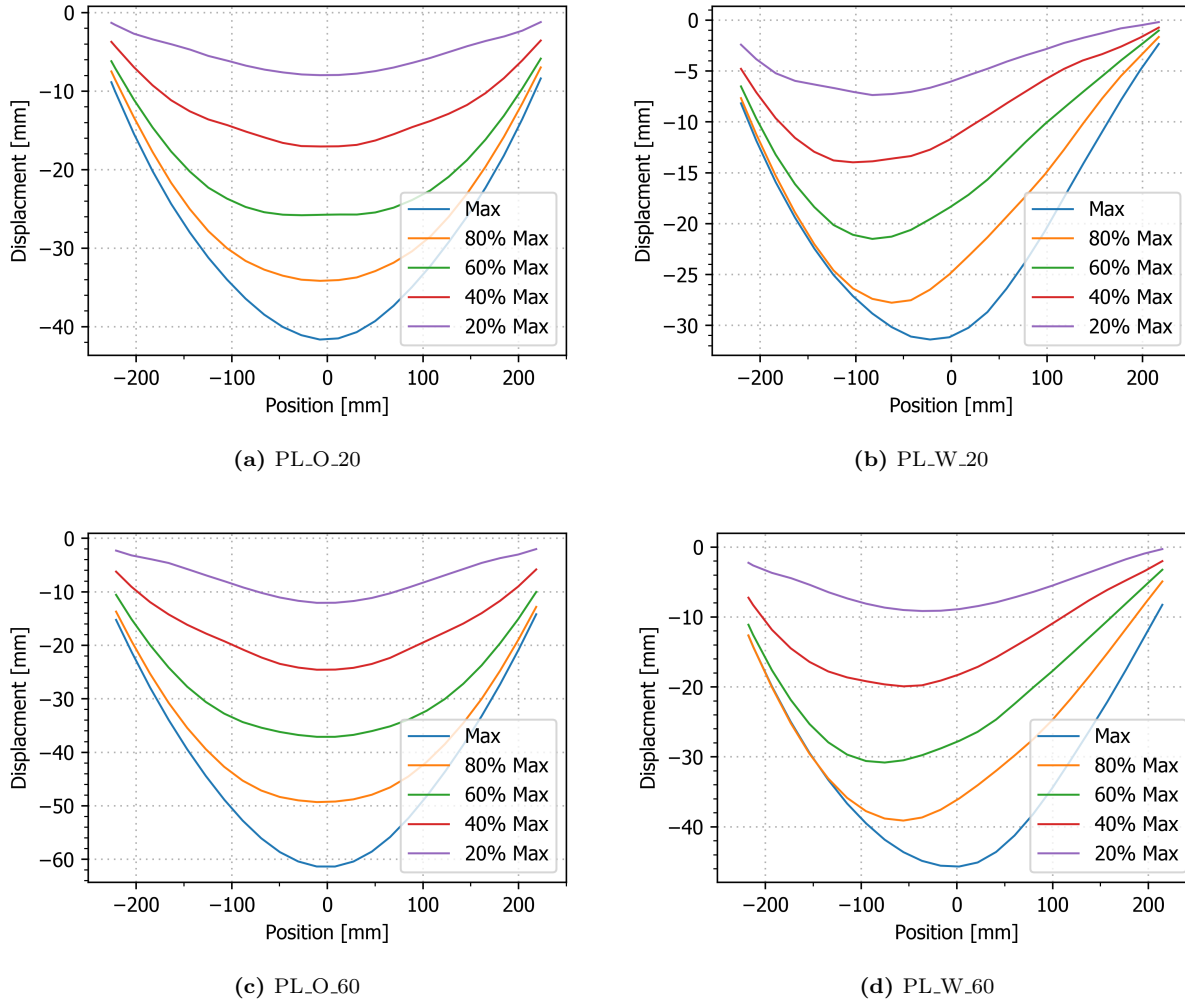
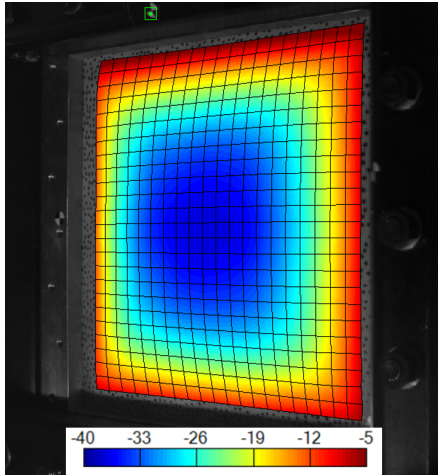
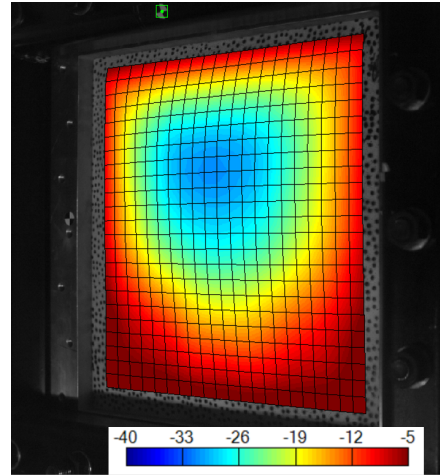


Figure 5.13: Deformation cross section profiles measured with FE DIC for plates.

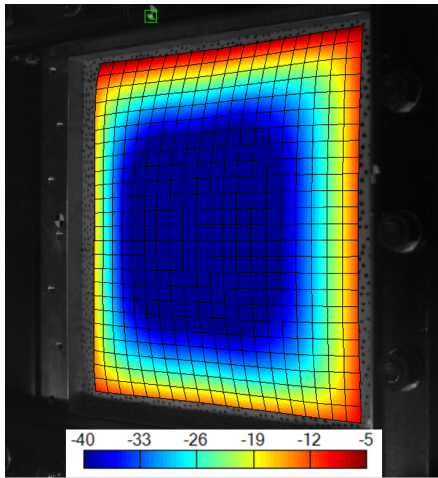
From Figure 5.14 one can observe the deformation field for open and wall configuration with 60 bar firing pressure. It is interesting to note the effect of difference non uniform loading. At 60% and 80 % of maximum deflection wall have more localised deflection at the top of the plate. Open are as expected experiencing most deflection in the centre of the plate. As the deflection progresses further towards maximum deflection both configuration tend to have more similar spatial distribution of deflection due to the boundary influencing the response.



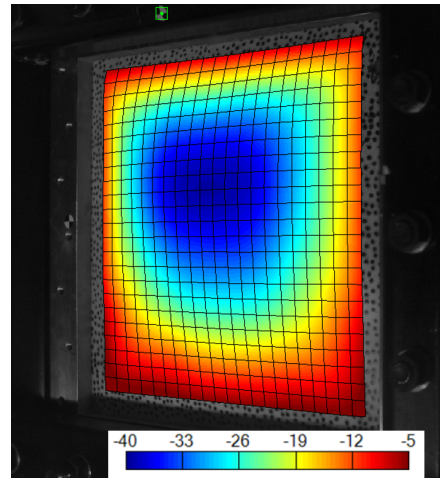
(a) Open 60% of max deflection



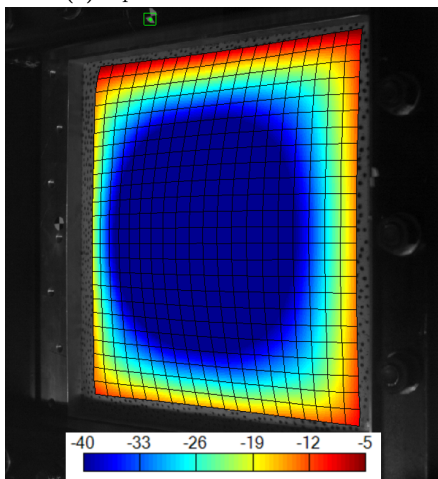
(b) Wall 60% of max deflection



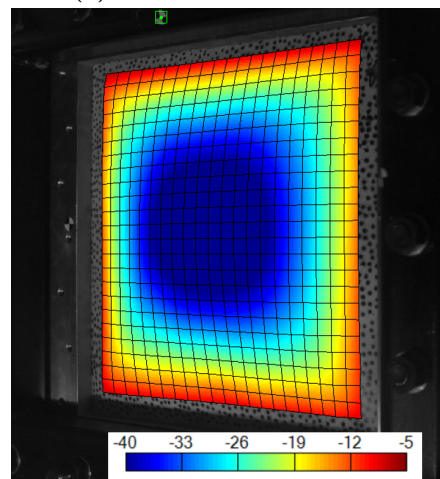
(c) Open 80% of max deflection



(d) Wall 80% of max deflection



(e) "Open" 100% of max deflection



(f) Wall 100% of max deflection

Figure 5.14: Comparison of the deformation fields of open and wall configuration at a nominal firing pressure of 60 bar. All the colour bars have equal scaling, with a range from -40 mm to -5 mm.

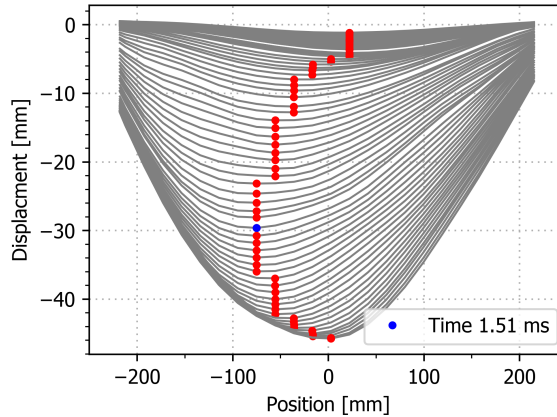


Figure 5.15: Tracking of maximum deflection point. The red dot corresponds to the location of maximum deflection for the deformation profile for the PL_W_60 test as it progresses from zero deformation (0 ms) until maximum deflection (2.16 ms).

5.5 Stiffened Panel

In the same manner as for the plate, this section will present the experimental setup for the stiffened plate, before the dynamic response is presented.

5.5.1 Experimental Setup

The aluminium 6082 T6 alloyed stiffened plate, Figure 5.16a, was mounted as illustrated in Figure 2.5d and Figure 5.16b. Double-sided adhesive tape was utilised, in an attempt to achieve simply supported boundary conditions. The tape was placed on the section of the stiffeners that was in contact with the supports. The tape was intended to barely hold the plate in place at the desired position, and then release it when the plate was hit by the load. This prove difficult. The adhesive was inconsistent and additional support was needed. Tiny wooden blocks was loosely placed under the the panels edged until the shock wave arrived, without restricting the deformation. Extruding direction was oriented vertically in the shock tube. The HAZ is to the left in all the photos in this section. As mentioned in Section 5.2.1, to track deformation with high-speed cameras for 3D-DIC, the plate section and stiffeners were manually spray-painted through a perforated template to obtain the speckle pattern. The experimental setup is further described in Section 2.5.

5.5.2 Experimental Results

The experimental results for the panel will be presented in this section. An additional nominal firing pressure test was performed on the panel. It was not included in the pre-planned test matrix in Table 4.2. The extra test was performed at a nominal firing pressure of 60 bar, with an open configuration. The decided load magnitude was based on the desire to have pressure measurements from the rigid plate configuration, as well as the desire to obtain fracture of the stiffened plate. Because of this, the only option was a nominal firing pressure of 60 bar. Based on the preliminary studies, achieving fracture was believed impossible with the wall configuration, resulting in the selection of the open configuration for the additional nominal firing pressure test on the panel.

All plots in this section are based on the measurements from Subset 3D-DIC, with the locations shown in Figure 5.17. All curves in Figure 5.18 are corrected for the rigid body movement of the setup and facility.

Positive direction is defined as upstream the shock tube. Time is set equal to zero when the shock wave arrives at Sensor 2.

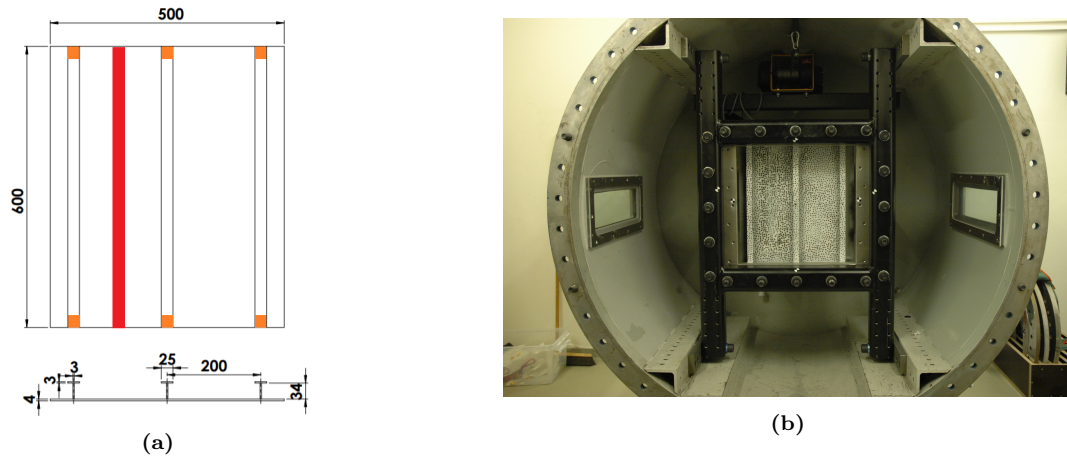


Figure 5.16: Illustration of (a) the stiffened plate dimensions, with orange markings on the stiffeners where the 50 mm long adhesive tape was placed. The red line between the stiffeners indicates the weld. The weld guide buildup lines start approximately 100 mm from either the top or the bottom - depending on the test sample. In (b), the mounting of the stiffened plate in the shock tube can be seen.

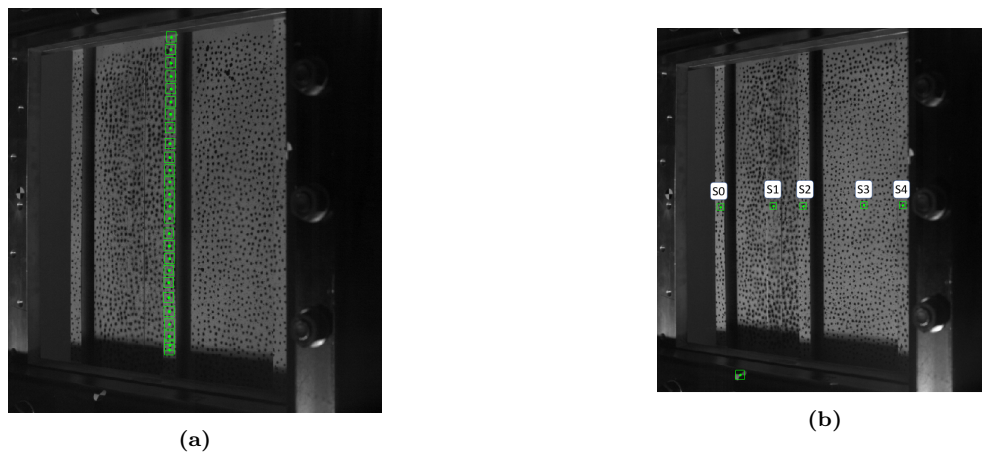


Figure 5.17: Representative illustrations of the data extraction points from Subset DIC in eCorr. (a) shows the subsets along the mid stiffener for the cross section profile deformation plots. (b) shows the extraction of the midpoints of the side stiffeners, mid stiffener and plate field, with and without weld.

In Figure 5.18, the midpoint deflection history of the mid stiffeners is shown. In Figure 5.19, the deflection history for all points - as shown in Figure 5.17b - is presented. Test PL_O_60 is not included in Figure 5.19.

It is clear that as the nominal firing pressure was increased within one driven outlet configuration - resulting in an increased intensity of the loading - the panel deflection increased. It can be observed quantitatively that all tests first exhibit a rapid increase in the inelastic displacement, before a phase of oscillations occurs. When comparing the wall configuration and the open configuration, it is evident that the wall decreases the deflection of the plate when having the same nominal firing pressure.

HAZ has a reduction in yield stress of almost 50 % compare to the rest of the panel (Section 3.5.2). Stiffened

plate are welded in engineering structures, thus the effect of HAZ is of great interest. It is observed that the plate field with the HAZ and the mid stiffener has the largest deformation in Figure 5.19. The plate field without the HAZ exhibits less deflection than the plate field with the HAZ, implying an asymmetrical response due to the HAZ. The HAZ proceeds first into the plastic zone and trigger strain localisation in the HAZ. A plastic hinge can be observed developed along the HAZ. The deformed profile of the tests can be seen in Figure 5.20. The side stiffener closest to the HAZ generally exhibits greater deformation than the side stiffener on the opposite side due to the reduction in strength at the HAZ. The wall increases the difference in the deflection between the two side stiffeners.

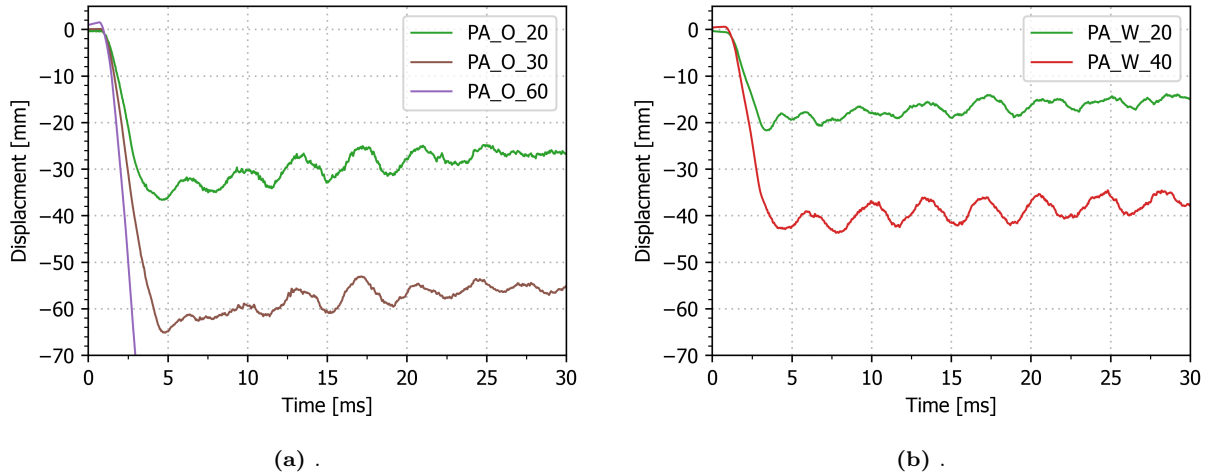


Figure 5.18: Midpoint deflection history of mid stiffener, measured with subset 3D-DIC for the panel. The curves has been corrected for rigid body (RB) movements. Data is synchronised with time zero as the shock wave passes Sensor 2

The panels oscillate with similar frequency. However, there are some differences in the amplitude depending on the location on the stiffened plate as seen in Figure 5.19. The plate field without the HAZ exhibits greater amplitude when it oscillates possibly due to the difference in strength.

In Figure 5.21, the deformation profiles of the mid stiffener are presented for all tests, excluding the test that resulted in failure (PA_O_60). The deformation profiles corresponding to the deflection at maximum deflection - 80% of max, 60% of max, 40% of max and 20% of max - are illustrated. The deflection history of each subset shown in Figure 5.17b, is exported from the 3D-DIC calculations in eCorr, along with the vertical coordinate and deflection for each frame. The data is then post-processed in a python script and plotted. In the post-processing routine, it is assumed that all subsets have the same horizontal coordinate in the photograph. The vertical coordinate is extracted from the first picture frame, thus assumed to be constant throughout the entire deformation history of the subset. One of the subsets was always located at the midpoint of the stiffeners. The location coordinate from the first frame of this subset was used as origin in Figure 5.21. As the subset DIC was used rather than the FE-based DIC, the continuity was lost between the subset elements. Therefore, several subsets along the stiffener were utilised to obtain a smoother plot. FE-based DIC could not be used, because it was impossible to obtain a mesh. The stiffener had a pixel width of 23 pixels. The mesh had to be coarse - with a pixel size greater than 23 pixels - due to the uniformity of the applied speckle pattern.

In the cross section Figure 5.21, the wall driven outlet configuration shows an asymmetrical response, with a maximum deflection found where the open side of the wall is located. A minor asymmetrical response is observed for the open driven outlet configuration. The maximum deflection of the PA_O_20 test is found to

the left, and similarly, the PA_O_30 maximum deflection is found to the right. Due to the resolution of the subset DIC, accurate location of the maximum deflection point could not be obtained. The asymmetrical response for the open configuration could be caused by the asymmetrical removal of the weld guide buildup (the red line in Figure 5.16a). The PA_O_20 test had its buildup removed from the left in the cross section plot (correlating with the top of the shock tube), and the PA_O_30 test had its buildup removed from the right in the cross section plot (correlating with the bottom of the shock tube). This was also the case for the two wall tests; PA_W_20 had removal from the right (bottom) and PA_W_40 from the left (top), but the effect was not measured because the load was asymmetrical.

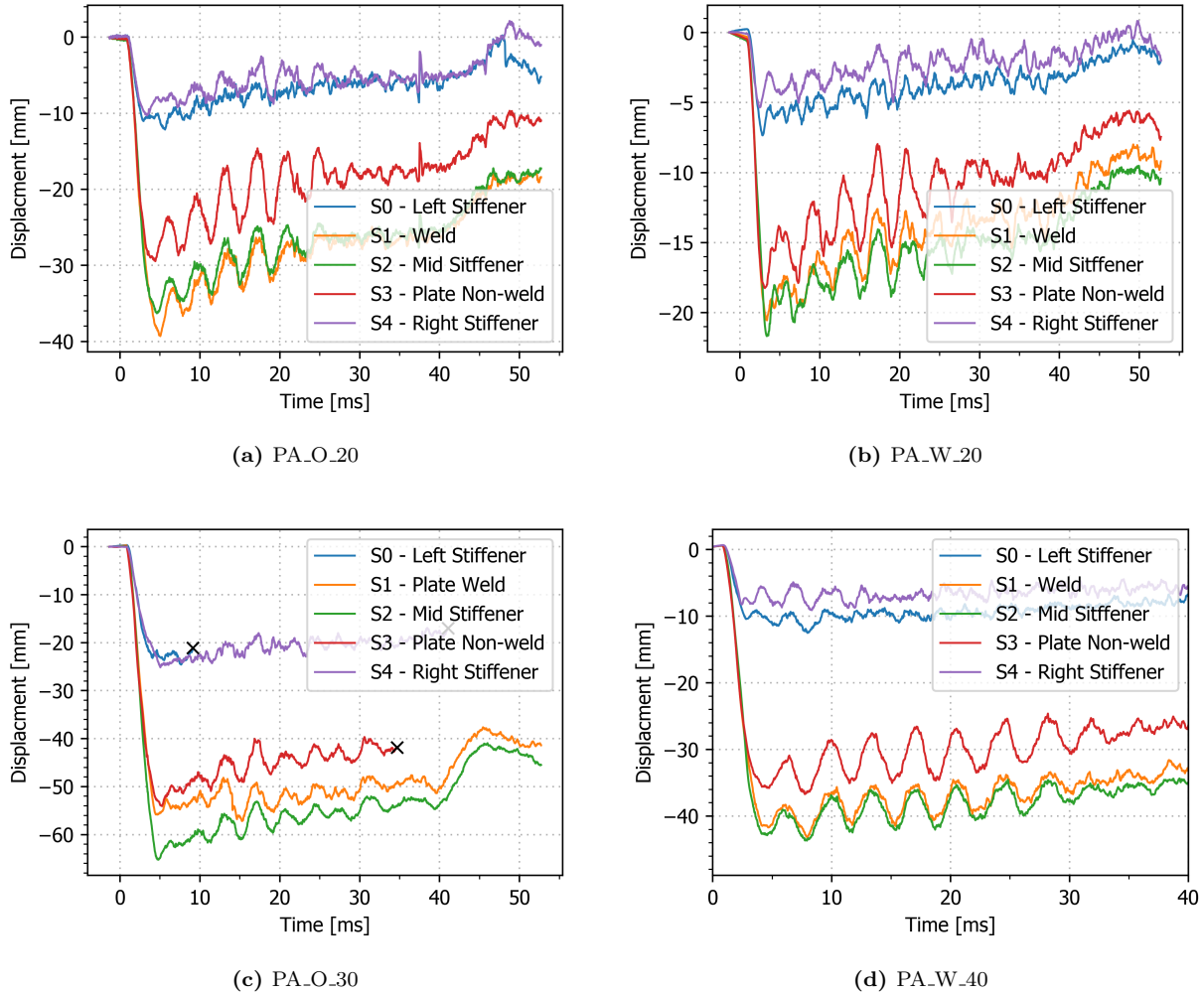


Figure 5.19: Deflection of the midpoints of five points: see Figure 5.17b measured with subset 3D-DIC. Time zero is when the shock front passes Sensor 2.

The PA_O_60 test experienced fracture. In Figure 5.22, pictures from the high-speed cameras are shown, at time 4.92 ms in (a) and time 6.57 ms in (b). The HAZ introduces a asymmetrical reduction of strength to the plate. Stiffness is reduced at the left plate field, thus less forces in the HAZ part. From the plastic strain plot in Figure 4.15 it is evident that strain localisation and plastic hinge develops in the HAZ, but this is also resulting in larger plastic strains at the right stiffener. Due to the reduction of stiffens in the left

side of the plate, the right stiffener has to carry a greater portion of the load. As the deflection progresses it is evident that the bending resistance is lost and that a plastic hinge is developed at the middle of the panel - mainly due to two failure modes - as the deflection progresses. The first to develop is the tripping of the middle and left stiffener. The mid stiffener starts to trip over its attached base plate towards the HAZ when the midpoint deflection of the mid stiffener is about 92 mm. Tripping occurs when the great tension force of the flange imposes significant compression on the web - due to the location of the plastic neutral axis - leading to instability and tripping [68]. The second to develop is the crack propagation (the red circle in Figure 5.22a), starting at the flange, moving through the web and stopping at the base plate of the right stiffener. When the two other stiffeners tripp, all load has to be carried through the right stiffener. Resulting in greater plastic strain before a crack develops at its midpoint. Because of the weld the right stiffener is able to obtained sufficient plastic strain for a crack to develop. Tearing along the base plate and mid stiffener was also observed afterwards. At the author's best knowledge this failure mode of stiffened plate has not been observed previously. The large deflection results in a reduction of the height (the vertical length) of the panel, making it smaller then the span of the support frame, and causing the panel to leave the boundary. Further Characterising of the failure processes is outside the scope of this thesis.

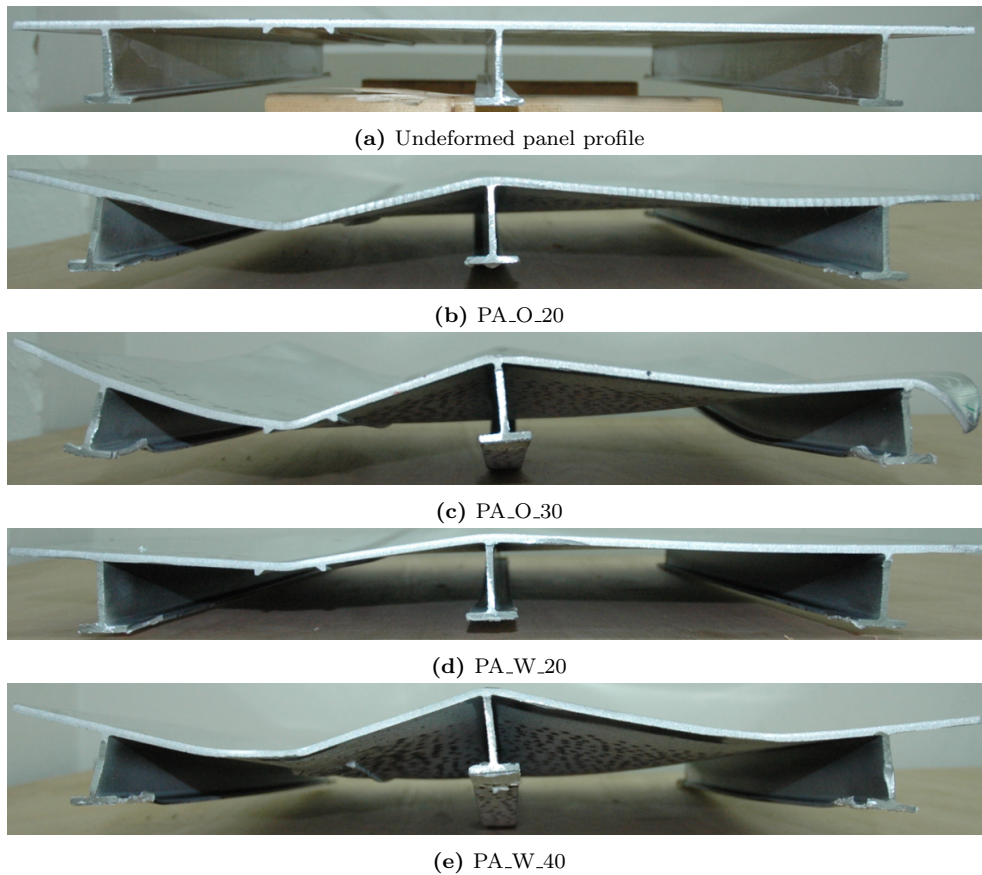
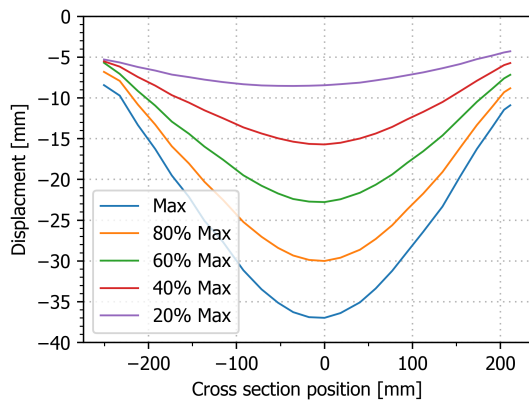
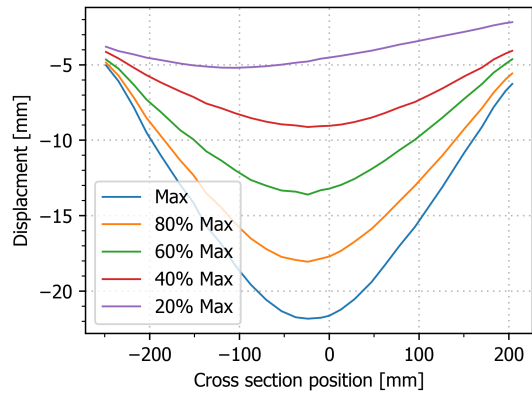


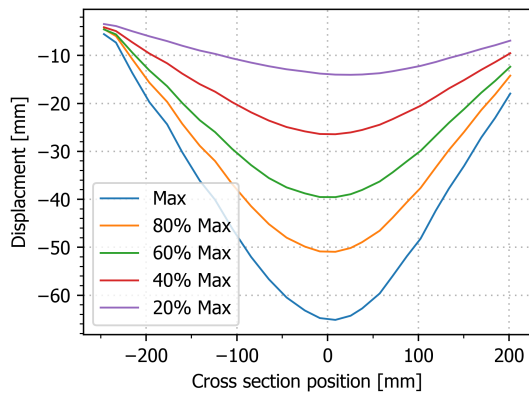
Figure 5.20: Stiffened plate profiles after the test. (a) is a undeformed profile while (b)-(e) are tests. PA_O_60 is not included. The HAZ is located on the plate field to the left. Plastic hinge are clearly developed. In (a) the weld guide rails are clearly seen.



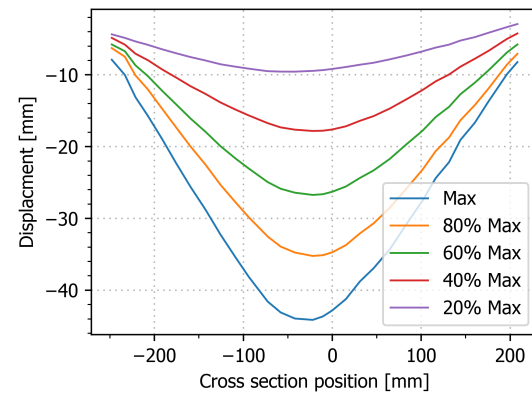
(a) PA_O_20



(b) PA_W_20

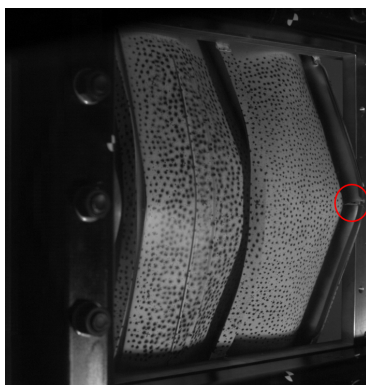


(c) PA_O_30

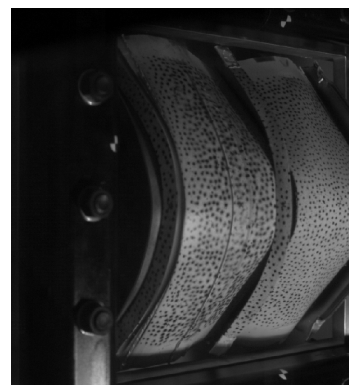


(d) PA_W_40

Figure 5.21: Deformation cross section profiles measured with FE DIC for the plates.



(a)



(b)

Figure 5.22: Test PA_O_60. (a) is at 4.92 ms. The red circle shows a developed crack at the middle of the stiffener. (b) shows the test just before it leaves the support frame, at 6.57 ms.

5.6 Concluding Remarks

Concluding remarks of this chapter are listed in this section.

- The new experimental setup for the SSTF successfully generated extreme pressure loads with varying complexity on plated structures.
- Tests on a rigid plate with piezoelectric were used to capture the spatial and temporal distribution of the extreme pressure loads. Past the first 4 ms of each test the pressure measurements were dominated by a spurious drift of negative character, leading to non-physical values. The drift was observed to vary with the load complexity, but the cause could not be determined with certainty. An attempt to correct the measurements - based on the expected negative phase from literature - was performed.
- BOS images capturing the density gradient resulting from motion of the shock wave indicate similarities to the flow field in the Eulerian simulation and large variations in the complexity between the wall and open configurations.
- Dynamic response on the deformable structures - the plate and stiffened plate - was measured with the 3D-DIC software, eCorr. FE 3D-DIC was used to capture the response of the plate, while subset 3D-DIC had to be used on the panel.
- The plate deflections were larger than predicted in Section 4. The plate exhibited large inelastic deformations and an asymmetrical dynamic response with asymmetrical loading. No failure along the supports was observed, but strain localisation around the bolt holes were.
- The stiffened plate exhibited large inelastic deformations. The HAZ and the the asymmetrical loading (wall driven outlet configuration) affected the symmetry of the response. A plastic hinge developed in the HAZ. Only the PA_O.60 test, which was intended to go to fracture, had any observed fracture.

6 Numerical Analysis

The experimental results acquired in Chapter 5 will be further studied numerically in this chapter. The experimental tests will be numerically simulated in an attempt to obtain insight into the complex dynamic problem, with focus on the loading and structural response. The numerical models in Section 4 will be further improved and studied through parametric studies. Furthermore, they will be evaluated and their capabilities will be discussed. The rigid plate tests will subsequently be numerically simulated in EUROPLEXUS (EPX) [22] with a pure CFD analysis. The deformable tests will be numerically simulated with a pure CSD analysis using ABAQUS/Explicit [23].

6.1 Introduction

Due to the complex nature of extreme pressure loads - and the limited research on the topic - the loading is the most significant uncertainty in this study. Sophisticated CFD simulations of the non-uniform extreme pressure loading event were performed in EPX. The pressure measurements from the tests on the rigid plate were meant to give the true load and validate the CFD generated loads. The measurements had significant negative drift and non-physical behaviour. Hence, even though an attempt to correct the data was done through the use of the best available literature, the measurements were not reliable.

The exposed pressure surface area was, as mentioned, divided into subareas (SA), each with an assigned temporal distribution. This approach is used in Chapter 4. As the rigid pressure wall in the CFD simulations was partitioned into subareas, the temporal distribution for each subarea could easily be extracted as the average pressure at each time step. However, the pressure readings from the rigid plate tests were limited to 16 sensor points. Therefore, an interpolation scheme had to be applied to approximate the subarea values. In Section 6.2.2, the interpolation algorithm denoted the grid data algorithm (GD) is explained and validated.

6.1.1 Naming Convention

In Table 6.1 the naming convention for the simulations of this chapter is presented. They are in addition to the naming convention presented in Section 4.6.

Table 6.1: Descriptions of the additions to the naming convention presented in Section 4.6.

Name extension	Explanation	Colour
_RAW	Raw data	Black
_NF	Numerically filtered	Sandy brown
_C	Corrected for the negative drift	Saddle brown
_EXP	Experimental	Black
_ExpL	Experimental load (NF) (GD)	Sandy brown
_ExpL_C	Experimental load (C) (GD)	Saddle brown
_CFD	Old CFD load (SA)	Dark green
_n_CFD	New CFD load (sensor points / SA)	Lime green
_n_CFD _GD	New CFD load (GD)	Royal blue

6.2 Load

The objective of this section is to obtain a better understanding of the experimental data and to verify the simulations of the fluid subdomain. To aid in this pursuit, all the rigid plate tests from the experimental programme were simulated in new numerical simulations in EPX. The same numerical model as was presented in Section 4.2.2 was utilised. However, a minor change was made in order to better represent the experiments: the discretised volume of the fluid sub domain included the whole dump tank volume. In Section 4.2.2, only the dump tank volume in front of the rigid plate was discretised. This change allowed the fluid to flow freely around the rigid plate. Pressure data in EPX was gathered at the sensor positions (Figure 5.3c) in order to enable a direct comparison to the experimental results. Pressure data was also gathered from each subarea of the rigid pressure plate for load modelling purposes.

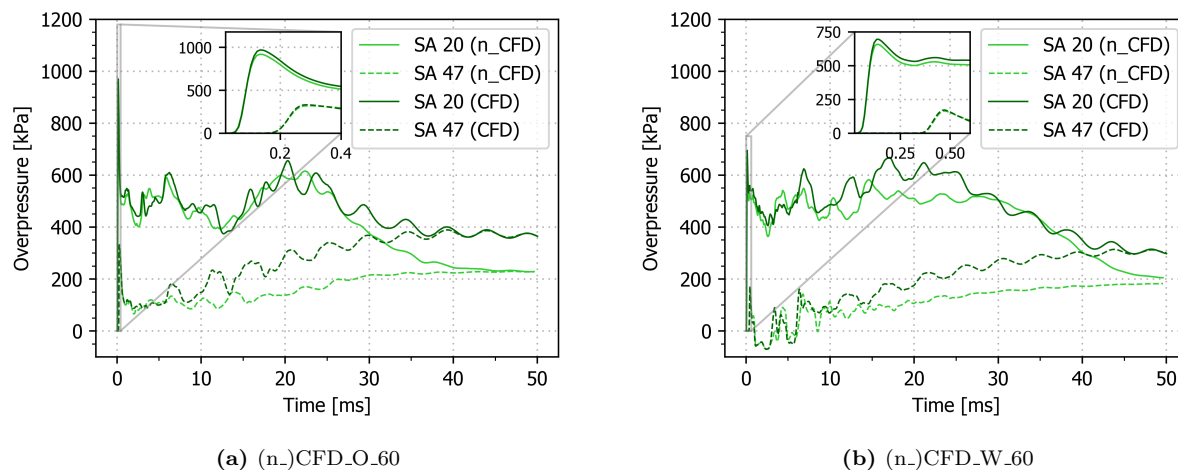


Figure 6.1: Overpressure-time histories of the subareas containing the maximal and minimal pressures for the new and the old CFD simulations of tests with both driven outlet configurations with a nominal firing pressure of 60 bar. The timescale is not comparable to the other overpressure-time histories, as Sensor 2 was not included in the subarea data sets.

6.2.1 New CFD: Resulting Loading

To assess the influence of modelling the whole dump tank in the CFD simulations, the new simulations are compared to the simulations from Section 4.4.3. This can be seen in the overpressure-time histories for distinct subareas in Figure 6.3. As the only common nominal firing pressure between the simulations is 60 bar, those simulations are displayed. However, the same trends can be seen for all nominal firing pressures. As can be observed in Figure 6.3, peak reflected overpressures are slightly higher for the simulations from Section 4.4. Most likely, that is due to different failure modes of the membranes, as the change in the tank volume should not have any effect on the peak reflected overpressures. Slight differences can be seen in the curves, but in terms of magnitudes, they are quite similar. The main difference is that the equilibrium level is lower for the new simulations. This is as expected since the volume is greater in the new simulations, while the amount of air in the blast remains constant. As there is less of a difference in the spatial and temporal pressure distributions than expected, the difference in the structural response is expected to be negligible.

Table 6.2 displays the firing conditions and blast parameters of the new CFD simulations, consistent with the representation of the experimental data in Table 5.1. The firing conditions and velocities are very similar, which is reasonable as the firing conditions used in the simulations are extracted from physical tests. Nonetheless, the maximal overpressures - both incident and peak reflected - are consistently lower for the simulations. From the overpressure-time histories in Figure 6.2 - gathered from the sensors with the maximal and minimal pressures in the simulations - it is apparent that the rise time is slower for the simulated histories. This indicates that the mesh of the fluid sub-domain in EPX was too coarse to capture the quickest changes in the physical fluid flow, which results in wider and shorter peaks. When the shock wave reaches PC_16, it has slowed down significantly, and the fluid mesh is better able to represent the physical behaviour. For the open simulation, the PC_01 measurements are seen to underestimate the peak pressure, but the impulse is similar to the experimental measurements the first 4 ms. For the wall simulation, both the impulse and the peak pressure are underestimated at PC_02, while the impulse is overestimated for PC_01 (not displayed). This indicates that the simulations with the wall configuration are less asymmetric than the experiments.

Due to the corrupted physical measurements, validating the CFD analysis past 4 ms is impossible. However, the simulated pressure values generally deviates less than 5% from the experimental values in this domain when the peaks are excluded. Increasing the nominal firing pressure seems to make the deviations larger - especially for the wall configuration - but the results remain similar. This might indicate that the simulations are more mesh sensitive at higher nominal firing pressures, as velocities increase. The corrected experimental measurements generally show better agreement with the CFD, but that is to be expected as the uncorrected measurements are physically impossible.

Table 6.2: The firing parameters, blast parameters and peak reflected overpressures from the new CFD simulations.

Test	Firing conditions			Parameters driven Sensor 2		Parameters rigid plate PC_01 PC_02	
	p_{driver} [kPa]	$p_{ambient}$ [kPa]	$T_{ambient}$ [°C]	M_s []	$p_{so,max}$ [kPa]	$p_{r,max}$ [kPa]	$p_{r,max}$ [kPa]
n_CFD_O_20	2160.7	101.3	21.4	1.71	258.8	672.9	475.8
n_CFD_O_30	3117.7	101.3	22.7	1.83	333.1	758.1	534.7
n_CFD_O_60	6211.1	100.9	23.9	2.06	382.6	1173.6	819.6
n_CFD_W_20	2160.7	101.3	21.4	1.71	258.8	362.6	385.0
n_CFD_W_40	3812.8	101.2	23.4	1.97	343.0	538.4	579.3
n_CFD_W_60	6211.1	100.9	23.9	2.06	382.6	627.4	679.7

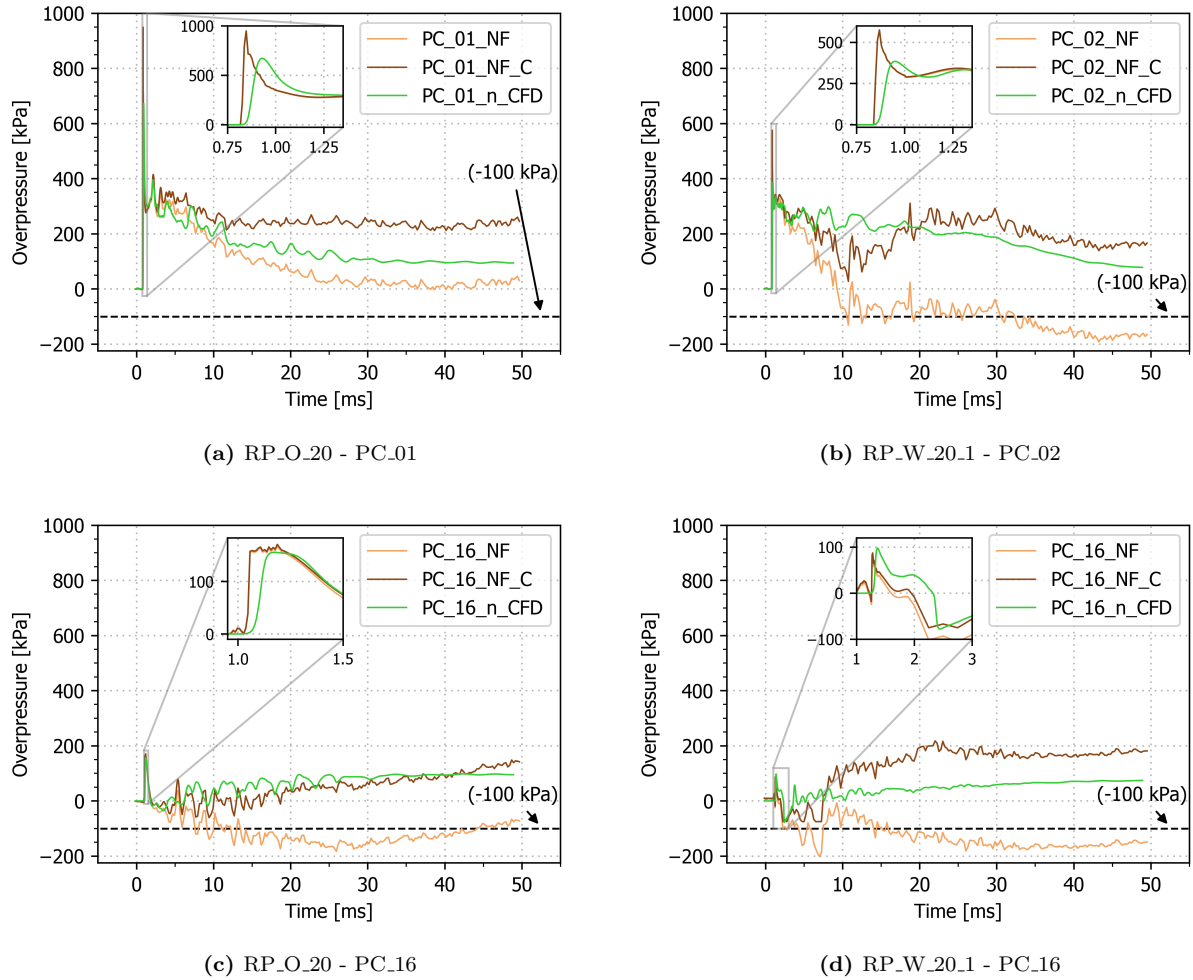


Figure 6.2: Overpressure-time histories from the sensor containing the global maximal pressure ((a)-(b)) and the sensor expected to contain the global physical minimum ((c)-(d)) for tests / CFD simulations with a nominal firing pressure of 20 bar for both driven outlet configurations.

6.2.2 The Griddata-algorithm

In traditional blast-resistant design, experimental tests on rigid plates with pressure sensors are conducted to ensure that the spatial distribution of the load is close to uniform. If the tests are successful, the load is easy to model, and if the tests show too much non-uniformity, the test setup is reevaluated. In this study, the non-uniform loading was a prerequisite, which makes the modelling of the loading more cumbersome. In CFD simulations, data can be gathered at any given point, which enables convenient load modelling like the subarea approach explained in Section 4. In physical testing, data gathering capabilities are always limited, hence, other methods must be found. In this study, the subarea approach was utilised for the experimental loads as well, which required interpolated sensor data over the plate. To achieve this, the unstructured data interpolation algorithm `interpolate.griddata` [69] from the Python-based open-source software collection Scipy was applied. The algorithm is henceforth referred to as the griddata-algorithm.

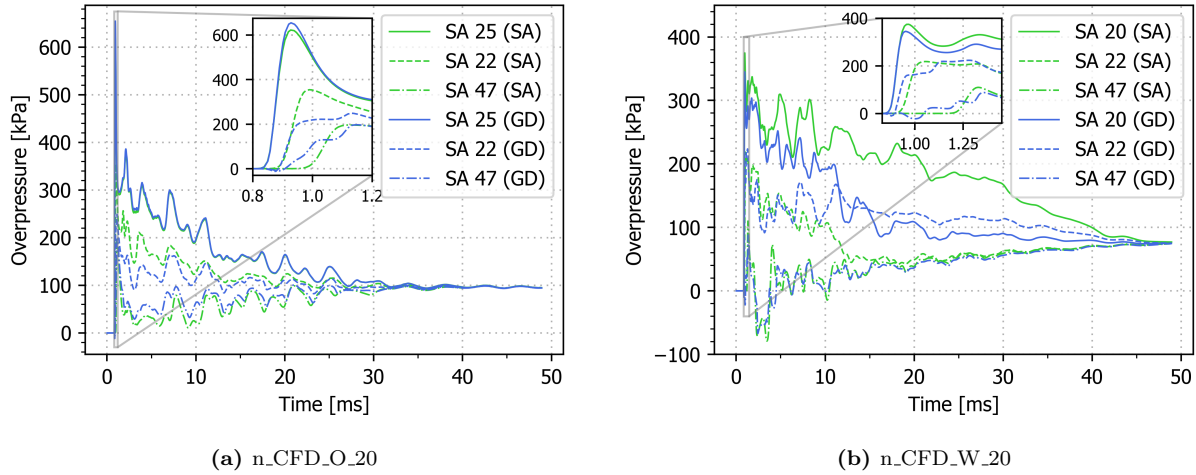


Figure 6.3: Overpressure-time histories of the subareas containing the maximal and minimal pressure values for the new CFD simulations with a nominal firing pressure of 20 bar and both the (a) open and (b) wall configuration. Both exact (SA) and approximated (GD) pressure values are displayed.

In order to assess the efficacy of the griddata-algorithm, the result of applying the algorithm to the "sensor measurements" from the new CFD simulations was compared to the values measured in the subareas in the same simulations. The resulting overpressure-time histories are displayed in Figure 6.3 for the subareas with the maximal and minimal pressure measurements, in addition to a subarea with median pressure levels. The numeration and positioning of the subareas and sensors are shown in Figure 4.3b and Figure 5.3c, respectively. SA 20 is close to the centre - but there is no sensor in its exact position - and SA 47 is along the outside of the plate where the density of sensors is the lowest. SA 22 is positioned between PC_12 and PC_13, but in the longitudinal direction, there are no nearby sensors. SA 25, on the other hand, is surrounded by sensors. As suspected, SA 25 shows good agreement between the true value and the interpolated value, but both the local minima and maxima are slightly overestimated. This is most likely because PC_01 in reality has larger pressures than the surrounding subareas, and because too few data points have been given to the griddata-algorithm to sufficiently counteract this fact. From the oscillating rise to peak pressure in SA 47, it is apparent that the algorithm is less accurate when there are large differences between the data points. Due to small magnitudes and timeframe, this is most likely insignificant for the structural response. Otherwise, the interpolated SA 47 estimate the correct value quite well for both configurations. For the open configuration, the shape of the curve is almost correct, but the magnitude is slightly overestimated. For the wall configuration, some local maxima and minima are not replicated by the interpolated history, but the overall magnitude fits well. The peak pressure of SA 22 can be seen to be greatly underestimated by the interpolated value for the open configuration. The shape of the curve is correct, but the magnitudes are underestimated until equilibrium is reached. The approximated SA 22 is quite accurate for the first 5 ms for the wall configuration, but past that point, the magnitude is overestimated and large oscillations occur. The overpressure-time history for SA 20 for the wall configuration shows the importance of having a sensor in the position where the maximal pressure occurs; All its pressure values are underestimated, some in the order of 50 % of the correct value. Figure 6.4b shows that the value at SA 20 is estimated to be lower than the values for SA 15 and SA 25 at peak reflected overpressure. This is a correlation which holds for the entirety of the overpressure-time history (not displayed). If a sensor had been placed in that position, the correlation would have been reversed, and the pressure values would have been more accurate.

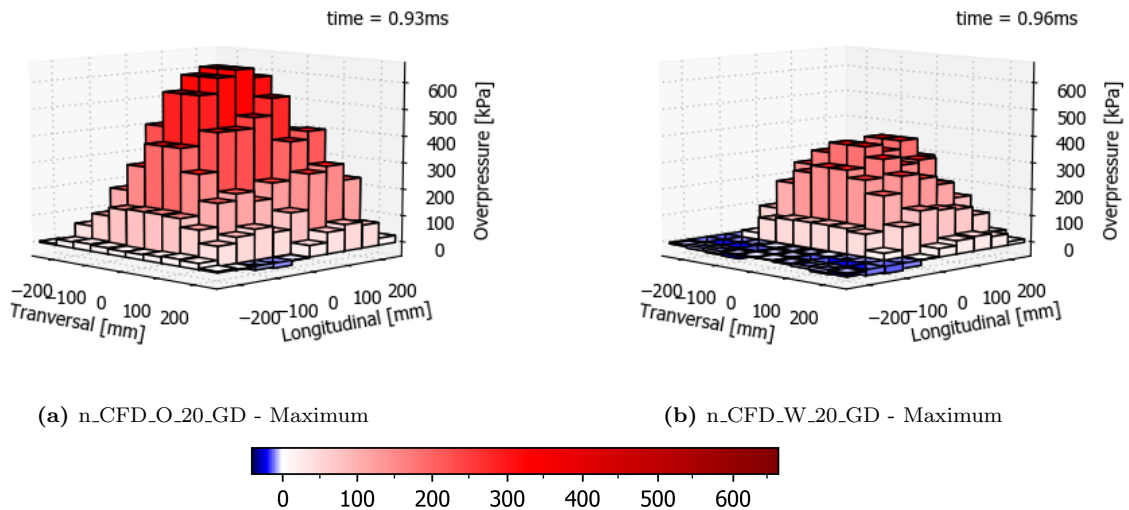


Figure 6.4: Visualisation of the pressure distributions at the maximum for the new CFD simulations with the open and wall configurations and a nominal firing pressure of 20 bar. Pressure data gathered from the "sensor measurements" and interpolated over the plate surface by the griddata-algorithm.

In Figure 6.4, the pressure distribution at the maximum is visualised for the approximate values produced by the griddata-algorithm for both simulations conducted with a nominal firing pressure of 20 bar. The true shapes of the pressure distributions are exactly the same as in Figure 4.7. Hence, they are not repeated here. In Figure 6.4a, it is interesting to note that the distribution has lost its symmetry. The subareas are mirrored about the longitudinal axis, and they are therefore symmetric. About the transversal axis, however, there are large differences. The values are also larger along the transversal axis than along the longitudinal axis. The distribution of the wall configuration, seen in Figure 6.4b, is more similar to the actual distribution. Both the approximated distributions are less concentrated around the maximal values than the correct distributions, which likely will lead to larger impulses. These discrepancies will probably influence the structural responses.

To sum it up, the griddata-algorithm is a convenient way to distribute the pressure measurements from the sensors across the whole plate. From Figure 6.3 and Figure 6.4, it is apparent that the performance of the griddata-algorithm is highly dependent on the sensor placement and density. However, some values are overestimated while others are underestimated, so the load impulse will likely be close to the correct value. The shape of the curves are very similar to each other for the open configuration, and less so for the wall configuration. As the shape of the pressure distributions are somewhat altered, the structural responses might be affected.

6.3 Blast Loaded Plate

The plate was intended to be a deformable structure consistent with the previous work performed at SIMLab at NTNU. From a structural engineering point of view, the response of the plate structure is regarded as well-known. The motivation to include the plate was to establish an understanding of the complex non-uniform loading on a simple well-known structure. The investigation of the numerical structural responses and the experimental results indicates that the plate is more sensitive to the pressure history than the stiffened panel.

6.3.1 Numerical FE Model

During the testing of deformable plates, severe straining was observed around the bolt holes - especially around the bolt holes close to the middle of the plate. Due to the large inelastic deformation of the thin plate, bending resistance was lost, and the load was absorbed by the bolts through membrane forces. The straining around the bolt holes was observed to increase with increasing mid-point deflection. Therefore, only using fixed boundaries is regarded as inadequate, as it would yield too stiff boundary conditions. Hence, the actual clamped boundary conditions of the plate had to be modelled in its entirety, with bolts and clamping frame.

The numerical model developed in ABAQUS/Explicit in Section 4.3.1 is adopted and updated to include the complex boundary conditions. In Figure 6.5, the numerical assembly is illustrated. The model consists of a back frame, the test specimen, a front frame, and bolts.

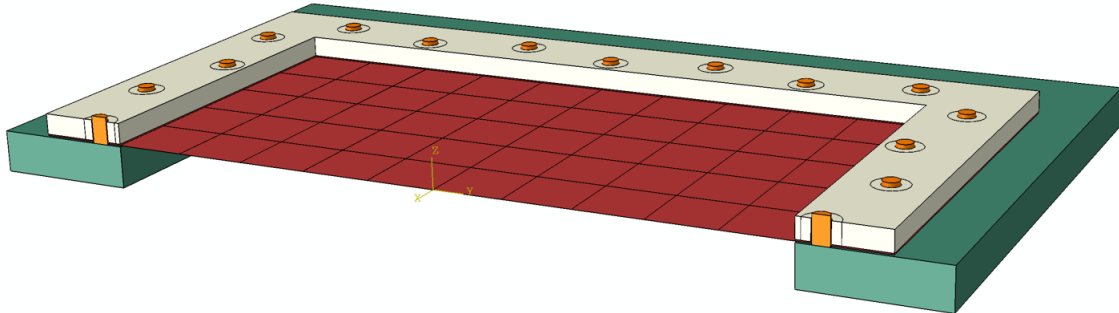


Figure 6.5: Numerical modelling of the plate with clamping frames. The model consists of a back frame (green) with tie constraints to bolts (orange), the test specimen (red), and a front frame (white). Furthermore, the figure shows the 50 partitioned subareas where the load is assigned.

The clamping frames and bolts were discretised using eight-node brick elements with reduced integration (C3D8R). The clamping frames were modelled using aluminium and the bolts using steel - both with elastic behaviour. The bottom clamping frame was assumed fixed in all translations. As the numerical model consists of multiple interacting components, the contact algorithm explained in Section 4.3.2 had to be applied. To reduce the work of the contact algorithm, the contact domain was refined by providing the algorithm with specific surface pairs. The same surface interaction model was assigned to all the specified regions in the general contact domain.

As previously stated, friction is an essential part of the contact algorithm, but the friction coefficient is a parameter with great uncertainty. At this stage, the frictional coefficients - both the static and dynamic - were set to be the same. For this study, a frictional coefficient of 0.3 from the literature [70] was used. A sensitivity study of the frictional coefficient was conducted, and as anticipated, the midpoint deflection was influenced.

For simplicity, the bolts are inspired by - and modelled as in - [24] and [71]. The bolts and the bottom frame are modelled as one component (using a tie constraint to connect the bolts to the back frame) because of the internal female threads in the bottom frame. Bolt heads are excluded. An area corresponding to a bolt head was partitioned on the top frame, where a bolt head pressure is assigned. The pressure results in a clamping force between the frames and the plate. The bolt torque was estimated in the experiments but with uncertainties. The uncertainty of the resulting pretension force is further increased by other factors such as the friction and geometry of the threads. By modelling the bolts as stress-free in the model, it is not possible to replicate the varying tension force in the bolts as the loading event progresses. Alternative modelling methods for the bolt mechanism is regarded as future work. However, this method is considered sufficient for validating and interpreting the load. Parametric study of bolt head pressure were conducted in

order to investigate the sensitivity for completeness. It is listed in the appendixes. A conservative pretension force of 23 kN was used in this section.

Artificial energy as a ratio of internal energy was below 3 % for all conducted simulations. Conservation of energy was also evaluated for all tests. There were few signs of energy losses in the model. The total energy divided on internal and kinematic energy was below 0.06 % for all simulations. Energy plots are included in the appendixes.

6.3.2 Load Evaluation

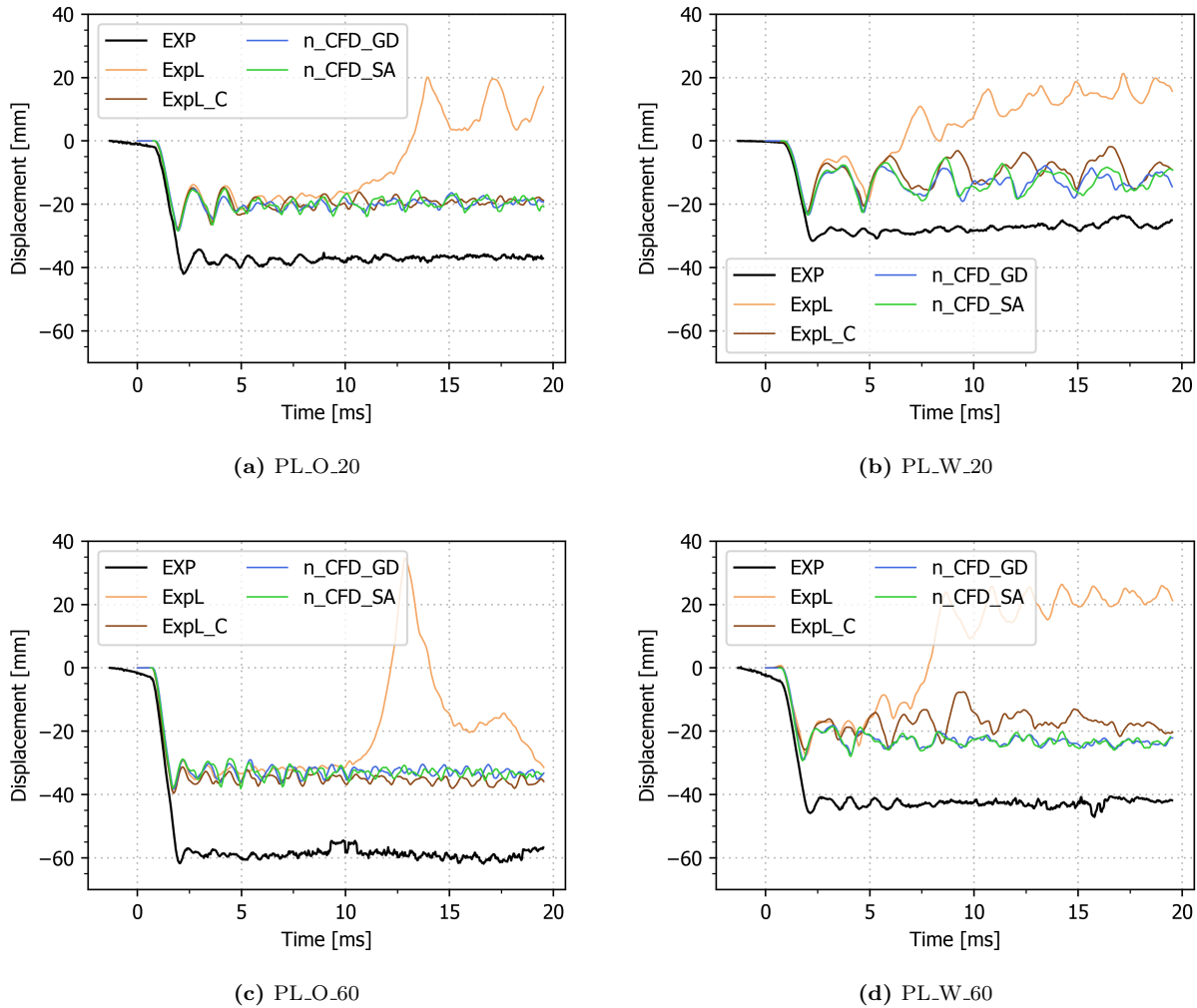


Figure 6.6: Midpoint deflection of the plate resulting from the loads described in Section 6.2.

Load validation and evaluation with regard to the structural response of the plate will be performed. This is in an attempt to investigate if the loading is correctly interpreted on the plate before applying them to the stiffened panel. In Figure 6.6, the midpoint deflection history resulting from the loads described in Section 6.2 is presented.

The first 5 ms of the numerical responses are similar, but past that, the non-corrected experimental loading

yields upstream deflections due to the measured negative spurious drift. The corrected experimental loading yields better results, especially for the open configuration. However, the CFD loads clearly yield the best correspondence with the experimental data. For the CFD loads, both the loading approximated with the griddata-algorithm and the subarea loading yield similar structural responses. Even with the CFD loading, the midpoint deflections are greatly underestimated for all the plate tests. One plausible explanation is that the load is not captured correctly. As previously mentioned, the plate is sensitive to the load history. Differences in the applied load compared to the true load in the experiments will greatly affect the dynamic response of the plate. There are uncertainties with regard to the load due to faulty measurements and limitations in the numerical description of the fluid subdomain. The simple and convenient method of applying the load using subareas - where the extreme pressure load is averaged within each cell - is a discretisation of the load and not a true representation. Hence, the method should be further tested, especially regarding cell size sensitivity. Another explanation is the boundary condition modelling. The whole rig - not just the clamping frame - should be included in the numerical analysis of the plate. When the plate has large inelastic deformations, large membrane forces develop. These forces are exerted on the rig frame, which may lead to a substantial elastic deflection of the fixture. The stiffened panel tests will only be simulated with the CFD loads, using both the griddata-algorithm and subareas.

FSI effects can greatly change the spatial and temporal distribution of the pressure load when large deformations occur, and they should be further investigated. However, when comparing an uncoupled approach to a coupled approach for the modelling of blast events with assumed uniform loading - as done by Aune et al. [72] - the uncoupled approach gives conservative results for higher blast pressures on metallic plates. At lower blast pressures, the agreement between the uncoupled and coupled approach was discovered to be better. Although the current load are not a blast load, it is suggested to perform the tests at lower nominal firing pressures in further work.

6.4 Blast Loaded Stiffened Panel

This study is the first to test stiffened panels in the SSTF. It is a more complex structure than a simple plate, both because of the HAZ and the stiffeners. Hence, it should - in theory - have a more complex structural response to the same load. As the loading conditions are both complex and uncertain in this study, the plate was used to obtain a general understanding of the load modelling. As the experimental data (both NF and C) were determined to be non-physical or unreliable, only the CFD loads are used in the following section.

6.4.1 Numerical FE Model

In the experimental phase, the stiffened panel deformations were mostly as predicted by the numerical simulations in Chapter 4, both in magnitude and shape. These results indicate that the FE model represents both the panel and its boundary conditions reasonably well. Hence, the same numerical model is used in this section.

6.4.2 Simulations

Figure 6.7 displays the midpoint deflections of all three flanges and the two plate fields for the simulations of the tests at a nominal firing pressure of 20 bar, with both the GD and the SA loading. The simulations of the tests with the wall configuration are close to identical, while there are some interesting differences for the simulations with the open configuration. The midpoint deflections of the weld and the middle stiffener are clearly greater for the GD simulation, while the right and left stiffeners have greater midpoint deflections for the SA simulation. This is likely due to the asymmetric pressure distribution around the peak pressure for the open configuration with the GD load, discussed in Section 6.2.2. As the pressure magnitudes are greater along the longitudinal axis, it is logical that the deflection along that line is overestimated. The same trend was seen at higher nominal firing pressures for both simulations. The influence of the distribution around the peak pressure further emphasises the differences in the load regime between the plate and the stiffened panel - presented in Section 4.5.1 - as this behaviour was not apparent in the plate simulations.

In Figure 6.8, the deflection histories of the midpoint of the middle flange are shown both for the FE model subjected to the new CFD loads and the corresponding test. Excluding the PA_O_30 test, all the panel simulations yielded too stiff responses. As the friction coefficient used in the simulations was conservative, the responses should have been even stiffer. Additionally to the load- and FSI-related issues discussed in Section 6.3.2, assuming isothermal conditions may contribute to the stiffness overvaluation. Assuming negligible adiabatic effects is likely a poor assumption for the panel due to the strain localisation. The asymmetric effects of the HAZ seem to be underestimated, as the relative deflection of the left flange and right plate field midpoints are under- and overestimated, respectively, for all simulations in Figure 6.9. This indicates that the right side of the panel absorbs some of the load absorbed by the left stiffener in the experiments. Both FSI effects and asymmetrical material properties due to strain softening could cause these changes in the structural responses. The experimental deflections are seen to converge towards the simulated deflections, but the reason for this convergence is likely a quicker relaxing of the panel as the air is free to leave the tank in the experiment - unlike the CFD simulations - alleviating the pressure.

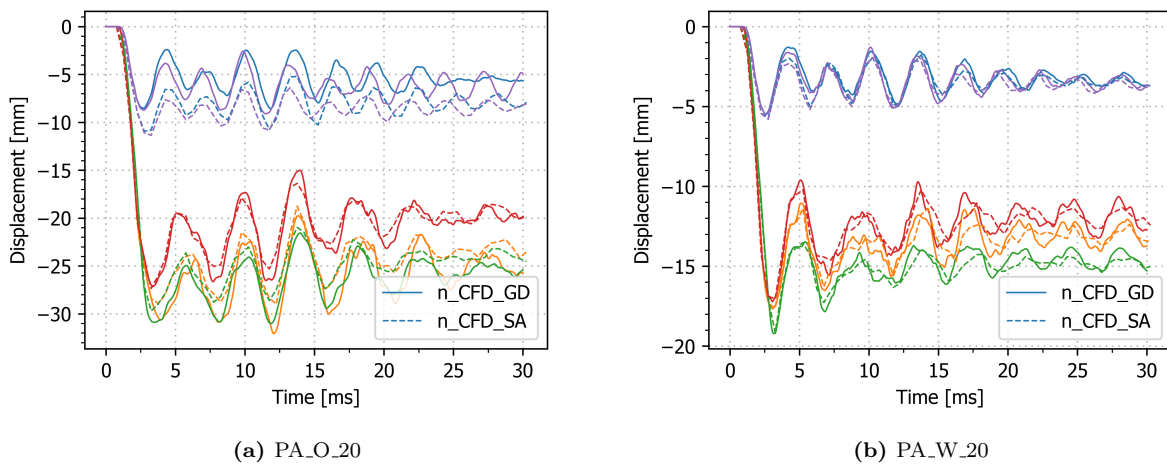


Figure 6.7: Deflection histories of the midpoints of five sections (see Figure 5.17b and Figure 5.19) from the numerical simulations with CFD loads, both GD and SA. Colour coding: Blue = Left stiffener, Orange = Weld, Green = Middle stiffener, Red = Unwelded plate field, Purple = Right stiffener.

All Lagrangian models, both panel and plate, were modelled using standard structural modelling techniques, and material assumptions were made. The materials were assumed to be strain rate and temperature independent. Rate dependent inelastic behaviour, viscoplasticity, was not included in either of the structural models. This is due to the low strain rate sensitivity of 6082-T6 aluminium discovered by Chen et al. [59]. Previous measurements on metallic plates subjected to shock waves in the SSTF showed intermediate strain rates [53]. However, as mentioned above, due to the weld on the stiffened panel, strain localisation occurs in the HAZ due to the reduction of the yield stress. The reduction was discovered to be around 45 % in Section 3.5.2. The HAZ experiences higher strain rates and rapid plastic deformation. Heating generated due to the rapid increase in plasticity may result in thermal softening. Adiabatic heating should be included in the material model. For large deflections, strain localisation also occurs around the stiffener midpoints. This was not investigated and could explain the systematic stiff response of the stiffened panel. Including strain rate and thermal softening effects in the material model may alter the structural response. Relative deformation between the different segments of the panel will increase. Future work should include viscoplasticity.

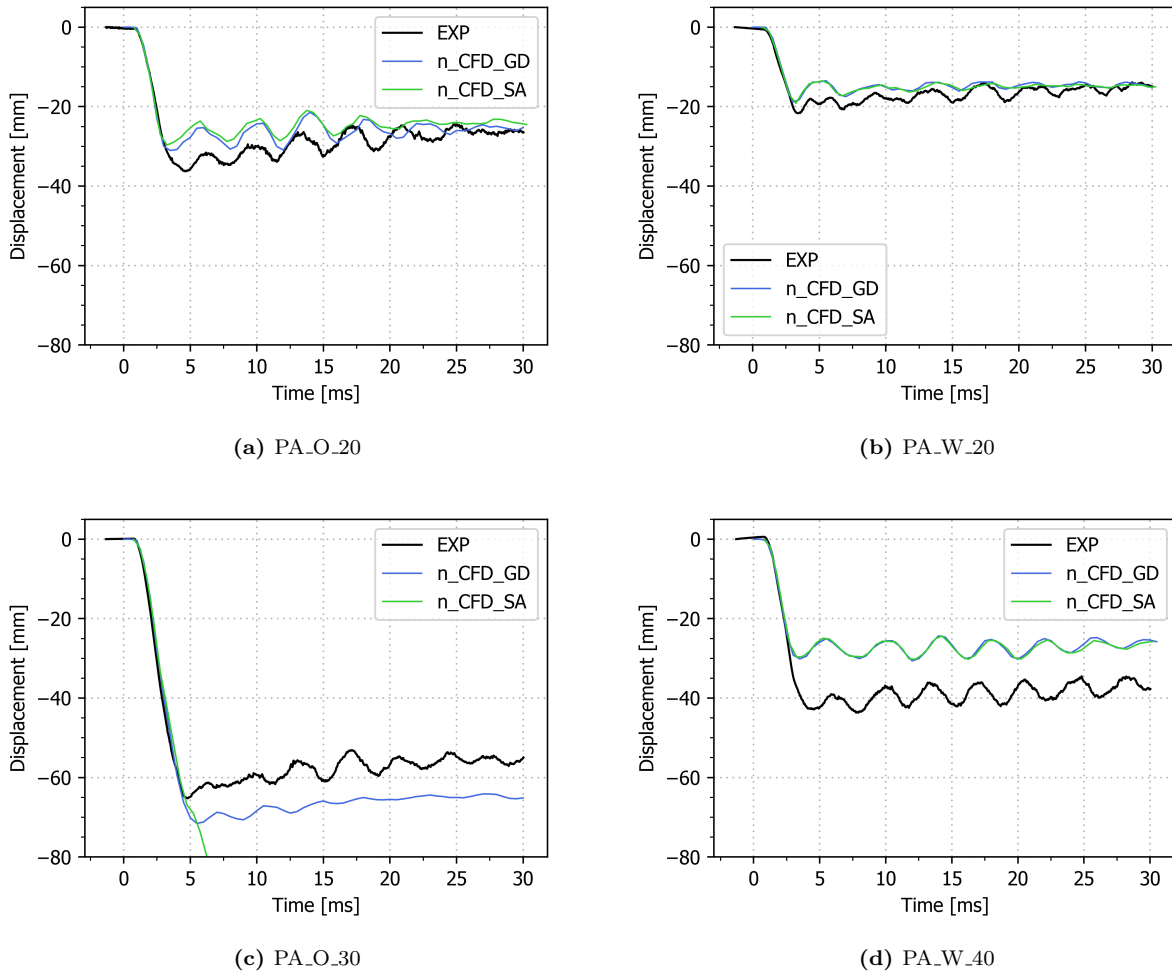


Figure 6.8: Deflection of the middle flange midpoint of the panel subjected to the new CFD loads described in Section 6.2.

The numerical simulation of the PA_O_30 test stands out as the only test in Figure 6.8 where the peak deflection of the middle flange is overestimated. The GD simulation has an incorrect deformation mode due to the previously discussed concentration along the longitudinal axis. This is apparent from Figure 6.9c, as the deflections of both the right and left flanges are greatly underestimated. The simulation with the SA load fractures and its deflection tends to infinity. There are four factors that likely contribute to this. First, the Cockcroft-Latham parameter is too low. Second, the friction coefficient used in this study is conservative. Third, there is a contact thickness reduction of the shell elements. Fourth, there are FSI effects. Regarding the first possible contribution, the fracture parameter is obvious, as an underestimated value would lead to premature fracture. As is soon to be discussed, the simulations of the PA_O_60 test also indicate that the fracture parameter is too low. Regarding the second possible contribution, only friction can activate membrane forces, since the panel is simply supported. Without the membrane forces, only bending moments restrict the deformation. Additional simulations were executed to investigate the influence of the friction coefficient - both for this test and the others - and the panel did not fracture with high friction coefficients for aluminium-aluminium contact (0.1 - 0.7) [55]. These studies are included in the appendixes. Regarding the third possible contribution, the contact thickness reduction of the shell elements might affect

the interaction between the supports and the panel. This could lead to the part of the stiffeners lying on the supports deforming less than in the experiments, thus absorbing less of the load. In addition, the deformation could potentially increase the friction between the supports and the panel. Regarding the fourth possible contribution, the FSI effects increase with deflections - and there are considerable deflections in this test. The FSI effects would likely concentrate the load towards the centre of the plate, and as the right stiffener fractures first in the simulation, this would likely delay the fracture; especially considering that fracture does not occur for the GD simulation, which has higher load concentration along the centre line.

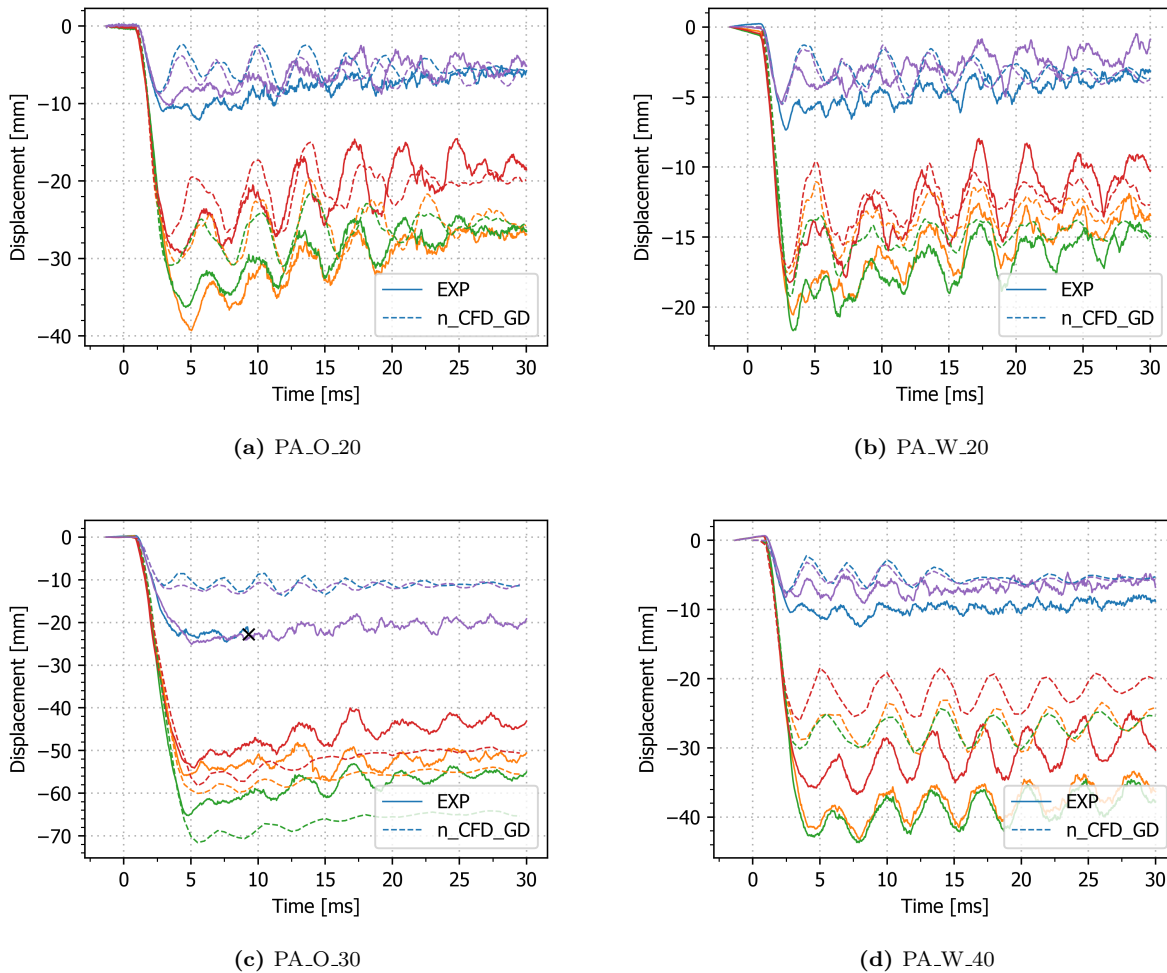


Figure 6.9: Deflection histories of the midpoints of five sections (see Figure 5.17b and Figure 5.19) from the experiments and numerical simulations with CFD loads (GD). Colour coding: Blue = Left stiffener, Orange = Weld, Green = Middle stiffener, Red = Right plate field, Purple = Right stiffener.

The numerical simulations of the PA_W_40 test yielded mostly the same results as the 20 bar simulations compared to the experiment with regard to midpoint deflections and oscillations. The exception was the more severe underestimation. Both the numerical simulations predicted a maximal deflection of the middle flange smaller than 75% of the experimental deflection. The fact that the compliance between simulations and tests are better at lower nominal firing pressures - especially considering that the experimental maximal deflections are similar between the PA_O_20 and PA_W_40 - may indicate that the load modelling is the

main problem. As previously stated, the agreement between the initial sensor measurements and the CFD data lessen with increasing nominal firing pressures.

Due to the plastic deformation of the supports being registered in the tests, simulations with elastic perfectly plastic behaviour of the supports and a characteristic element length of 5 mm were conducted. Although the plastic deformation of the simulated supports were similar to the experimental deformation, the deflection of the panel was unaffected. The study is included in the appendixes.

In Figure 6.10a, the displacement-time history for the PA_O_60 test, as well as the simulations of it, are displayed. For this test, two simulations with SA-extracted loading are shown; one with a fracture criterion and one without. The two simulations have different failure modes, but the displacement histories are similar. The experimental midpoint velocity is significantly larger past 2 ms, reasons of which could be strain softening due to higher strain rates, increased FSI effects due to larger deflections, or larger errors in the load modelling due to a higher nominal firing pressure.

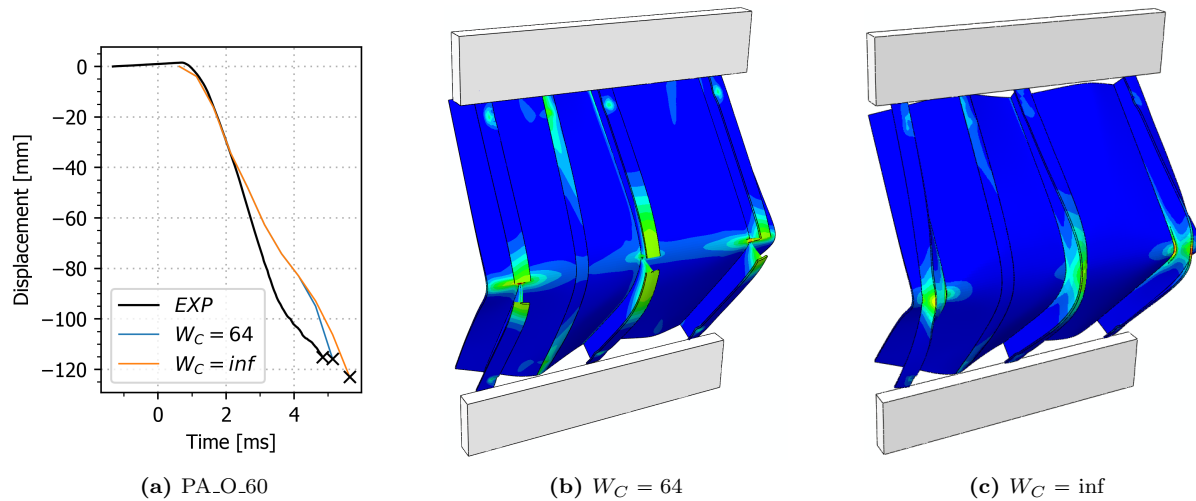


Figure 6.10: (a) Displacement-time history from the PA_O_60 experiment, as well as two simulations with n.CFD-SA loading and different fracture criteria. (b) Failure mode with the fracture criterion determined by Morin et al. [1]. (c) Failure mode without a fracture criterion.

Characterising the fracture behaviour of stiffened aluminium panels subjected to extreme pressure loading is outside the scope of this thesis. However, it is interesting to note that all the stiffeners fracture when the PA_O_60 test is simulated with the standard model, while all the stiffeners fail by tripping when the failure criterion is excluded from the material model. Hence, the Cockcroft-Latham parameter of the stiffeners must be slightly increased - to avoid fracture in the left and middle stiffeners - if the experimental failure mode is to be replicated numerically. The numerical failure modes are displayed in Figure 6.10, while the experimental failure mode is displayed in Figure 5.22.

6.5 Concluding Remarks

Concluding remarks of this chapter are listed in this section.

- The CFD simulations were unable to capture the rise time and the peak magnitude of the extreme pressure load. This was likely due to the mesh of the fluid subdomain being too coarse. Hence, further investigation will be proposed.
- The griddata-algorithm is a convenient way to distribute pressure sensor readings across the whole plate. However, the accuracy is greatly influenced by the sensor density over the exposed pressure

area.

- The CSD plate model from 4.3 severely underestimated the experimental deflections, and therefore, the clamping frame and bolts were included in the model. The new model yielded an improvement but not a satisfactory correspondence with the test results. Suspected reasons for this are the coupled behaviour to the rig frame or the sensitivity to the load history.
- Two CFD-generated loads and two experimental loads - both corrected and non-corrected - were applied to the CSD model of the plate. All loads resulted in similar results for the first 5 ms. Past that point, the non-corrected experimental load resulted in upstream deflections. The CFD loads yielded better correspondence to the test results.
- The CFD loads - one being exact and the other an approximation based on the griddata-algorithm - yielded near identical responses for the plate. For the panel simulations with open configuration, however, different deformation shapes were observed. This is likely due to the panel response being heavily dependent on the peak pressure, where the griddata-algorithm was observed to alter the distribution.
- The peak deflection, the new equilibrium position and the oscillations of the tests are all well predicted by the panel model for the tests with a nominal firing pressure of 20 bar. Close to fracture and at a higher nominal firing pressure, the accuracy of the predictions worsen.
- The greatest uncertainty of the plate is the boundary condition modelling, and because of that, it is reasonable for the panel to yield better results. The panel is simply supported, hence, the forces and moments transferred to the rig frame - excluding the forces in the load direction - are minimal. This will mainly lead to rigid body motions of the panel, which are accounted for and removed in the DIC analysis. Thus, there is minimal uncertainty in the boundary condition modelling of the panel.
- The inclusion of a viscoplastic material model in the numerical model of the panel is proposed.
- The tripping and fracturing, which were the experimental failure modes of the panel, are successfully replicated numerically.

7 Conclusions and Outlook

In this section the main topics of the study are summarised and discussed. In addition the most important findings are emphasised. The thesis is concluded with recommended future work.

7.1 Summary and Discussion

The objective of this study was to determine how plated aluminium structures behave under extreme pressure loading, and to establish a convenient method to model the loading conditions. In this endeavour an experimental setup for the SIMLab Shock Tube Facility was designed. The setup was modular to enable the testing of both simple plates and stiffened panels with varying load complexities. A numerical framework for the modelling of structural responses to extreme pressure loading was established and used to construct a test matrix. The test matrix was executed, both physically and computationally, and the results were used to assess the performance of the numerical framework.

Through evaluation of traditional experimental setups and suitable boundary conditions, and conducting simple preliminary simulations, an experimental setup was determined and designed. A computer 3D model of the setup was created, and iterations on the design were performed. The setup accommodates for the use of load cells to measure reaction forces, however, load cells were not utilised in this thesis. After a thorough review of the CAD model, technical drawings were produced and sent to Heimdal Industriservice AS, who manufactured the test rig. When the finished test rig arrived, mounting went seamlessly, except for a partition wall which had manufacturing errors. Luckily, the wall was not essential for the experimental setup.

An integral part of a structural finite element model is the material modelling framework. Based on existing literature, a constitutive model suitable for describing the behaviour of aluminium alloys was determined, as well as a fracture criterion for modelling failure. The material parameters were then identified. The material of the plate was characterised through tensile testing and reverse engineering, while the parameters found by Morin et al. [1] were used for the stiffened panel.

The test matrix was constructed based on preliminary numerical studies on simplified models subjected to CFD generated loading.

The experimental study consisted of tests on a rigid plate, simple deformable plates and deformable stiffened panels. In addition to testing different nominal firing pressures, two different tube outlet configurations were tested, to create different load complexities. The results indicate that the experimental setup successfully subjected plated structures to loads with high magnitude, short duration and non-uniform spatial and temporal distribution.

The rigid plate tests were performed on a massive aluminium plate mounted with pressure sensors. These tests were conducted in order to determine the approximate pressure distributions on the deformable test specimens, and to visualise the shock wave as it propagates from the driven outlet to the test specimen by utilising the BOS technique. The pressure data was intended to be utilised for the quantitative evaluation of the Eulerian simulations used in the preliminary and numerical parts of this study. However, the extreme pressures proved difficult to measure. A measurement technique based on piezoelectric sensors designed for shock tubes was utilised. Although the first 3-4 ms of the test data seem correct, dependent on the test, the data was largely compromised. A spurious drift of negative nature is seen in all measurements, and as the drift is inconsistent, it is difficult to isolate and correct for. Nevertheless, an attempt to correct the data was performed. A correlation between the complexity of the fluid flow and the amount of negative drift is registered. Ways complex fluid flow can distort pressure measurement in the setup used in this study has been explored, as well as other causes. Although some causes are more likely than others, no definitive cause could be determined. This study suggests that traditional shock tube measurement techniques should be used with caution for extreme pressure loading with complex flow effects.

The simple deformable plate tests were executed as planned without any problems. Measuring the deflections with 3D-DIC was straightforward. The deflections were larger than anticipated in the preliminary studies, but the tests were successful in strictly inducing Mode I failure with large inelastic deformations.

The deformable tests on the stiffened panel were executed as planned, and one additional test was conducted. Considerable time was spent on determining the appropriate boundary conditions for the stiffened panel tests, where simply supported was elected. 3D-DIC was challenging due to the stiffeners and the weld guide-rails, leading to differences between the two cameras. However, the deflections were successfully measured by subset DIC. The deflections were more or less as predicted in the preliminary studies, both with regard to shape and magnitude.

CFD simulations with the same conditions as the rigid plate tests were conducted in EUROPLEXUS, to enable direct comparison. The spatial distributions of the numerical loads had close resemblance to the experimental results. However, the peak reflected overpressures were 40 to 50% larger in the rigid plate tests, and the rise times were about 90% shorter. A finer mesh of the fluid subdomain would have yielded better results for both these parameters, but simulations with refined mesh were not conducted due to time restrictions. Due to the spurious drift in the experimental measurements, only the first four milliseconds are comparable. Both the CFD and the corrected experimental load histories were applied to the plate model in ABAQUS/Explicit to assess the resulting structural response. However, the CFD loads yielded better correspondence to the deformable plate tests. Thus only the CFD loads were used in parametric studies and for the panel.

The method for modelling the non-uniform spatial and temporal loading consisted in partitioning the surface of the ABAQUS/Explicit models exposed to pressure into 100 subareas, a surface mesh, and applying a separate load history to each subarea. From the CFD simulations the pressure data could be gathered

directly from the corresponding subarea of the rigid wall. The experimental pressure data on the other hand was limited to 16 measurement points. Thus, an interpolation algorithm denoted the griddata-algorithm was applied to determine the approximate load history for each subarea. To evaluate the performance of the griddata-algorithm, pressure data was gathered both from each subarea and at the sensor positions in the CFD simulations. The griddata-algorithm was then applied to the measurements from the sensor positions, to approximate the subarea values. Comparing the true subarea values to the interpolated values confirmed a good approximation of the spatial and temporal distribution. In addition to the direct comparison between the load histories, the resulting structural responses from applying the load histories to the Lagrangian plate model was compared. No noticeable difference between the maximal midpoint deflections resulting from the true and approximate load histories were found. The discretisation of the load is a simplification and could give some deviations.

From the discrepancy between the structural response of the Lagrangian plate model subjected to the CFD loading and the experimental results, it was deduced that the plate model had to include modelling of the boundary. Thus, the plate model was upgraded to include a clamping frame and bolts. Although the resulting structural responses from the upgraded model improved, the discrepancy was still large. The panel simulations however, yielded better correspondence to the experimental results. The reason for this is likely twofold. The first reason is that the boundary conditions of the panel are much simpler and thus easier to model and secondly the plate is more sensitive to the spatial and temporal distribution of the pressure load than the panel. Also, FSI effects were not included.

The panel model presented in [1] predicted the deformation modes in the tests. The strength reduction in the HAZ initiated strain localisation, and a plastic hinge developed, which resulted in an asymmetrical response.

7.2 Concluding Remarks

The most important findings obtained through the work in this thesis are as follows:

- Experimental setup:
 - The experimental setup designed in this study was able to generate a loading with a high magnitude, short duration and non-uniform spatial and temporal distributions.
 - The pressure measurement technique used in this study was validated for traditional shock tube testing. In this study, the technique yielded compromised data, suggesting that improvements must be made to capture the extreme pressure loading.
 - The use of Finite Element-based DIC to measure the panel deflections was not possible. Subset-based DIC has to be used.
- Plated structures subjected to extreme pressure loads:
 - The tests with a deformable specimen showed large inelastic deformations, asymmetric responses and fractures. The tested structures responded differently to the loading conditions, but the response varied with the load magnitude and complexity for all structures.
 - The HAZ - a zone with lower material strength due to the welding process - forms a plastic hinge for large inelastic deformations, which leads to asymmetrical dynamic structural responses.
- Eulerian models of the experimental setup in in EUROPLEXUS:
 - The initial pressure measurements and BOS images suggest that the Eulerian simulations in EUROPLEXUS replicate the initial pressure loading and flow field reasonably well.
 - The mesh size used in this thesis was not sufficient to capture the rise time and peak magnitude of the extreme pressure load. Mesh sensitivity increases with the load magnitude and complexity.

- Prescribing extreme pressure loads to the Lagrangian models:
 - The griddata-algorithm efficiently interpolated sensor measurements across the plate field, enabling the load description as a surface mesh.
 - The study indicates that an uncoupled analysis accurately can predict the structural response of plated structures subjected to extreme pressure loads generated in a shock tube environment. This can be done through prescribing the load to the structural model as a surface mesh. However, accurate Lagrangian and Eulerian models are paramount.
- Lagrangian models in ABAQUS/Explicit:
 - The design of experimental setups with minimal constraints greatly simplifies the modelling process and limits the uncertainties.
 - The modelling of clamped plated structures subjected to extreme pressure loading is a very complex endeavour, and it is difficult to capture the physical behaviour numerically.
 - The modelling of the HAZ as a homogenised section along the weld, with weaker material properties than the surrounding material, captures the strain localisation well.
 - The study indicates that the model presented in [1] accurately captures the behaviour of the stiffened panel. However, the fracture parameter is too small.

7.3 Further Work

Based on the work and findings presented in this thesis, the following further work is suggested:

- Performing new material tests and calibrations of the stiffened panels to assess if the material behaviour has changed since it was characterised in [1].
- Determining a measurement technique suitable for measuring extreme pressure loading.
- Validating the modelling approach of extreme pressure loading by prescribing pressure-time histories to subareas, utilising correct pressure measurements.
- Refining the mesh in the CFD simulations of the fluid sub-domain to better capture the rise time, the peak reflected overpressure and the pressure fluctuations.
- Further investigating the fluid-structure interactions - particularly with a coupled analysis.
- Further investigating how to numerically model the boundary conditions of the clamped plate, particularly modelling the whole rig.
- Investigating the strain softening and adiabatic heating effects - particularly for the HAZ with its strain localisation.
- Characterising the fracture behaviour of stiffened panels subjected to extreme pressure loading.
- Investigating the influence of the contact thickness reduction of the shell models.
- Investigating why there is a better correspondence between experiments and simulations with 20 bar nominal firing pressure, particularly by performing experiments with lower firing pressures. This study indicates that the correspondence will increase with decreasing firing pressure as the CFD simulations seem less accurate at higher firing pressures. In addition, FSI effects will decrease with decreasing deflections.

References

- [1] D. Morin, B. L. Kaarstad, B. Skajaa, O. S. Hopperstad, and M. Langseth, “Testing and modelling of stiffened aluminium panels subjected to quasi-static and low-velocity impact loading,” *International Journal of Impact Engineering*, vol. 110, pp. 97 – 111, 2017. Special Issue in honor of Seventy Fifth Birthday of Professor N. K. Gupta.
- [2] T. Haugstad 2016.
- [3] F. G. Friedlander and G. I. Taylor, “The diffraction of sound pulses i. diffraction by a semi-infinite plane,” *Proceedings of the Royal Society of London. Series A. Mathematical and Physical Sciences*, vol. 186, no. 1006, pp. 322–344, 1946.
- [4] S. B. Menkes and H. J. Opat, “Broken beams - tearing and shear failures in explosively loaded clamped beams.,” *Experimental Mechanics*, vol. 13, p. 480–486, 1973.
- [5] R. G. Teeling-Smith and G. N. Nurick, “The deformation and tearing of thin circular plates subjected to impulsive loads,” *International Journal of Impact Engineering*, vol. 11, no. 1, pp. 77 – 91, 1991.
- [6] M. Olson, G. Nurick, and J. Fagnan, “Deformation and rupture of blast loaded square plates—predictions and experiments,” *International Journal of Impact Engineering*, vol. 13, no. 2, pp. 279 – 291, 1993.
- [7] G. N. Nurick, M. E. Gelman, and N. S. Marshall, “Tearing of blast loaded plates with clamped boundary conditions,” *International Journal of Impact Engineering*, vol. 18, no. 7, pp. 803 – 827, 1996.
- [8] G. N. Nurick and G. C. Shave, “The deformation and tearing of thin square plates subjected to impulsive loads—an experimental study,” *International Journal of Impact Engineering*, vol. 18, no. 1, pp. 99 – 116, 1996.
- [9] N. Jones, “A theoretical study of the dynamic plastic behavior of beams and plates with finite-deflections,” *International Journal of Solids and Structures*, vol. 7, no. 8, pp. 1007 – 1029, 1971.
- [10] N. Jones, *Structural Impact*. Cambridge University Press, 2012.
- [11] Y. Peng, P. Yang, and K. Hu, “Nonlinear dynamic response of blast-loaded stiffened plates considering the strain rate sensitivity,” *Marine Structures*, vol. 70, p. 102699, 2020.
- [12] Z. Yu, J. Amdahl, and Y. Sha, “Large inelastic deformation resistance of stiffened panels subjected to lateral loading,” *Marine Structures*, vol. 59, pp. 342 – 367, 2018.
- [13] S. C. K. Yuen and G. N. Nurick, “Experimental and numerical studies on the response of quadrangular stiffened plates. part i: subjected to uniform blast load,” *International Journal of Impact Engineering*, vol. 31, no. 1, pp. 55 – 83, 2005.
- [14] G. N. Nurick, M. D. Olson, J. R. Fagnan, and A. Levin, “Deformation and tearing of blast-loaded stiffened square plates,” *International Journal of Impact Engineering*, vol. 16, no. 2, pp. 273 – 291, 1995.
- [15] R. B. Schubak, M. D. Olson, and D. L. Anderson, “Rigid-plastic modelling of blast-loaded stiffened plates—part i: One-way stiffened plates,” *International Journal of Mechanical Sciences*, vol. 35, no. 3, pp. 289 – 306, 1993.
- [16] R. B. Schubak, M. D. Olson, and D. L. Anderson, “Rigid-plastic modelling of blast-loaded stiffened plates—part ii: Partial end fixity, rate effects and two-way stiffened plates,” *International Journal of Mechanical Sciences*, vol. 35, no. 3, pp. 307 – 324, 1993.
- [17] G. K. Schleyer, S. S. Hsu, M. D. White, and R. S. Birch, “Pulse pressure loading of clamped mild steel plates,” *International Journal of Impact Engineering*, vol. 28, no. 2, pp. 223 – 247, 2003.

- [18] Y. Pan and L. A. Louca, “Experimental and numerical studies on the response of stiffened plates subjected to gas explosions,” *Journal of Constructional Steel Research*, vol. 52, no. 2, pp. 171 – 193, 1999.
- [19] L. A. Louca, Y. G. Pan, and J. E. Harding, “Response of stiffened and unstiffened plates subjected to blast loading,” *Engineering Structures*, vol. 20, no. 12, pp. 1079 – 1086, 1998.
- [20] J. K. Paik, “Empirical formulations for predicting the ultimate compressive strength of welded aluminum stiffened panels,” *Thin-Walled Structures*, vol. 45, no. 2, pp. 171 – 184, 2007.
- [21] D. Bonorchis and G. N. Nurick, “The analysis and simulation of welded stiffener plates subjected to localised blast loading,” *International Journal of Impact Engineering*, vol. 37, no. 3, pp. 260 – 273, 2010.
- [22] EUROPLEXUS, “User’s manual - a computer program for the finite element simulation of fluid-structure systems under transient dynamic loading.”
URL: <https://europlexus.jrc.ec.europa.eu/> (accessed 04/25/2020).
- [23] Abaqus/CAE 6.14-1, Dassault Systèmes SIMULIA Corp, USA, 2019.
- [24] V. Aune, *Behaviour and modelling of flexible structures subjected to blast loading*. PhD thesis, Norwegian University of Science and Technology, Trondheim, 2017.
- [25] V. Aune, G. Valsamos, F. Casadei, M. Langseth, and T. Børvik, “On the dynamic response of blast-loaded steel plates with and without pre-formed holes,” *International Journal of Impact Engineering*, vol. 108, pp. 27 – 46, 2017. In Honour of the Editor-in-Chief, Professor Magnus Langseth, on his 65th Birthday.
- [26] M. Larcher, “Simulation of the effects of an air blast wave,” Tech. Rep. EUR 41337 EN, JRC, Luxembourg, 2007.
- [27] H. N. G. Wadley, T. Børvik, L. Olovsson, J. J. Wetzel, K. P. Dharmasena, O. S. Hopperstad, V. S. Deshpande, and J. W. Hutchinson, “Deformation and fracture of impulsively loaded sandwich panels,” *Journal of the Mechanics and Physics of Solids*, vol. 61, no. 2, pp. 674 – 699, 2013.
- [28] B. L. Kårstad and B. Skajaa, “Impact behaviour of stiffened aluminium plates,” *Norwegian University of Science and Technology Master’s. thesis*, 2015.
- [29] E. J. Lien and A. Skyrud, “Impact behaviour of stiffened aluminium plates,” *Norwegian University of Science and Technology Master’s. thesis*, 2016.
- [30] 3D models software, DASSAULT SYSTEMES;
URL: <https://www.solidworks.com/> (accessed 06/22/2020).
- [31] M. Ortiz and J. C. Simo, “An analysis of a new class of integration algorithms for elastoplastic constitutive relations,” *International Journal for Numerical Methods in Engineering*, vol. 23, no. 3, pp. 353–366, 1986.
- [32] T. Belytschko, *Nonlinear Finite Elements for Continua and Structures*. John Wiley Sons, Ltd, 2nd ed., 2014.
- [33] E. Fagerholt, “Field measurements in mechanical testing using close-range photogrammetry and digital image analysis.,” *Norwegian University of Science and Technology Ph.D. thesis*, 2011.
- [34] F. Hannard, T. Pardoën, E. Maire, C. L. Bourlot, R. Mokso, and A. Simar, “Characterization and micro-mechanical modelling of microstructural heterogeneity effects on ductile fracture of 6xxx aluminium alloys,” *Acta Materialia*, vol. 103, pp. 558 – 572, 2016.
- [35] T. Wang, O. S. Hopperstad, O.-G. Lademo, and P. K. Larsen, “Finite element analysis of welded beam-to-column joints in aluminium alloy en aw 6082 t6,” *Finite Elements in Analysis and Design*, vol. 44, no. 1, pp. 1 – 16, 2007.

- [36] A. Saai, S. Dumoulin, O. S. Hopperstad, and O.-G. Lademo, “Simulation of yield surfaces for aluminium sheets with rolling and recrystallization textures,” *Computational Materials Science*, vol. 67, pp. 424 – 433, 2013.
- [37] W. F. Hosford, *The Mechanics of Crystals and Textured Polycrystals*. Oxford engineering science series, Oxford University Press, 1993.
- [38] M. G. Cockroft and D. J. Latham, “Ductility and the workability of metals,” *Journal of the Institute of Metals*, vol. 96, pp. 33–39, 1968.
- [39] *Datasheet AA6082-T6/T651 Plate*. Aalco Metals Ltd., 2019.
- [40] C. Comte and J. von Stebut, “Microprobe-type measurement of young’s modulus and poisson coefficient by means of depth sensing indentation and acoustic microscopy,” *Surface and Coatings Technology*, vol. 154, no. 1, pp. 42 – 48, 2002.
- [41] ABAQUS, *Abaqus Analysis User’s Guide (6.14)*, 29.6.2 Choosing a shell element. URL: <http://ivt-abaqusdoc.ivt.ntnu.no:2080/v6.14/books/usb/pt06ch29s06alm16.html> (accessed 06/22/2020).
- [42] `scipy.optimize.curve_fit v1.3.1(Scipy)`, The SciPy community, 2019.
- [43] G. Gruben, D. Morin, M. Langseth, and O. Hopperstad, “Strain localization and ductile fracture in advanced high-strength steel sheets,” *European Journal of Mechanics A/Solids*, vol. 61, p. 315, 2017.
- [44] P. Hogström, J. Ringsberg, and E. Johnson, “An experimental and numerical study of the effects of length scale and strain state on the necking and fracture behaviours in sheet metals,” *International Journal of Impact Engineering - INT J IMPACT ENG*, vol. 36, pp. 1194–1203, 10 2009.
- [45] V. Aune, T. Børvik, and M. Langseth, “An introduction to blast mechanics,” *Lecture Notes TKT4128, NTNU*, 2019.
- [46] T. Belytschko, W. K. Liu, B. Moran, and K. I. Elkhodary, *Nonlinear Finite Elements for Continua and Structures*. Chichester, West Sussex: Wiley, 2nd ed., 2014.
- [47] T. Børvik, A. G. Hanssen, M. Langseth, and L. Olovsson, “Response of structures to planar blast loads – a finite element engineering approach,” *Computers Structures*, vol. 87, no. 9, pp. 507 – 520, 2009.
- [48] F. Casadei, J. P. Halleux, A. Sala, and F. Chillè, “Transient fluid–structure interaction algorithms for large industrial applications,” *Computer Methods in Applied Mechanics and Engineering*, vol. 190, no. 24, pp. 3081 – 3110, 2001. Advances in Computational Methods for Fluid-Structure Interaction.
- [49] V. Aune, G. Valsamos, F. Casadei, M. Langseth, and T. Børvik, “Fluid-structure interaction effects during the dynamic response of clamped thin steel plates exposed to blast loading,” *International Journal of Impact Engineering*, 2020.
- [50] Open-source software ParaView; URL: <https://https://www.paraview.org/> (accessed 05/25/2020).
- [51] R. Andreotti, M. Colombo, A. Guardone, P. Martinelli, G. Riganti, and M. [di Prisco], “Performance of a shock tube facility for impact response of structures,” *International Journal of Non-Linear Mechanics*, vol. 72, pp. 53 – 66, 2015.
- [52] Wikipedia contributors, “Euler equations (fluid dynamics) — Wikipedia, the free encyclopedia,” 2020. [Online; accessed 1-June-2020].
- [53] V. Aune, E. Fagerholt, M. Langseth, and T. Børvik, “A shock tube facility to generate blast loading on structures,” *International Journal of Protective Structures*, vol. 7, no. 3, pp. 340–366, 2016.
- [54] F. Casadei, P. Díez, and F. Verdugo, “An algorithm for mesh refinement and un-refinement in fast transient dynamics,” *International Journal of Computational Methods*, vol. 10, pp. 1–31, 2013.

- [55] E. Deulin, V. Mikhailov, Y. Panfilov, and R. Nevshupa, *Mechanics and Physics of Precise Vacuum Mechanisms*, vol. 91. 01 2010.
- [56] S. Rigby, A. Tyas, T. Bennett, S. Clarke, and S. Fay, “The negative phase of the blast load,” *International Journal of Protective Structures*, vol. 5, pp. 1–20, 03 2014.
- [57] W. E. Baker, P. A. Cox, J. J. Kulesz, R. A. Strehlow, and P. S. Westine, *Explosion Hazards and Evaluation*, vol. 5. Elsevier Science pp 271-282, 1983.
- [58] R. D. Blevins, *Formulas for natural frequency and mode shape*. Van Nostrand Reinhold Company pp 233-287, 1979.
- [59] Y. Chen, A. Clausen, O. Hopperstad, and M. Langseth, “Stress–strain behavior of aluminium alloys at a wide range of strain rates,” *International Journal of Solids and Structures - INT J SOLIDS STRUCT*, vol. 46, pp. 3825–3835, 10 2009.
- [60] E. Fagerholt. eCorr v4.0 Documentation, url: <http://folk.ntnu.no/egilf/ecorr/doc/>, C,.
- [61] G. Settles and M. Hargather, “A review of recent developments in schlieren and shadowgraph techniques,” *Measurement Science and Technology*, vol. 28, 01 2017.
- [62] H. Richard and M. Raffel, “Principle and applications of the background oriented schlieren (bos) method,” *Measurement Science and Technology*, vol. 12, pp. 1576–1585, 09 2001.
- [63] BOS code developed in Python at SIMLab, NTNU, 2020, URL: <https://github.com/PolymerGuy/openBOS> (accessed 04/30/2020).
- [64] Communications with Jostein Kyte at Scanditest Norge AS.
- [65] R. J. Fradette, “Understanding vacuum and vacuum measurement,” 2016. SOLAR ATMOSPHERES, INC.
- [66] *Data sheet, Type 603B*. Kistler Holding AG.
- [67] US Department of Defence, “Structures to resist the effects of accidental explosions.” US DoD, Washington DC, USA, UFC-3-340-02, 2008.
- [68] Z. Yu, J. Amdahl, and Y. Sha, “Large inelastic deformation resistance of stiffened panels subjected to lateral loading,” *Marine Structures*, vol. 59, pp. 342 – 367, 2018.
- [69] `scipy.interpolate.griddata v1.3.1(Scipy)`, The SciPy community, 2019.
- [70] Engineering ToolBox, “Friction and friction coefficients,” 2004. [Online; accessed 12-Feb-2020].
- [71] V. Aune, G. Valsamos, F. Casadei, M. Larcher, M. Langseth, and T. Børvik, “Numerical study on the structural response of blast-loaded thin aluminium and steel plates,” *International Journal of Impact Engineering*, vol. 99, pp. 131 – 144, 2017.
- [72] V. Aune, G. Valsamos, F. Casadei, and T. Børvik in *Aspects of fluid-structure interaction on the dynamic response of blast-loaded metallic plates*, 10 2019.

A Shock Tube Experiments

A.1 Rigid Plate

A.1.1 Dimensions and Pressure Sensor Location

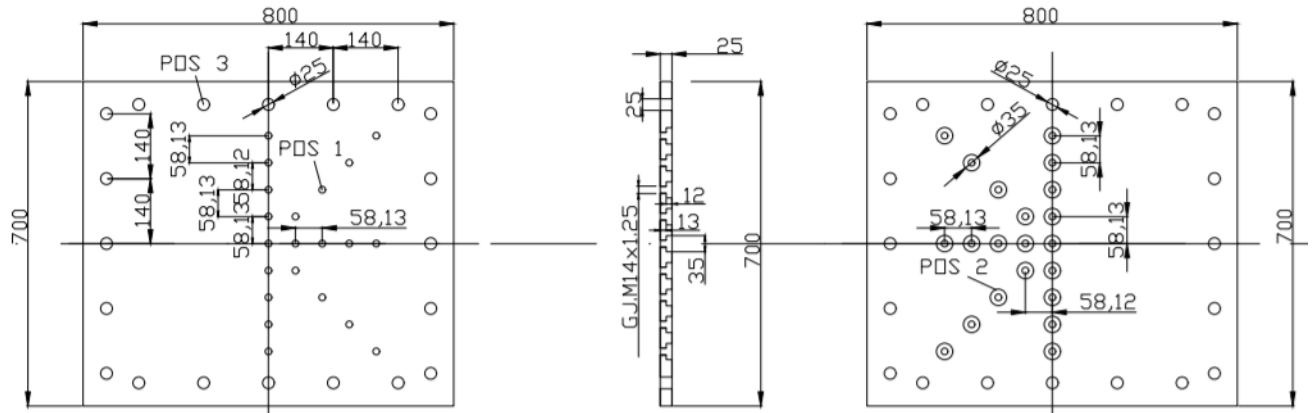


Figure A.1: Dimension of the rigid plate and spatial orientation of the pressure sensors are illustrated.

A.1.2 Code for Numerical Filtration and Correction of Pressure Measurements

```
# NF_SSTF_pressures.py
# by Odin Celius and Magnus L. Knoph

# Table of Contents
# -----
# 1. Required modules
# 2. Utilities
# 3. Filtration function for open configuration tests
# 4. Filtration function for wall configuration tests
# 5. Correction function

# 1. Required modules
# -----
import os
import xlrd
import numpy as np
import copy
from scipy import signal

# 2. Utilities
```



```

# -----
def datasheetToDictionaryHandler(ws):
    RAW = {}
    for i in range(ws.ncols):
        key = ws.cell_value(0, i)
        RAW[key] = np.asarray(ws.col_values(i, 2))
        if key != 'Time' and RAW[key][0] < 0:
            RAW[key] = RAW[key] - RAW[key][0]
    if ws.name == 'RP_0_60':
        for i in range(len(RAW['Time'])):
            if RAW['Time'][i] > RAW['Time'][0] + 25:
                for key in RAW:
                    RAW[key] = RAW[key][:i]
                break
    if 'EPX' not in ws.name:
        for pos in range(len(RAW['P01_1'])):
            if RAW['P01_1'][pos] > 0.5:
                RAW['Time'] -= RAW['Time'][pos]
                break
    return RAW

def running_avg(y):
    oddNumber = 5
    travel = int(np.floor(oddNumber/2.))
    yliste_NF = []
    for i in range(travel, (len(y) - travel), oddNumber):
        yliste_NF.append(np.ma.average(y[i-travel:i+travel]))
    return yliste_NF

def columnDictSmoother(data, key, i):
    data[key][i] = data[key][i] / 5.

def expectedGlobalMinima(filteredMaxima):
    return -29./380 - filteredMaxima * 9./380

# 3. Filtration function for open configuration tests
# -----
def NF_Open(data):
    data = copy.deepcopy(data)

```

```

b, a = signal.butter(5, 0.01)
b4, a4 = signal.butter(5, 0.0005)
for i in range(len(data['Time'])):
    if data['Time'][i] > 5:
        startIndex = i
        break
globalPeakIndex = np.argmax(data['PC_01'][:startIndex])
globalPeak = data['PC_01'][globalPeakIndex]
for key in data:
    if key != 'Time':
        for i in range(startIndex, len(data[key])):
            if np.abs(data[key][i]) > globalPeak * 0.7:
                columnDictSmoother(data, key, i)
            if np.abs(data[key][i] - data[key][i - 1]) > globalPeak/2.:
                columnDictSmoother(data, key, i)
            if i > startIndex * 3:
                if np.abs(data[key][i]) > globalPeak * 0.5:
                    columnDictSmoother(data, key, i)
                if np.abs(data[key][i] - data[key][i - 1]) > globalPeak/3.:
                    columnDictSmoother(data, key, i)
            if i > startIndex * 6.5:
                if np.abs(data[key][i]) > globalPeak * 0.3:
                    columnDictSmoother(data, key, i)
        firstPeakIndex = np.argmax(data[key][:startIndex])
        firstPeakIndex += 70
        if key in ['PC_08', 'PC_11', 'PC_12']:
            data[key][firstPeakIndex:] = np.asarray(
                signal.filtfilt(b4, a4, data[key][firstPeakIndex:]))
        else:
            data[key][firstPeakIndex:] = \
                np.asarray(signal.filtfilt(b, a, data[key][firstPeakIndex:]))
        data[key] = np.asarray(running_avg(data[key]))
        switchIndex = int(np.floor(startIndex * 2 / 9.))
        data[key] = np.asarray(list(data[key][:switchIndex])
            + list(running_avg(running_avg(data[key][switchIndex:]))))
    if key != 'Time':
        number = 4
        for i in range(switchIndex, len(data[key])):
            if np.sum(np.abs(np.asarray(data[key][i - number + 1:i + 1]) -
                np.asarray(data[key][i - number:i]))) > globalPeak/3. \
                and i%number == 0:
                columnDictSmoother(data, key, list(range(i - number, i + 1)))
return data

```

```

# 4. Filtration function for wall configuration tests
# -----
def NF_Wall(data, name):
    data = copy.deepcopy(data)
    b, a = signal.butter(5, 0.01)
    b4, a4 = signal.butter(5, 0.0005)
    for i in range(len(data['Time'])):
        if data['Time'][i] > 1.7:
            startIndex = i
            break
    globalPeakIndex = np.argmax(data['PC_02'][:startIndex])
    globalPeak = data['PC_02'][globalPeakIndex]
    for key in data:
        if key != 'Time':
            for i in range(startIndex, len(data[key])):
                if (np.abs(data[key][i]) > globalPeak * 1. and '60' in name) or \
                    (np.abs(data[key][i]) > globalPeak * 2.2 and '60' not in name):
                    columnDictSmoother(data, key, i)
                if np.abs(data[key][i] - data[key][i - 1]) > globalPeak/2.:
                    columnDictSmoother(data, key, i)
                if i > startIndex * 8:
                    if data[key][i] > globalPeak * 0.3:
                        columnDictSmoother(data, key, i)
            firstPeakIndex = np.argmax(data[key][:startIndex])
            firstPeakIndex += 70
            if key in ['PC_08', 'PC_11', 'PC_12']:
                data[key][firstPeakIndex:] = np.asarray(
                    signal.filtfilt(b4, a4, data[key][firstPeakIndex:]))
            else:
                data[key][firstPeakIndex:] = \
                    np.asarray(signal.filtfilt(b, a, data[key][firstPeakIndex:]))
            data[key] = np.asarray(running_avg(data[key]))
            switchIndex = int(np.floor(startIndex * 2 / 9.))
            data[key] = np.asarray(list(data[key][:switchIndex]) +
                                   list(running_avg(running_avg(data[key][switchIndex:]))))
    return data

# 5. Correction function
# -----
def minimaBasedCorrector(EXP_NF):

```

```

data = copy.deepcopy(EXP_NF)
##
filteredMinimaIndex = 100000
filteredMinima = 0
filteredMaxima = 0
for key, item in data.items():
    if key not in ['Time', 'PC_08', 'PC_11', 'PC_12', 'P01_1', 'P01_2']:
        for i in range(len(item)):
            if (item[i] < 0.90 * filteredMinima and i < filteredMinimaIndex) or \
                item[i] < filteredMinima * 1.2:
                filteredMinima = item[i]
                filteredMinimaIndex = i
            if item[i] > filteredMaxima:
                filteredMaxima = item[i]
                filteredMaximaIndex = i
for key, item in data.items():
    if key != 'Time':
        for i in range(len(item)):
            if data['Time'][i] > data['Time'][filteredMinimaIndex]:
                data[key][i] += expectedGlobalMinima(filteredMaxima) - filteredMinima
            elif data['Time'][i] > data['Time'][filteredMaximaIndex]:
                data[key][i] += \
                    (expectedGlobalMinima(filteredMaxima) - filteredMinima) * \
                    (data['Time'][i] - data['Time'][filteredMaximaIndex]) / \
                    (data['Time'][filteredMinimaIndex] - data['Time'][filteredMaximaIndex])
            if data[key][i] < -0.75:
                data[key][i] = -0.75
##
return data

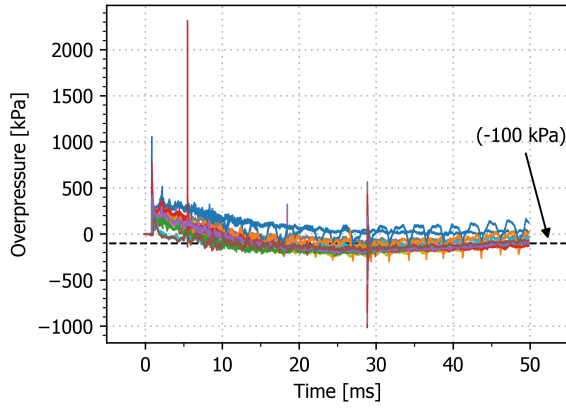
# 6. Program
# -----
folderPos = r'D:\Skole\Master(D)\ShockTubeExperiments'
test = 'RP_W_20_2'
directory = '{}\{}\{}'.format(folderPos, test)
os.chdir(directory)
wb = xlrd.open_workbook("ShockTubePressures.xlsx")
dataSheet = wb.sheet_by_index(0)

RAW = datasheetToDictionaryHandler(dataSheet)
if dataSheet.name.split('_')[1] == 'O':
    EXP_NF = NF_Open(RAW)
elif dataSheet.name.split('_')[1] == 'W':

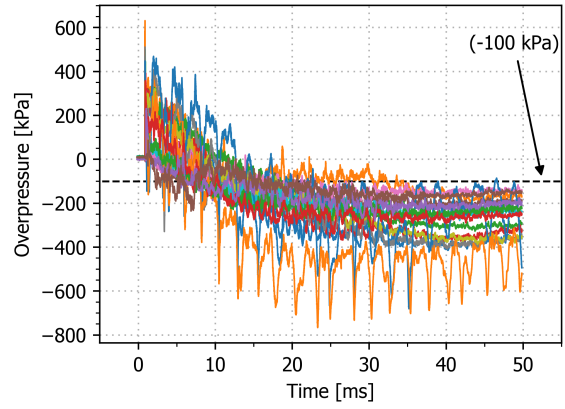
```

```
EXP_NF = NF_Wall(RAW, dataSheet.name)
EXP_C = minimaBasedCorrector(EXP_NF)
```

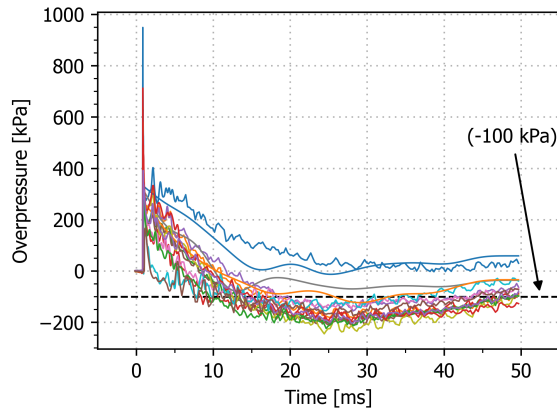
A.1.3 Pressure Measurements



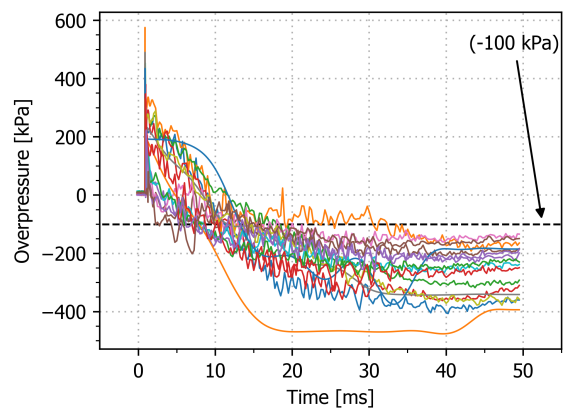
(a) RP_O_20_RAW



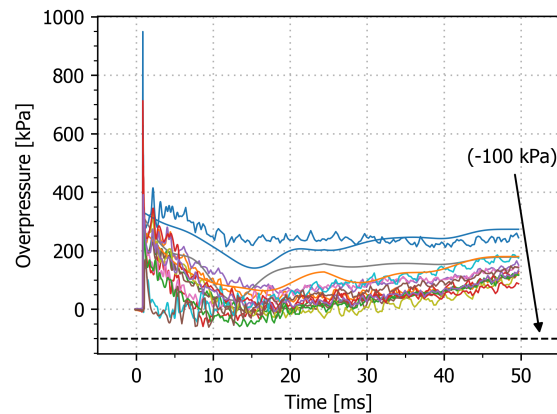
(b) RP_W_20.1_RAW



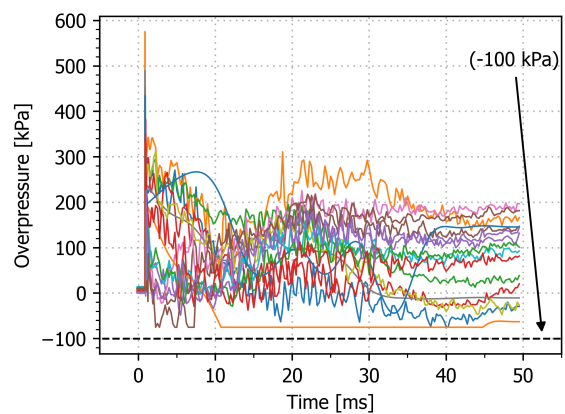
(c) RP_O_20_NF



(d) RP_W_20.1_NF

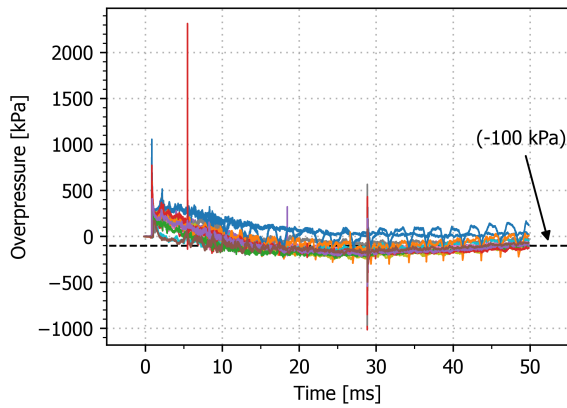


(e) RP_O_20_C

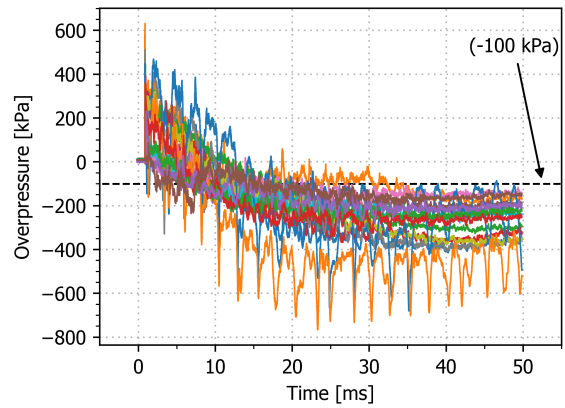


(f) RP_W_20.1_C

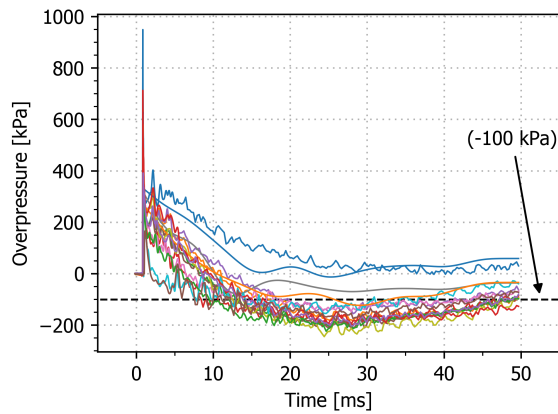
Figure A.2: Raw, numerically filtered and corrected overpressure-time histories from two of the tests at 20 bar.



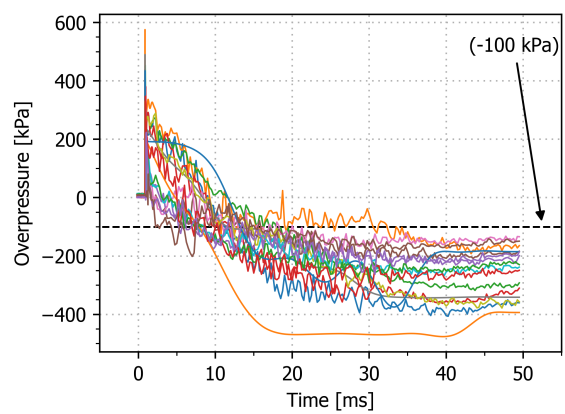
(a) RP_O_20_RAW



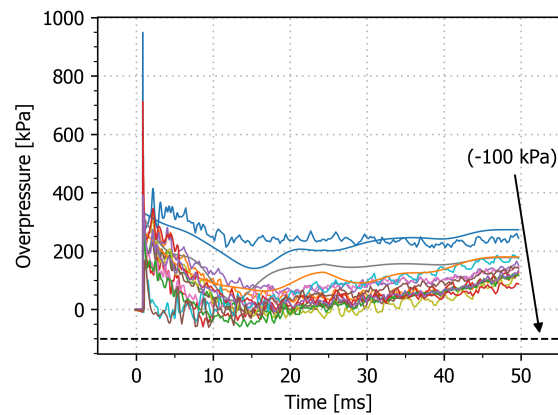
(b) RP_W_20.1_RAW



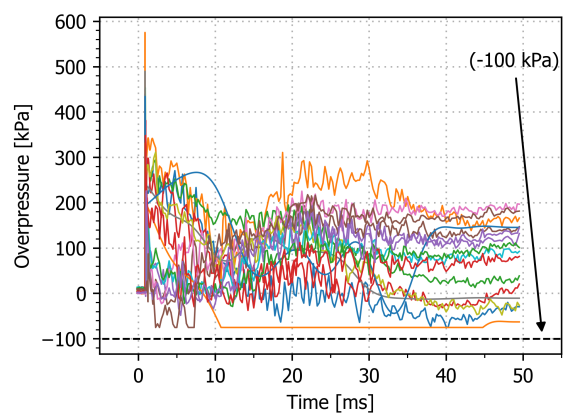
(c) RP_O_20_NF



(d) RP_W_20.1_NF

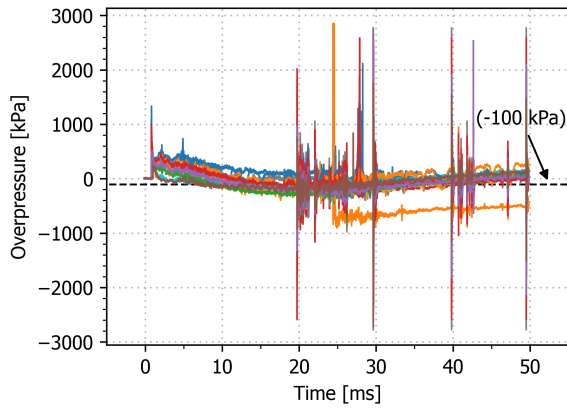


(e) RP_O_20_C

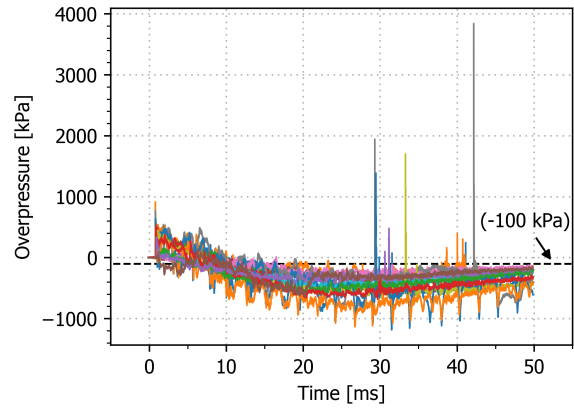


(f) RP_W_20.1_C

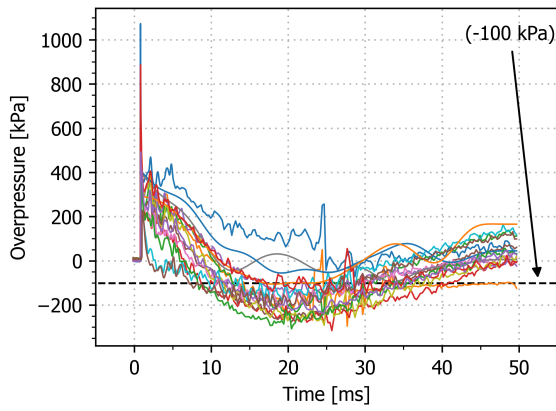
Figure A.3: Raw, numerically filtered and corrected overpressure-time histories from two of the tests at 20 bar.



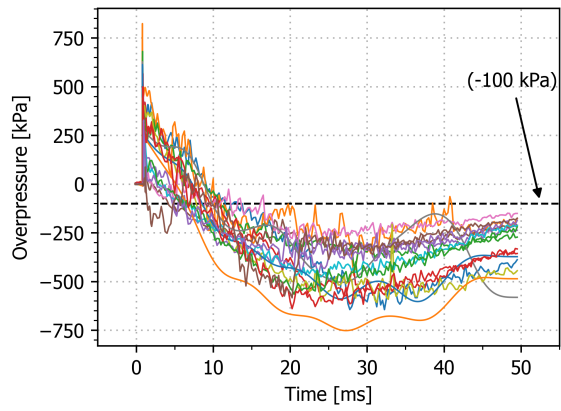
(a) RP_O_30_RAW



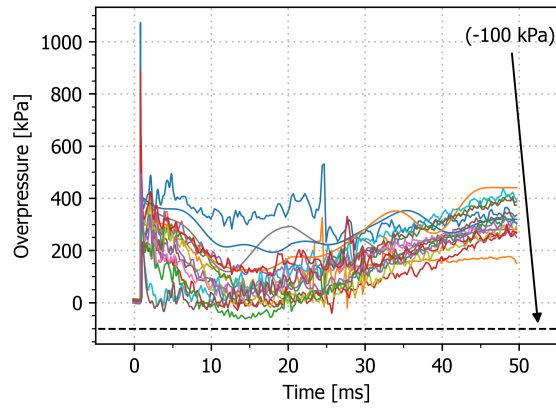
(b) RP_W_40_RAW



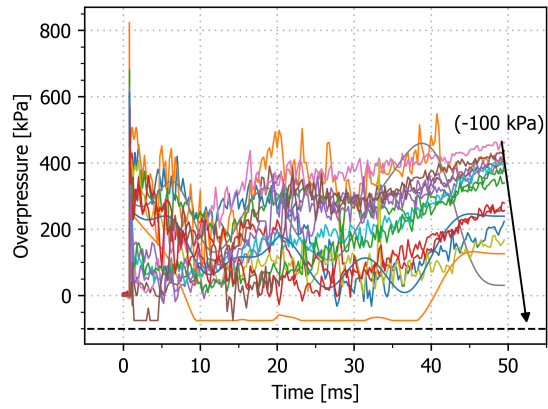
(c) RP_O_30_NF



(d) RP_W_40_NF

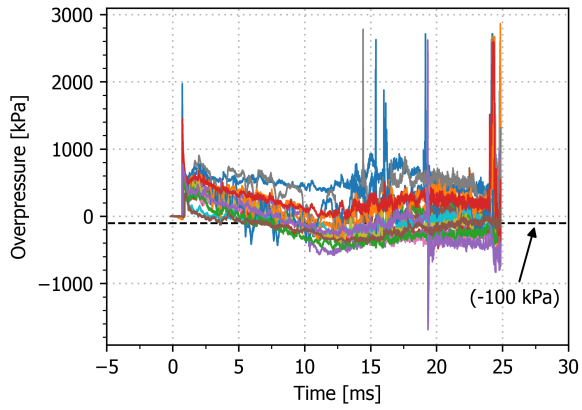


(e) RP_O_30_C

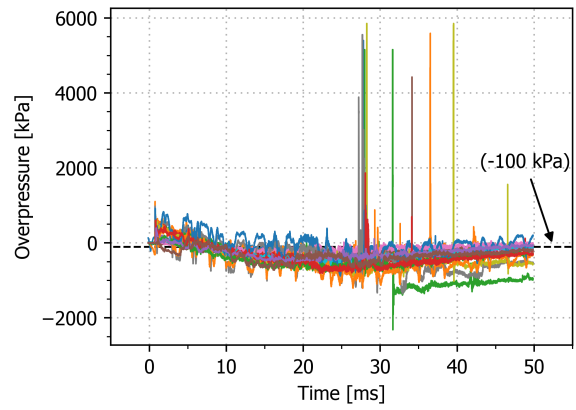


(f) RP_W_40_C

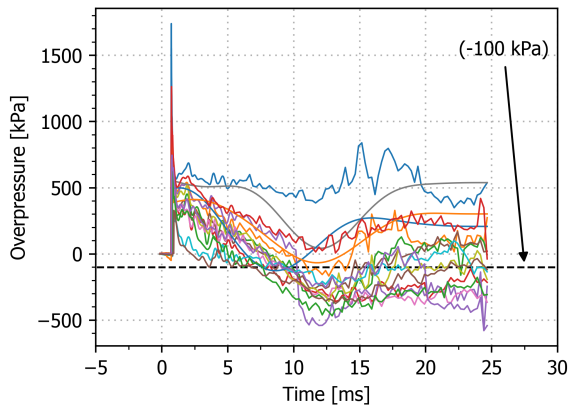
Figure A.4: Raw, numerically filtered and corrected overpressure-time histories from the tests at 30 and 40 bar.



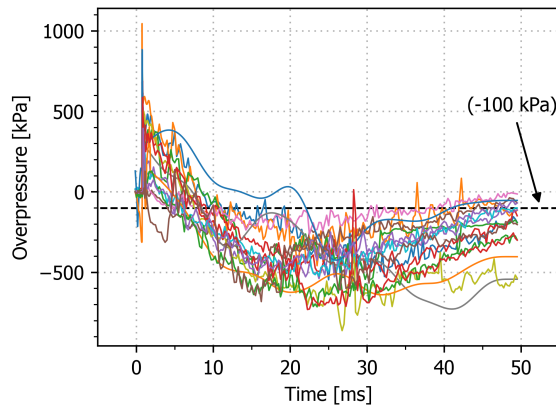
(a) RP_O_60_RAW



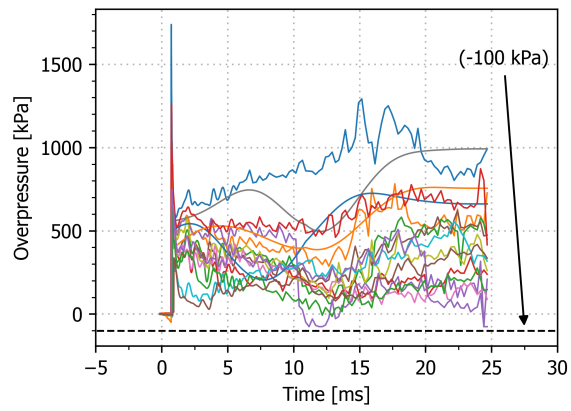
(b) RP_W_60_RAW



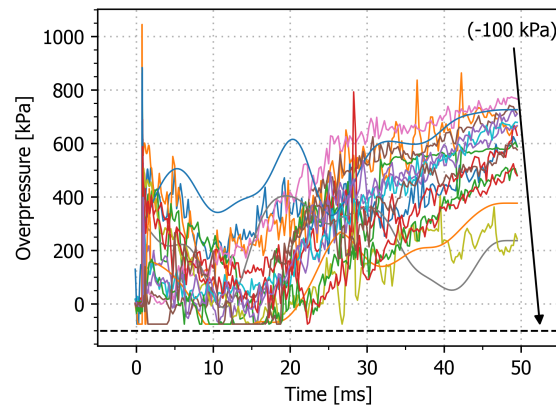
(c) RP_O_60_NF



(d) RP_W_60_NF



(e) RP_O_60_C



(f) RP_W_60_C

Figure A.5: Raw, numerically filtered and corrected overpressure-time histories from the tests at 60 bar.

A.1.4 BOS Code

```
import os

import matplotlib.pyplot as plt
import numpy as np
from imageio import imread
import scipy.signal as sig
from scipy.ndimage import gaussian_filter

"""
Synthetic Schlieren draft

It loads a set of images and subtracts the background.
The background is estimates as the average of the N next images.

Made by Sindre Nordmark Olufsen <sindre.n.olufsen@ntnu.no>

"""

def find_images_names(path,file_type = ".tif"):
    return sorted([file for file in os.listdir(path) if file.endswith(file_type)])

# Processing settings
image_folder_name = 'None'
image_folder = os.curdir+"/{}/".format(image_folder_name)
results_folder = os.curdir+"/{}_Results/".format(image_folder_name)
if not os.path.exists(results_folder):
    os.mkdir(results_folder)
first_image_ind = 0
n_images = 400
ref_depth = 50

# Visualization settings
overlay_blend_fraction = 0.2
diff_max_value = 5000.
clip_diff_above_fraction = 0.9

# Load the images to memory
image_names_all = find_images_names(image_folder,file_type=".tif")
n_images = len(image_names_all)
image_names_extracted = image_names_all[first_image_ind:first_image_ind+n_images+ref_depth]
```

```

images = np.array([imread(image_folder+image_name).astype(np.float32)
    for image_name in image_names_extracted])

print("The image stack contains %i images with the shape: %i x %i"%images.shape)

image_shape_n, image_shape_m = images[0].shape
max_gray_values = images.max()

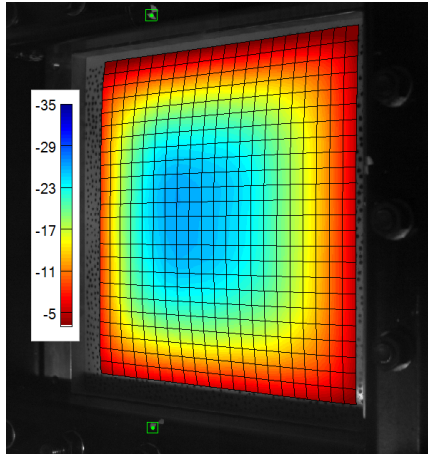
# Calculate the background image as the average of the images before
# the shockwave enters the frame
background = np.average(images[0:31,:,:],axis=0)
for i in range(n_images):
    print("Processing image nr: %i"%i)
    # Subtract background and calculate absolute value
    diff = np.abs(images[i,:,:]-background)
    diff = gaussian_filter(diff,sigma=1.0)
    # Normalize
    diff_norm = diff/diff_max_value
    # Clip above threshold
    diff_norm[diff_norm>clip_diff_above_fraction] = 1.0
    # Generate color image
    composition = overlay_blend_fraction * images[i][:,:,np.newaxis] *
        np.ones((image_shape_n,image_shape_m,3))/max_gray_values
    composition[:, :, 1] += (1.-overlay_blend_fraction) * (diff_norm)
    plt.imsave(results_folder+'field{0}{1}.png'.format(
        int(np.ceil(np.log10(n_images+1))-np.ceil(np.log10(i+2)))*'0', i+1), diff_norm)

```

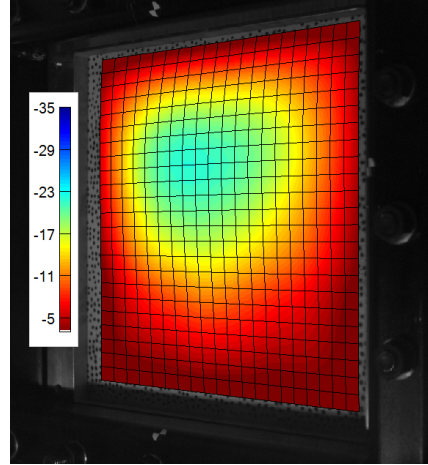
A.2 Plate

A.2.1 Rigid Body Motions of Shock Tube and Rig Frame

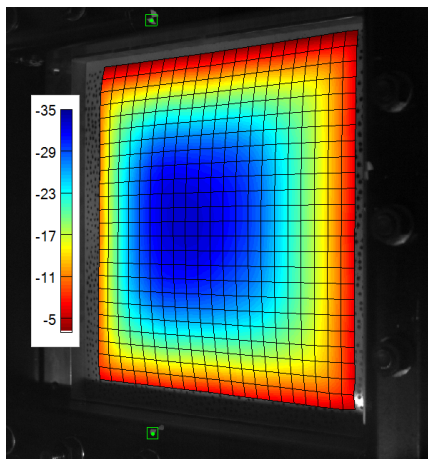
In Figure A.7b is the rigid body motions from setup and rig frame plotted for all plate tests. Values obtained from subset DIC (point tracking) of checkboard stickers on the frame. Only the lower horizontal frame member checkboard sticker was used to measure the rigid body movements, see Figure A.7a. Negative direction is defined as out of plane, thus negative direction is the same direction as shock wave propagation in the shock tube.



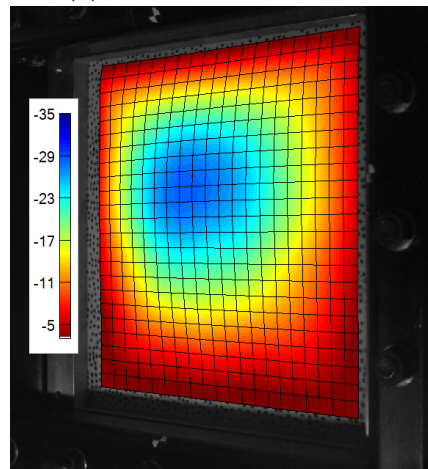
(a) Open 60% of max deflection



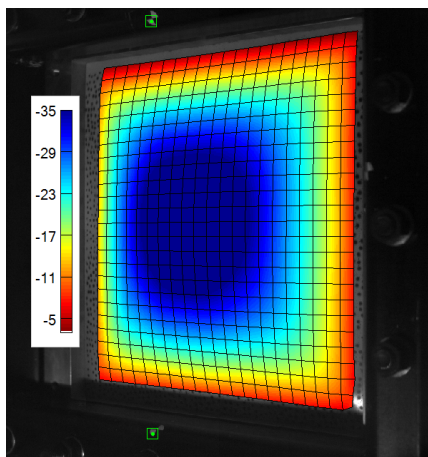
(b) Wall 60% of max deflection



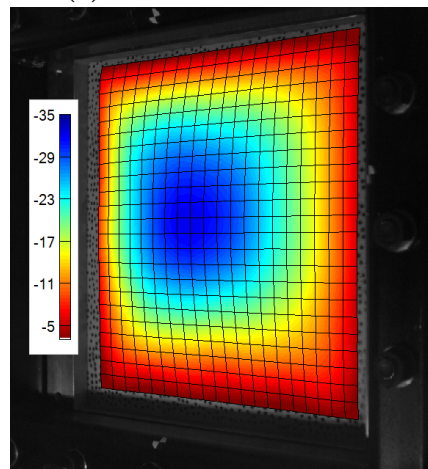
(c) Open 80% of max deflection



(d) Wall 80% of max deflection

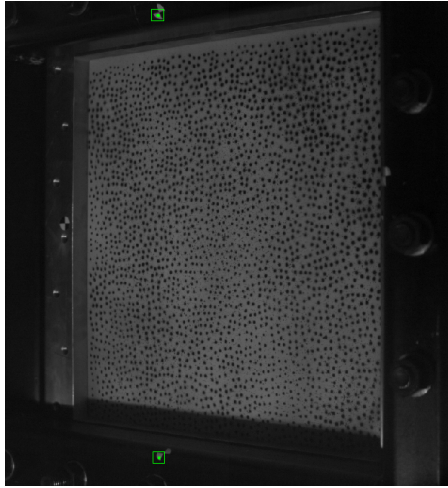


(e) "Open" 100% of max deflection

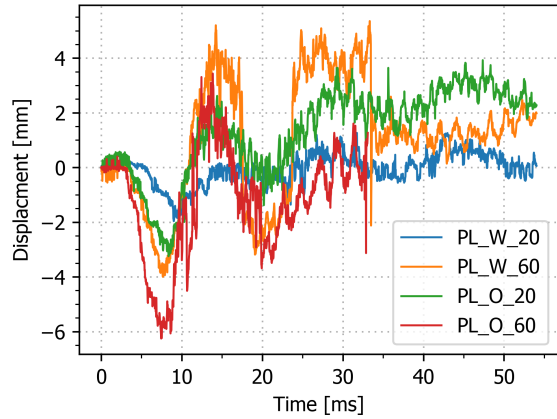


(f) Wall 100% of max deflection

Figure A.6: Comparison of the deformation field of the open and wall configuration at a nominal firing pressure of 20 bar. All the colour bars have equal scaling, with a range from -35 mm to -3 mm.



(a)

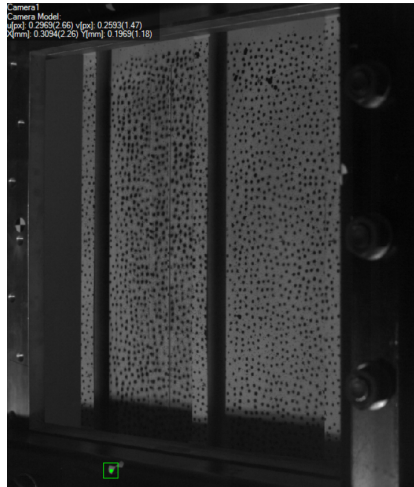


(b)

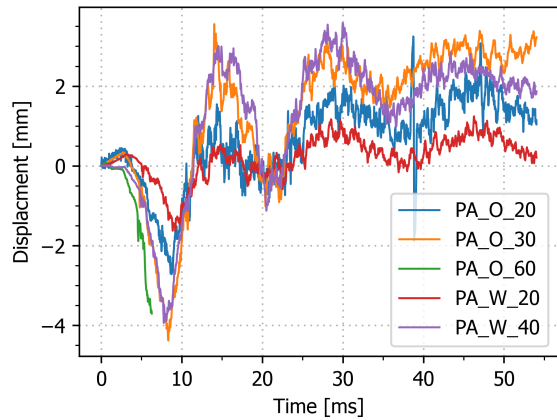
Figure A.7: (a) Screen dump from the eCorr software where subset DIC is chosen on the lower horizontal frame member of the new rig. The green square gets point traced. (b) Plate rigid body movements from all tests.

A.3 Stiffened Panel

A.3.1 Rigid Body Motions of Shock Tube and Rig Frame



(a)



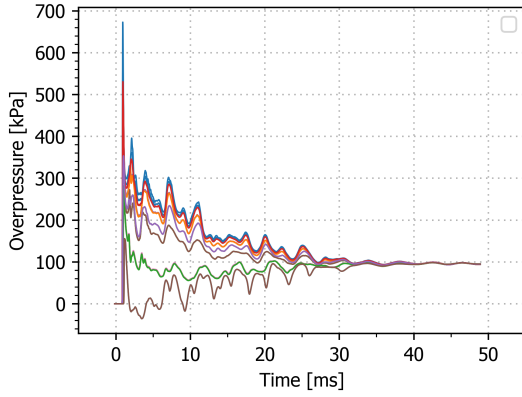
(b)

Figure A.8: (a) Screen dump from the eCorr software where subset DIC is chosen on the lower horizontal frame member of the new rig. The green square gets point traced with subset DIC. (b) Panel rigid body movements for all tests.

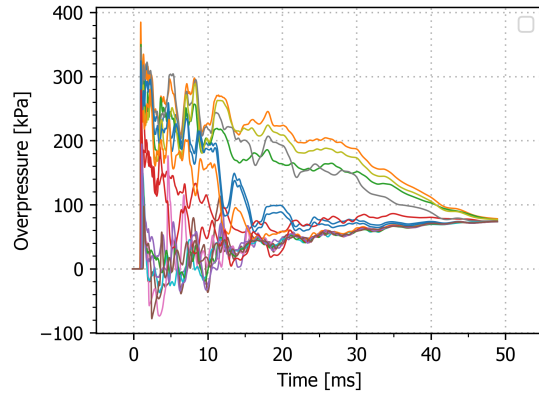
In Figure A.8b is the rigid body motions from setup and rig frame plotted for all stiffened panel tests. Values obtained from subset DIC (point tracking) of checkboard stickers on the frame. Only the lower horizontal frame member checkboard sticker was able to be visualised in both cameras, see Figure A.8a. Negative direction is defined as out of plane, thus negative direction is the same direction as shock wave propagation in the shock tube.

B Numerical Analysis

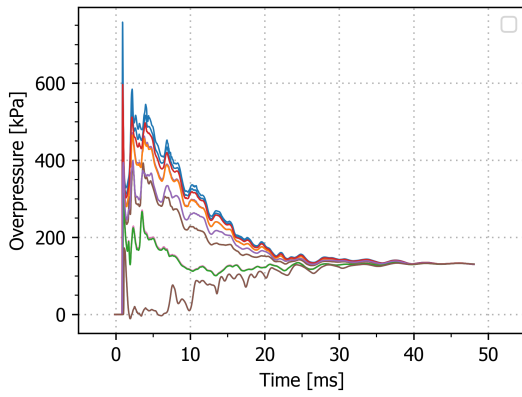
B.1 CFD Load



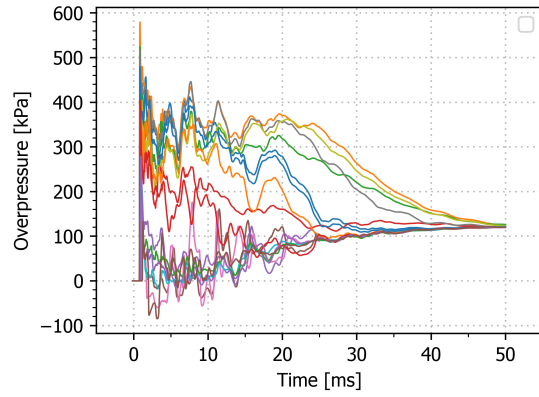
(a) n_CFD_O_20



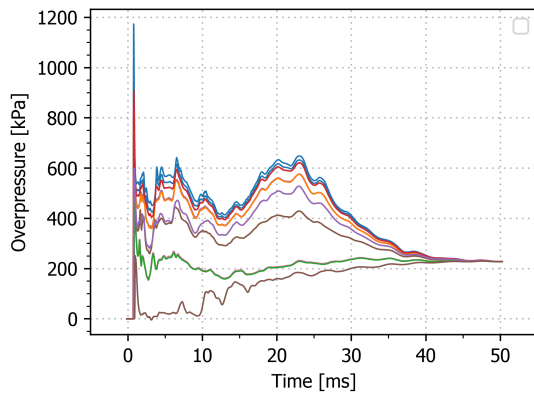
(b) n_CFD_W_20



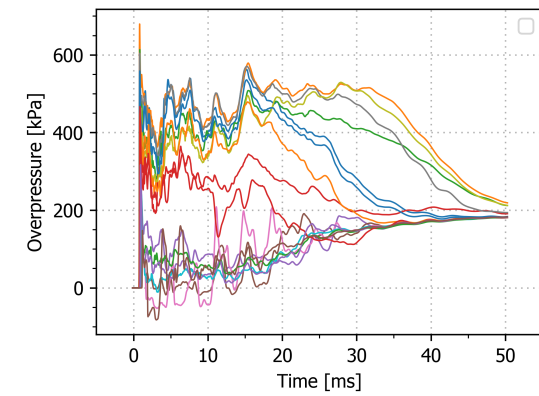
(c) n_CFD_O_30



(d) n_CFD_W_40



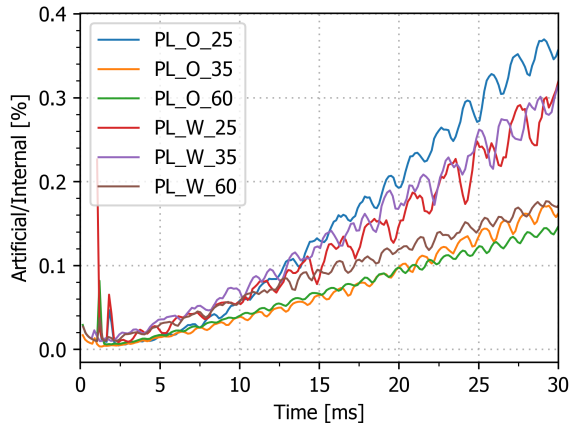
(e) n_CFD_O_60



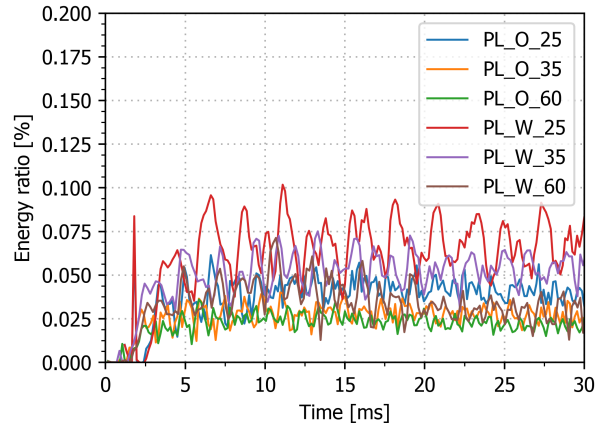
(f) n_CFD_W_60

Figure B.1: Overpressure-time histories from "sensor measurements" from the new CFD simulations.

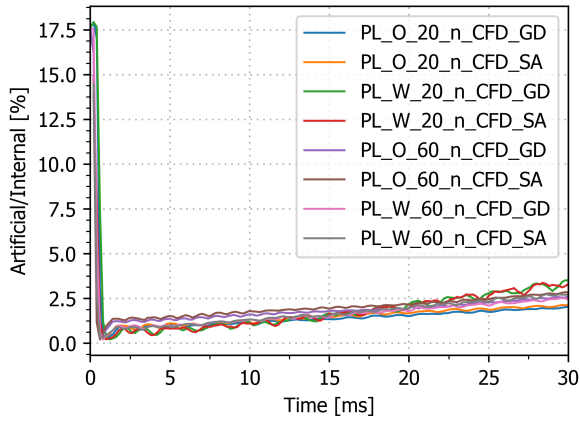
B.2 Plate



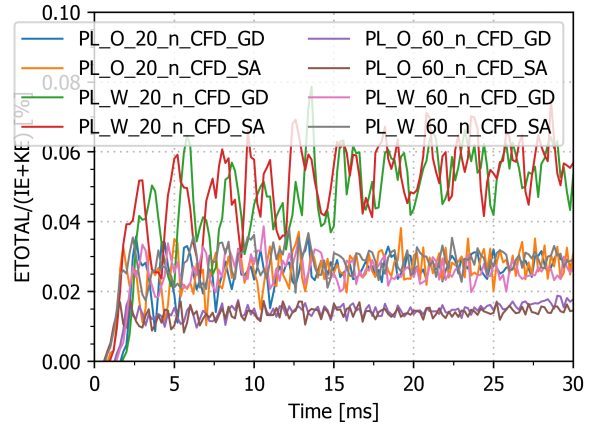
(a) Artificial energy



(b) Conservation of energy

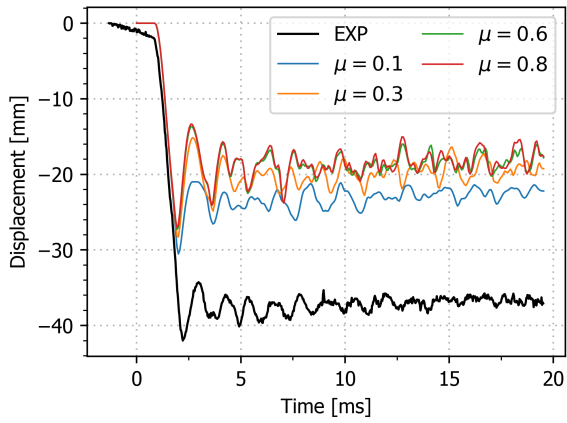


(c) Artificial energy

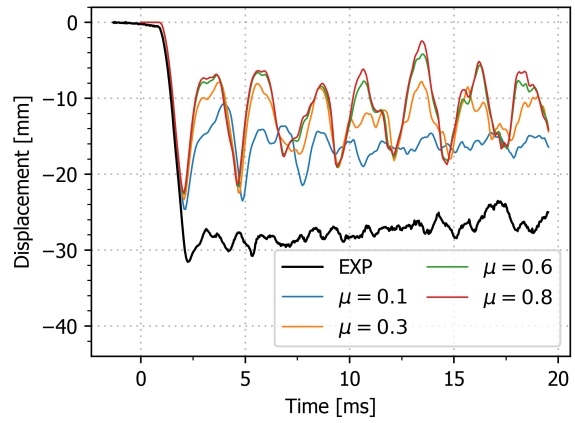


(d) Conservation of energy

Figure B.2: Energy plot where (a) and (b) are from Prelim 2 and (c) and (d) are from Numerical

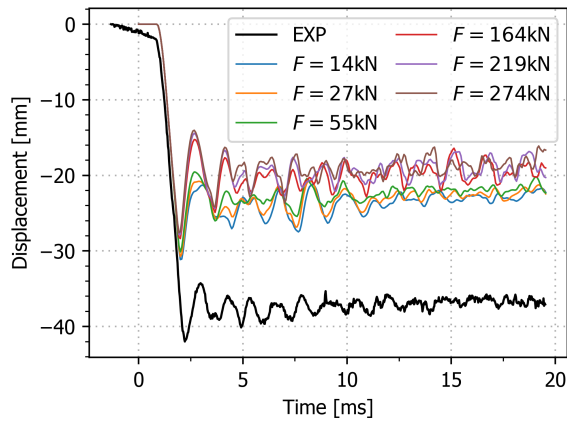


(a) PL_O_20 - n_CFD_GD



(b) PL_W_20 - n_CFD_GD

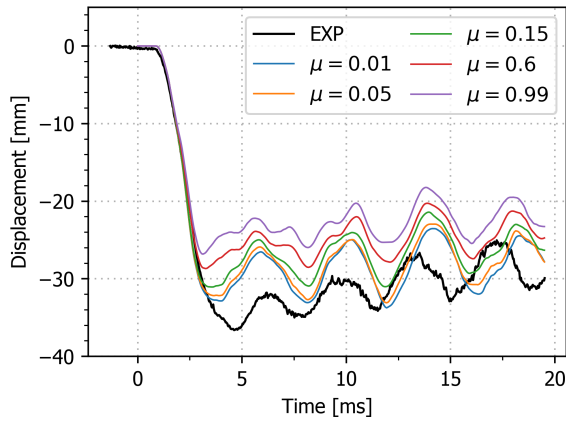
Figure B.3: Frictional coefficient study displayed as midpoint deflection-time curves.



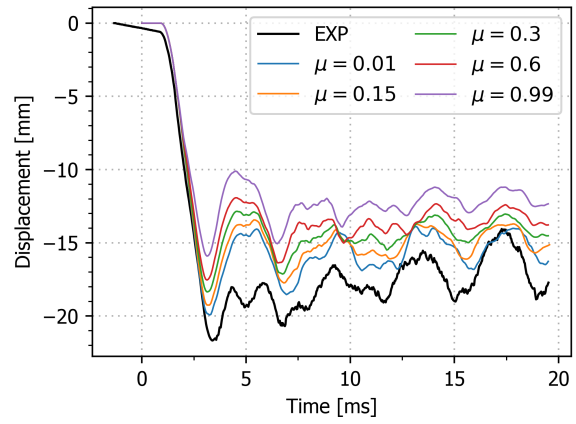
(a) PL_O_20 - n_CFD_GD

Figure B.4: Pretension force study displayed as midpoint deflection-time curves.

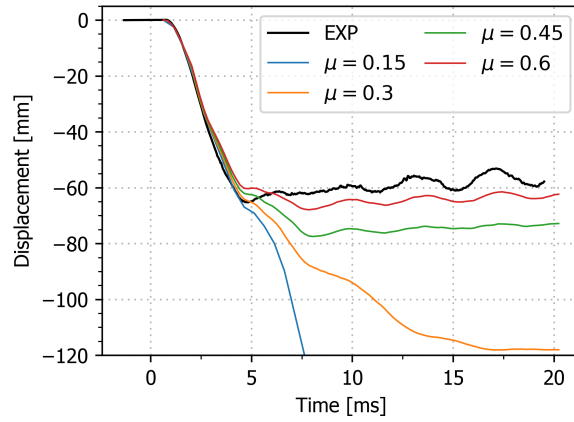
B.3 Stiffened Panel



(a) PA_O_20 - n.CFD_GD

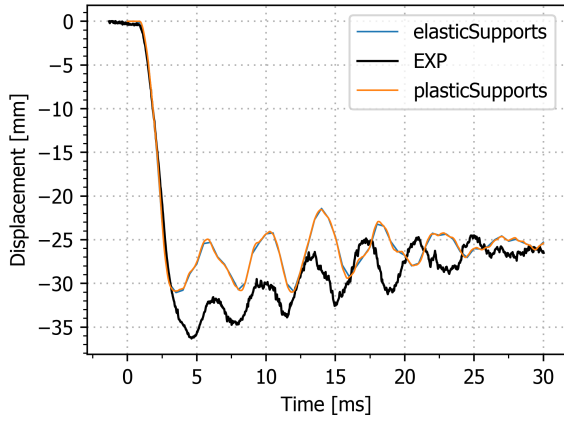


(b) PA_W_20 - n.CFD_GD

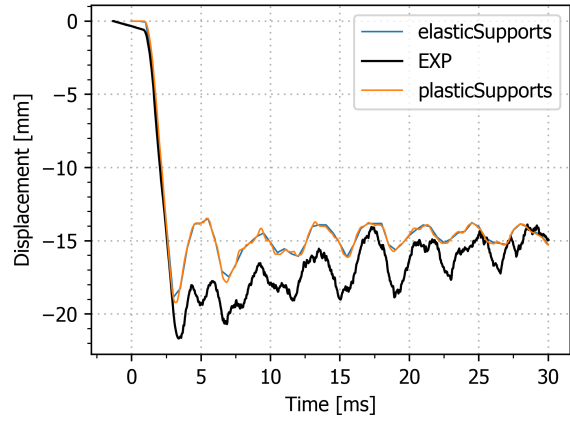


(c) PA_O_30 - n.CFD_SA

Figure B.5: Frictional coefficient study displayed as middle flange midpoint deflection-time curves.



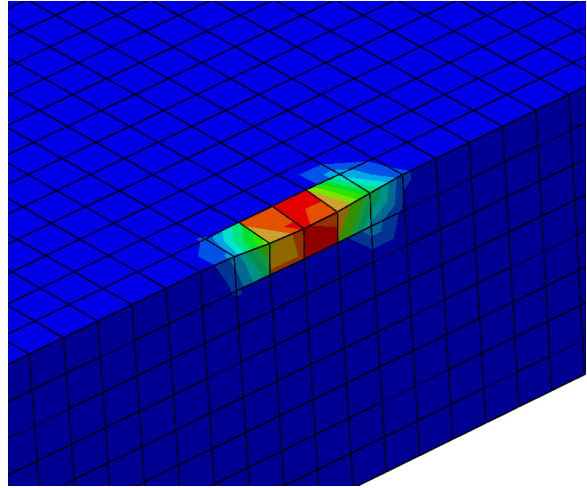
(a) PA_O_20 - n_CFD_GD



(b) PA_W_20 - n_CFD_GD



(c) Photo from laboratory



(d) PA_O_20 - n_CFD_GD

Figure B.6: Plastic material behaviour of the supports study. (a) - (b) middle flange midpoint deflection-time curves. (c) - (d) pictures of the plastic deformation.

